SCUOLA DI DOTTORATO
Università Mediterranea di Reggio Calabria

DIPARTIMENTO
DICEAM

DOTTORATO DI RICERCA
INGEGNERIA CIVILE, AMBIENTALE E INDUSTRIALE

S.S.D. ING-IND/31
XXXVIII CICLO

INFRARED THERMOGRAPHY AND ARTIFICIAL INTELLIGENCE FOR PREDICTIVE DIAGNOSTICS IN ELECTRICAL SYSTEMS

From Photovoltaic Monitoring to Advanced Energy Management in Hybrid Microgrids

Dottorando
Danilo Pratticò
[redacted]

Tutor
Prof. Fabio La Foresta
[redacted]

Coordinatore del Dottorato
Prof. Matilde Pietrafesa
[redacted]

Table of Contents

List of Figures

List of Tables

Abbreviations

AI	Artificial Intelligence
ANN	Artificial Neural Network
AG	Attention Gate
ASPP	Atrous Spatial Pyramid Pooling
BESS	Battery Energy Storage System
CNN	Convolutional Neural Network
CA	Current Absorption
DC	Direct Current
DC/DC	Direct Current to Direct Current
DC/AC	Direct Current to Alternating Current
DER	Distributed Energy Resource
DL	Deep Learning
DRL	Deep Reinforcement Learning
DSP	Digital Signal Processor
DNN	Deep Neural Network
EMS	Energy Management System
EN	European Norm
ENTSO-E	European Network of Transmission System Operators for Electricity
ETS	Emissions Trading System
FC	Fuel Cell
FPGA	Field Programmable Gate Array
FPN	Feature Pyramid Network
GRU	Gated Recurrent Unit
IEC	International Electrotechnical Commission
IEEE	Institute of Electrical and Electronics Engineers
IoT	Internet of Things
IR	Infrared
IRT	Infrared Thermography
LSTM	Long Short-Term Memory
L-UN	LSTM–U-Net hybrid architecture
LV	Low Voltage
MG	Microgrid
MILP	Mixed Integer Linear Programming
MPC	Model Predictive Control
MPPT	Maximum Power Point Tracking

O&M	Operation and Maintenance
OPF	Optimal Power Flow
PCC	Point of Common Coupling
PdM	Predictive Maintenance
PEMFC	Proton Exchange Membrane Fuel Cell
PF	Power Factor
PQ	Power Quality
PV	Photovoltaic
RES	Renewable Energy Source
RMS	Root Mean Square
RNN	Recurrent Neural Network
SE	Squeeze-and-Excitation
SVM	Support Vector Machine
SoH	State of Health
SOC	State of Charge
TDD	Total Demand Distortion
THD	Total Harmonic Distortion
THD_V	Total Harmonic Distortion of Voltage
UAV	Unmanned Aerial Vehicle
ViT	Vision Transformer
VSC	Voltage Source Converter
WT	Wind Turbine

Abstract

This thesis is framed within the context of the European energy transition, which aims to achieve climate neutrality by 2050 and recognises the strategic role of photovoltaic (PV) and smart grid technologies in decarbonisation process. The research adopts a multidisciplinary approach to the topics of predictive maintenance (PdM) and intelligent energy management systems (EMS) applied to PV plants and hybrid AC/DC microgrids (MGs), integrating expertise in infrared thermography (IRT), artificial intelligence (AI) and physical-numerical modelling. The growing complexity of distributed systems and the variability of operating conditions make corrective or preventive maintenance approaches based on manual inspections and static thresholds inadequate. In this context, the combination of IRT and AI represents a high potential technological frontier, as it allows for rapid, non-destructive and automatable diagnostics, paving the way for predictive maintenance integrated with efficient EMS.

The main goal is to build a standardised solution that can combine automatic fault diagnostics, state of health (SoH) assessment of components, and adaptive control of energy flows, helping to make next-gen power grids more reliable, efficient, and sustainable.

The first part of the thesis analyses the physical principles of IRT and the relevant regulations, highlighting the measurement conditions and radiometric parameters necessary to ensure repeatability and traceability of results. An experimental thermographic campaign was conducted on the PV plant of the DICEAM Department of the Mediterranean University of Reggio Calabria, with the acquisition of IRT images. The images, annotated and balanced, enabled the creation of an original multi-class dataset, comprising six categories of defects: hotspots, bypass diode failure, substring faults, shading/soiling, glass damage and background. Starting from this dataset, a semantic segmentation model called Efficient Attentive U-Net was designed, based on U-Net encoder-decoder architectures with MobileNetV2 encoder, ASPP (Atrous Spatial Pyramid Pooling) modules for multi-scale aggregation, Attention Gates (AG) for spatial selection, and Squeeze-and-Excitation (SE) for adaptive channel weighting. This configuration made it possible to balance accuracy and computational lightness, achieving high performance with a reduced number of parameters and real-time inference, making the model appropriate for implementation on drones and edge devices.

The proposed architecture allows for the accurate identification of segmented thermal maps which, in future developments, will enable the creation of predictive models capable of estimating the impact of faults on the electrical performance of the module.

The methodology has been extended to the industrial domain, in particular to electrical distribution switchboards, through the development of a hybrid LSTM–U-Net (L-UN) model. The integration of temporal analysis of electrical signals and spatial segmentation of IRT images has allowed for the early detection of abnormal overheating and current overloads, anticipating fault conditions. The system, implemented on Raspberry Pi and Arduino platforms, showed excellent accuracy in predicting current absorption and automatically classifying thermal status, reducing unnecessary maintenance interventions. This multimodal application demonstrated the effectiveness of the PdM–AI–IRT paradigm even in complex industrial contexts, validating the possibility of creating intelligent distributed systems for the PdM of electrical components.

The final part of the thesis broadens the field of investigation to the modelling of a hybrid AC/DC MG, including PV and wind turbine (WT) generators, a fuel cell system (PEMFC), battery storage (BESS) and heterogeneous AC/DC loads. The model, developed in MATLAB/Simulink©, was accompanied by a Mamdani-type fuzzy EMS, designed to coordinate production, storage, and consumption in real time. The EMS simultaneously integrates Power Quality (PQ) indicators (ΔV, Δf, THD_V, TDD), state of charge (SOC) and dynamic tariff signals, pursuing dual technical and economic optimisation. Simulations have shown that the fuzzy EMS improves voltage stability, reduces harmonic distortion, increases self-consumption, and lowers daily operating costs.

The main innovative contribution consists in the development of two complementary systems for intelligent PdM and EMS, each address specifics aspect of diagnostics and operational optimisation in hybrid MGs. The bidirectional information link between AI diagnostic modules and fuzzy controllers makes it possible, in the future, to adapt dispatch strategies according to the health status of generators and converters, evolving towards cognitive MGs capable of predicting, preventing, and optimising.

In summary, the thesis provides a coherent and replicable framework that combines automatic thermographic analysis, physical modelling of energy systems and intelligent control, outlining a methodological path towards the digitalisation of maintenance and the predictive management of distributed networks. The results obtained confirm the validity of the proposed approach and lay the foundations for future research activities aimed at real-time AI-EMS integration, the adoption of digital twins for adaptive maintenance, and the use of interpretable neural models in accordance with IEC/IEEE standards for PQ and safety.

Sommario

Questo lavoro di tesi si inserisce nel contesto della transizione energetica europea, che mira a raggiungere la neutralità climatica entro il 2050 e riconosce il ruolo strategico delle tecnologie fotovoltaiche (PV) e delle reti elettriche intelligenti nel processo di decarbonizzazione. La ricerca adotta un approccio multidisciplinare ai temi della manutenzione predittiva (PdM) e dei sistemi intelligenti di gestione dell'energia (EMS) applicati agli impianti PV e alle microgrid ibride AC/DC (MG), integrando competenze in termografia a infrarossi (IRT), intelligenza artificiale (AI) e modellazione fisico-numerica. La crescente complessità dei sistemi distribuiti e la variabilità delle condizioni operative rendono inadeguati gli approcci di manutenzione correttiva o preventiva basati su ispezioni manuali e soglie statiche. In questo contesto, la combinazione di IRT e AI rappresenta una frontiera tecnologica ad alto potenziale, in quanto consente una diagnostica rapida, non distruttiva e automatizzabile, aprendo la strada alla manutenzione predittiva integrata con un EMS efficiente.

L'obiettivo principale è quello di costruire una soluzione standardizzata in grado di combinare la diagnostica automatica dei guasti, la valutazione dello stato di salute (SoH) dei componenti e il controllo adattivo dei flussi di energia, contribuendo a rendere le reti elettriche di nuova generazione più affidabili, efficienti e sostenibili.

La prima parte della tesi analizza i principi fisici dell'IRT e le normative pertinenti, evidenziando le condizioni di misurazione e i parametri radiometrici necessari per garantire la ripetibilità e la tracciabilità dei risultati. È stata condotta una campagna termografica sperimentale sull'impianto PV del Dipartimento DICEAM dell'Università Mediterranea di Reggio Calabria, con l'acquisizione di immagini IRT. Le immagini, annotate e bilanciate, hanno consentito la creazione di un dataset multi-classe originale, comprendente sei categorie di difetti: hotspot, guasto dei diodi di bypass, guasti alle sottostringhe, ombreggiamento/sporcizia, danni al vetro e sfondo. Partendo da questo dataset, è stato progettato un modello di segmentazione semantica chiamato Efficient Attentive U-Net, basato su architetture U-Net encoder-decoder con encoder MobileNetV2, moduli ASPP (Atrous Spatial Pyramid Pooling) per l'aggregazione multiscala, Attention Gates (AG) per la selezione spaziale e Squeeze-and-Excitation (SE) per la ponderazione adattiva dei canali. Questa configurazione ha permesso di bilanciare accuratezza e leggerezza computazionale, ottenendo prestazioni elevate con un numero ridotto di parametri e inferenze in tempo reale, rendendo il modello adatto all'implementazione su droni e dispositivi edge. L'architettura proposta consente l'identificazione accurata delle mappe termiche segmentate che, in futuri sviluppi, consentiranno la creazione

di modelli predittivi in grado di stimare l'impatto dei guasti sulle prestazioni elettriche del modulo.

La metodologia è stata estesa al dominio industriale, in particolare ai quadri di distribuzione elettrica, attraverso lo sviluppo di un modello ibrido LSTM-U-Net (L-UN). L'integrazione dell'analisi temporale dei segnali elettrici e della segmentazione spaziale delle immagini IRT ha consentito il rilevamento precoce di surriscaldamenti anomali e sovraccarichi di corrente, anticipando le condizioni di guasto. Il sistema, implementato su piattaforme Raspberry Pi e Arduino, ha mostrato un'eccellente accuratezza nella previsione dell'assorbimento di corrente e nella classificazione automatica dello stato termico, riducendo gli interventi di manutenzione non necessari. Questa applicazione multimodale ha dimostrato l'efficacia del paradigma PdM-AI-IRT anche in contesti industriali complessi, convalidando la possibilità di creare sistemi distribuiti intelligenti per il PdM dei componenti elettrici.

La parte finale della tesi amplia il campo di indagine alla modellizzazione di un MG ibrido AC/DC, che include generatori fotovoltaici e eolici (WT), un sistema a celle a combustibile (PEMFC), un sistema di accumulo a batteria (BESS) e carichi eterogenei AC/DC. Il modello, sviluppato in MATLAB/Simulink©, è stato accompagnato da un EMS fuzzy di tipo Mamdani, progettato per coordinare la produzione, lo stoccaggio e il consumo in tempo reale. L'EMS integra simultaneamente indicatori di qualità dell'energia (PQ) (ΔV, Δf, THDV, TDD), stato di carica (SOC) e segnali tariffari dinamici, perseguendo una doppia ottimizzazione tecnica ed economica. Le simulazioni hanno dimostrato che l'EMS fuzzy migliora la stabilità della tensione, riduce la distorsione armonica, aumenta l'autoconsumo e abbassa i costi operativi giornalieri.

Il principale contributo innovativo consiste nello sviluppo di due sistemi complementari per il PdM e l'EMS intelligenti, ciascuno dei quali affronta aspetti specifici della diagnostica e dell'ottimizzazione operativa nei MG ibridi. Il collegamento bidirezionale di informazioni tra i moduli diagnostici AI e i controllori fuzzy rende possibile, in futuro, adattare le strategie di dispacciamento in base allo stato di salute dei generatori e dei convertitori, evolvendo verso MG cognitivi in grado di prevedere, prevenire e ottimizzare.

In sintesi, la tesi fornisce un quadro coerente e replicabile che combina l'analisi termografica automatica, la modellizzazione fisica dei sistemi energetici e il controllo intelligente, delineando un percorso metodologico verso la digitalizzazione della manutenzione e la gestione predittiva delle reti distribuite. I risultati ottenuti confermano la validità dell'approccio proposto e gettano le basi per future attività di ricerca volte all'integrazione in tempo reale di AI-EMS, all'adozione di gemelli digitali per la manutenzione adattiva e all'uso di modelli neurali interpretabili in conformità con gli standard IEC/IEEE per la PQ e la sicurezza.

Thesis Outline

This doctoral thesis is organised into six chapters, each contributing to the overall goal of developing an integrated framework for electrical PdM based on IRT and AI, and its holistic integration into hybrid AC/DC MGs with fuzzy-logic EMS.

Chapter 1 introduces the motivation and objectives of the research within the context of the European energy transition and the rapid growth of PV systems.

It outlines the limitations of traditional Operation & Maintenance (O&M) strategies and discusses how artificial intelligence and thermographic diagnostics can transform maintenance from reactive to predictive.

The chapter also presents the theoretical background and state of the art, defining the research questions, original contributions, and overall structure of the work.

The identified research gaps provide the rationale for the proposed methodology.

Chapter 2 describes the thermographic campaign conducted at the DICEAM PV plant of the University of Reggio Calabria. It details the instrumentation, measurement protocols compliant with IEC TS 62446-3:2017, and the acquisition of thermal images under standardised conditions.

The chapter explains how the collected data were pre-processed, annotated, and statistically balanced to construct a high-quality multi-class dataset suitable for deep learning training.

Chapter 3 introduces the proposed Efficient Attentive U-Net architecture, developed for multi-class defect segmentation in thermographic PV images. The model combines MobileNetV2 encoding with AGs, SE blocks, and Atrous Spatial Pyramid Pooling (ASPP) to improve multi-scale contextual awareness. Extensive validation, ablation studies, and comparative analysis with state-of-the-art models confirm its superior accuracy, efficiency, and interpretability.

The chapter concludes with an energy correlation analysis linking the segmented defect areas to measurable power losses.

Chapter 4 extends the AI–IRT framework to the predictive diagnostics of industrial electrical switchboards, a critical component of energy distribution networks and MG infrastructures.

A hybrid U-Net + LSTM model is developed to jointly process thermal images and electrical signals, enabling both spatial defect detection and temporal anomaly prediction. The chapter describes the multimodal acquisition system designed for synchronous data collection, the dataset structure, and the predictive results demonstrating early detection of overheating and load imbalance conditions.

Chapter 5 integrates predictive maintenance into a system-level control context through the modelling and optimisation of a hybrid AC/DC MG. Using MATLAB/Simulink©, a fuzzy-logic EMS is

implemented to coordinate renewable sources, battery storage, and grid interaction.

The results show significant improvements in PQ, cost reduction, and self-consumption, and establish a conceptual link between diagnostic intelligence and adaptive energy management.

Finally, Chapter 6 summarises the findings, highlighting the originality and scientific contributions of the work. It discusses the implications of combining IRT and AI for predictive electrical maintenance, identifies the main limitations of the current approach, and proposes future developments toward AI-driven predictive MGs, including the integration of intelligent EMS frameworks, edge computing, and UAV-based thermographic monitoring.

1. Introduction and research context

This chapter outlines the European policies for energy transition and climate neutrality by 2050, and the growing role of photovoltaic (PV) energy in decarbonisation and in the development of smart grids. The goal is to delineate the technical-scientific context of the research, by illustrating the principles, technologies, and methodologies that enable predictive maintenance (PdM) and advanced management of distributed energy systems.

This section analyses the theoretical foundations, physical models, and artificial intelligence (AI) techniques underlying the predictive diagnostics of PV systems and hybrid AC/DC microgrids (MGs). After providing an overview of the architectures and operating modes of PV systems, the chapter explores the degradation mechanisms of modules and the radiometric and thermophysical principles that govern infrared thermography (IRT) as a non-destructive analysis tool.

Subsequently, an analysis of the main deep learning (DL) approaches used for the processing and classification of thermal images is conducted, with particular attention to convolutional neural networks (CNN), encoder–decoder architectures derived from U-Net, and attention-based and Long Short-Term Memory (LSTM) models, which are now widely used for fault diagnosis and health monitoring of electrical components such as electrical switchboards.

Furthermore, the concept of Energy Management System (EMS) is introduced as a higher level of control for the coordinated management of renewable generation, storage systems, and loads in hybrid AC/DC MGs. The main EMS methods adopted in hybrid AC/DC MGs are described, highlighting the limitations of each and their central role in the predictive optimisation of energy flows.

In conclusion, the main scientific contributions of the research and the overall structure of the thesis are outlined.

1.1. The Photovoltaic Sector in the European Energy Transition

1.1.1. Energy neutrality by 2050 and European policies for the green transition

The European Union (EU) has established, with the European Climate Law (Reg. EU 2021/1119), the legal objective of climate neutrality by 2050, with a net reduction in greenhouse gas emissions of at least 55% by 2030 compared to 1990 levels [1]. This goal is the core of the European Green Deal, the strategic plan launched in 2019 to transform the EU

economy into a competitive and sustainable model, capable of combining growth, energy security and environmental protection [2].

To achieve these objectives, EU has adopted the Fit for 55 legislative packages, which updates the main regulatory instruments on the emissions trading system (ETS) market, renewable energy sources (RES), energy efficiency and sustainable mobility [3]. At the same time, following the 2021-2022 energy crisis, the REPowerEU plan (COM (2022) 108 final) set out extraordinary measures to reduce dependence on imported fossil fuels, in particular by boosting solar and wind power generation and simplifying authorisation procedures [4].

The Net Zero Industry Act (Reg. EU 2024/1735) represents the industrial pillar of the new paradigm: it aims to consolidate the European zero-emission technology supply chain, including the production of PV modules, inverters and storage systems[5]. In parallel, the European Solar Charter (2024) formalises cooperation between the Commission, Member States and businesses to strengthen the competitiveness and security of the solar value chain [6].

Thanks to this strategic frameworks, EU aims to bring installed PV capacity to over 600 GW by 2030, promoting the spread of distributed solar energy in buildings, energy communities and local MGs [7]. However, this expansion requires a profound rethinking of maintenance, monitoring and grid integration strategies, as the large number of installations calls for automated and data-driven solutions to secure reliability and performance throughout the entire life cycle.

The progressive penetration of PV systems is associated with a decentralisation of generation and a growing role for prosumers, favouring the evolution of traditional networks towards interconnected and flexible smart grids [8]. These systems, supported by sensors, IoT devices and AI methods, enable real-time monitoring of production and loads, as well as optimised management of distributed resources.

In this context, PV is no longer a simple passive generator, but an active node in the grid, capable of participating in balancing and grid services through controllable inverters and storage systems. However, the reliability of the modules remains a critical factor: failures, degradation and thermal anomalies can compromise productivity and introduce imbalances in the quality of the power supplied. The digital transition of the energy sector therefore requires the synergistic integration of advanced diagnostics, PdM and intelligent management techniques to support the growth of European solar energy and ensure the stability of future AC/DC hybrid MGs [9].

1.2. Technologies of PV systems

A PV system consists of one or more strings of modules connected in series and parallel, power converters and control systems. Each PV module is composed of silicon cells (mono or polycrystalline) connected electrically and encapsulated in a glass-EVA-backsheet laminate.

PV is now one of the key technologies for the energy transition, thanks to steadily falling costs, high modularity, and the possibility of widespread integration into electricity grids. Over the last twenty years, the average cost of modules has fallen by more than 90%, from over €4/W in 2005 to less than €0.3/W in 2024 [10]. This evolution has been pushed by innovations in manufacturing processes, cell efficiency, and the global production chain.

The most widely used technologies can be divided into three main families:

i. Crystalline silicon (c-Si) – accounts for over 90% of the market, with PERC and TOPCon monocrystalline cells exceeding efficiencies of 23–24%.
ii. Thin film (a-Si, CdTe, CIGS) – characterised by reduced thickness and lower costs, but lower efficiencies (10–18%).
iii. New generation cells – include perovskites, perovskite-silicon tandems and organic cells, with record efficiencies exceeding 26% in the laboratory [11].

The increase in performance has been accompanied by advances in encapsulation materials, anti-reflective coatings and backsheets, which improve resistance to thermo-mechanical stress and irradiation cycles. At the same time, the development of bifacial and half-cut modules allows for better management of partial currents and more stable performance in real-world conditions [12].

1.2.1. System architectures and conversion topologies

The architectural configuration of a PV system is determinant for its overall performance, operational reliability, and ease of integration with the electricity grid. The evolution of energy conversion topologies — from the module level to low or medium voltage connections — has been driven by the need to maximise power extraction efficiency, ensure electrical safety and enable intelligent control functions.

A PV system consists of a conversion chain that includes:

- solar field (array of modules connected in series/parallel);
- string panels and protection devices;
- DC/DC converters and DC/AC inverters;
- transformers, distribution lines and loads or public grid.

Depending on the scale of installation and the control logic employed, the same components can be organised according to different architectural topologies, each characterised by specific advantages and limitations in terms of efficiency, modularity, and reliability. The most common architectures are:

- centralised, in which many strings converge on a single high-power inverter (typical of utility-scale parks);
- multi-string, with separate inverters for groups of strings;
- modular or distributed, with microinverters or power optimisers dedicated to each module [13].

Distributed configurations, now widely adopted in residential and commercial installations, improve fault resilience, and allow for accurate monitoring of the performance of each module.

Modern inverters also integrate Maximum Power Point Tracking (MPPT), grid support functions (var-control, frequency ride-through) and interfaces for digital communication (Modbus, CAN, IEC 61850), making the system an active part of the smart grid [14].

The evolution of PV architectures is converging towards intelligent, sensor equipped and interconnected systems capable of integrating diagnostics, control, and automated maintenance.

The inclusion of real-time temperature, radiation, voltage and current sensors, combined with the use of cloud platforms and artificial intelligence algorithms, enables the implementation of predictive monitoring, fault detection and energy efficiency optimisation functions [15].

This paradigm forms the basis for subsequent integration with hybrid AC/DC MGs and EMS, which are the subject of the following chapters.

1.2.2. Connection standards and requirements

At European and national level (Italy), the connection and operation of PV systems are governed by specific regulations. The main regulations are:

- IEC 61724-1:2021, which defines the criteria for performance monitoring;
- IEC 62109-1/-2, on the electrical and thermal safety requirements of inverters;
- CEI 0-21 (low voltage) and CEI 0-16 (medium voltage), which regulate the technical conditions for connection and power quality limits in Italy;
- EN 50530, which establishes methods for measuring the static and dynamic efficiency of inverters [13, 16].

The respect of these standards is essential not only for regulatory compliance, but also to guarantee interoperability with EMS, operator safety and the stability of the overall electrical system.

1.3. Operation & Maintenance (O&M) challenges in PV systems

1.3.1. Degradation and failures in PV modules: energy and economic impacts

During operation, PV plants are subject to degradation phenomena that compromise the efficiency and safety of the system. The reliability of PV modules is a key factor in the technical and economic sustainability of systems. Although the nominal useful life of a module is between 25 and 30 years, numerous studies have shown that the average rate of

power degradation varies between 0.5% and 0.8% per year, with peaks exceeding 1% in climates with high insolation or in the presence of thermal and mechanical stress [11, 17].

The main causes of deterioration include delamination, micro-cracking, contact corrosion, hot spots, bypass diode failures and ageing of the encapsulant (EVA) [18]. These phenomena cause localised heat dispersion, current unevenness in the strings and power losses which, on a large scale, can lead to reductions in energy yield of more than 10% compared to nominal conditions [19].

From an economic perspective, the costs associated with faults that are not detected in a timely manner include lost production, costly corrective measures, and a reduction in the remaining life of the modules. SolarPower Europe estimates that non-optimised O&M strategies can reduce the internal rate of return (IRR) of a utility-scale plant by up to 2-3 percentage points compared to a system equipped with predictive diagnostics and scheduled maintenance [20]. These losses are more relevant in the context of large distributed systems and energy communities, where the aggregation of widespread micro-faults affects the overall stability of the grid and the remuneration of the energy fed into the system.

1.3.2. Electrical and thermal PV faults

Electrical faults are one of the most frequent causes of reduced performance in PV systems. They result from current or voltage imbalances between cells, interruptions in the connection circuits or abnormal behaviour of the protection components, and typically manifest themselves as localised overheating.

The main electrical faults include:

- Hotspots: generated by partially shaded or damaged cells that behave as dissipative loads, converting the energy produced by healthy cells into heat. They can reach temperatures above 100 °C and cause irreversible damage to the EVA and front glass [21].
- Bypass diode failures: a shorted diode reduces the output voltage of the string, while an open diode prevents the bypass of the defective cell, amplifying the formation of hotspots [22].
- Breakage or corrosion of busbars and interconnections: these cause localised voltage drops and electrical instability; they are often linked to thermal cycles and high humidity.
- Current mismatch: due to power losses between cells or modules, accentuated by uneven ageing, dirt, or partial shading [23].
- Potential Induced Degradation (PID): caused by leakage currents to the metal frame under high polarisation voltages; produces power loss and blackening visible in thermography [24].

These phenomena result in significant reductions in conversion efficiency and, in severe cases, risks of thermal runaway or fire. Their timely detection is therefore essential to preserve the safety and useful life of the system.

In besides electrical defects, PV modules are subject to a wide range of physical-chemical degradation processes induced by environmental, mechanical, and thermal factors.

Although these phenomena evolve slowly over time, they contribute significantly to the annual performance loss rate (PLR), which is generally between 0.5% and 0.8% per year for crystalline silicon modules [11].

The main degradation mechanisms include:

- LID (Light Induced Degradation): loss of initial efficiency in the first hours of exposure due to carrier recombination induced by defects in silicon dopants.
- LeTID (Light and elevated Temperature Induced Degradation): worsening of LID at operating temperatures above 60 °C, with a power reduction of up to 5% [25].
- Micro-cracking and cell fractures: caused by mechanical stress (wind, transport, hail) or thermal stress (differential expansion); these cause abnormal resistive paths and widespread hotspots.
- Delamination of EVA or backsheet: loss of adhesion between the layers of the module facilitates the entry of moisture and oxygen, accelerating the oxidation of metal contacts.
- Optical ageing and yellowing of EVA: reduce visible light transmission and leads to a gradual loss of short-circuit current.
- Soiling and biological deposits: the deposition of dust, pollen, sand or organic residues decreases effective irradiation and alters surface thermal distribution, generating false hotspots in thermography [26].
- Corrosion from moisture and aggressive gases: more pronounced in coastal or industrial environments, it degrades metal connections and reduces insulation resistance [27].

Many of these defects interact synergistically: for example, a micro-crack facilitates moisture penetration and accelerates delamination, while PID amplifies the local thermal effect of hotspots.

The combined analysis of IR images, electrical signals and environmental data is therefore essential for a complete diagnosis and for estimating the SoH of the modules over time.

1.3.3. Limitations of corrective and preventive approaches

Traditionally, PV system maintenance has been based on corrective or preventive strategies. Corrective maintenance only intervenes after

failure or performance degradation, inevitably leading to high downtime, unexpected costs, and planning difficulties.

PdM, on the other hand, involves scheduled periodic checks (e.g. visual inspections, electrical tests, manual thermography), but is often unable to detect latent defects or slow degradation that only manifest themselves under particular environmental or operating conditions [28].

Both strategies suffer from a lack of granular information on the actual phenomena developing in the modules and components of the BOS (Balance of System). In particular, aggregate electrical measurements at string or inverter level do not allow localised defects to be identified, while traditional periodic inspections do not guarantee continuous monitoring [29].

This results in the need for non-destructive, automated, and high spatial resolution methods capable of providing thermal and radiometric information directly in the field, even in large-scale plants.

1.3.4. Evolution towards data-driven predictive maintenance

In recent years, technological advances in sensors and digital infrastructure have facilitated the transition to PdM based on continuous analysis of environmental, electrical, and thermographic data. This paradigm focuses on detecting defects and predicting when a fault will occur, enabling rapid evaluation of the impact on performance and targeted intervention [30].

The PdM approach is based on a combination of non-destructive diagnostics (e.g., IRT, electroluminescence, IV-curve tracing) and artificial intelligence, which allows the behaviour of the modules to be modelled and abnormal patterns that are difficult to interpret using traditional methods to be recognised.

In particular, the integration of IRT and DL allows for the automation of PV field inspections, quickly identifying anomalies such as hotspots, shading, soiling and bypass diode defects [31].

This transition to PdM, powered by data analysis, edge computing and AI algorithms, is a fundamental element for the reliability, efficiency, and sustainability of the new generation of European solar plants and their integration into distributed energy systems and hybrid MG.

1.4. Non-destructive diagnostics using IRT and AI

1.4.1. Physical principles, radiometric parameters, and compliance criteria

IRT is a non-destructive diagnostic technique that allows contactless measurement of temperature distribution on the surface of PV modules. It is based on the principle that any body with a temperature above

absolute zero emits electromagnetic radiation proportional to its absolute temperature according to Stefan-Boltzmann's law (1):

$$E = \varepsilon \sigma T^4 \quad (1)$$

Where E is the surface emissivity (W m^{-2}), ε is the emissivity coefficient (0–1), σ is the Stefan-Boltzmann constant (5.67×10^{-8} W m^{-2} K^{-4}) and T is the absolute temperature (K) [32].

In PV modules, the radiation measured by the IR sensor comprises three main components: the module's own emission, the reflected radiation from the surrounding environment, and the radiation transmitted through the overlapping materials (glass, EVA, backsheet).

The thermal imaging camera converts the radiometric signal into an apparent temperature value, which must be corrected for the emissivity of the material and the apparent reflected temperature.

For glass-EVA-Si-backsheet modules, the commonly adopted emissivity value is between 0.90 and 0.95, while atmospheric reflectance strongly depends on the angle of incidence and irradiation conditions [33]. The main advantages of IRT over other diagnostic methods include:

- speed and spatial coverage (up to hundreds of modules in a few minutes);
- no service interruption, as measurements can be performed while the plant is in operation;
- direct visual detection of defects, facilitating qualitative assessment and fault mapping;
- integration with automatic systems (unmanned aerial vehicles (UAVs), ground robots, edge platforms).

IRT analysis of PV modules allows local anomalies (hotspots, interconnection defects, short-circuited or open bypass diodes, micro-cracked cells, shading, soiling) to be identified through thermal differences of less than 2–3 °C compared to adjacent areas [34].

This sensitivity, combined with the possibility of remote acquisition by drone or ground vehicle, makes IRT an ideal technique for rapid, high-spatial-resolution inspections of large solar fields.

1.4.2. Reference Standards and Compliance Criteria

The main technical reference for performing thermographic measurements on PV systems is IEC TS 62446-3:2017. It establishes the operating conditions and measurement procedures for the application of outdoor IRT, distinguishing between two types of inspection configurations: open circuit inspection, in which the generator does not supply current and inspection under nominal operating conditions, performed with the system in production.

The standard IEC TS 62446-3:2017 also defines:

- the minimum environmental conditions to ensure the significance of the measurement; measurement configurations (on the ground, on a drone, on an operating plant or in an open circuit);

- the radiometric parameters to be recorded (emissivity, distance, angle, reflected temperature, humidity, wind, irradiance);
- the criteria for accepting the results, based on the maximum permissible temperature difference between cells or substrings.

With the support of the IEA-PVPS Task 13 document, the categories and indicative thermal thresholds for the formal classification of PV defects are defined. Defects are divided into three macro-classes, as described in Table 1 [33].

Table 1.Defects macro-classes on PV systems

Category	*Typical examples*	*Thermal description and probable causes*
Electrical defects	Hotspots, faulty bypass diodes, open connections	Areas with temperature > 10 °C above the background; reverse current or local overload
Mechanical / environmental defects	Soiling, shading, cracks, delamination	Irregular but temporally stable thermal patterns; altered irradiation or heat conduction
Structural / aging defects	Busbar corrosion, backsheet delamination, PID	Diffuse temperature increase; current leakage or high resistance

The guidelines indicate that a temperature difference (ΔT) greater than 10 °C compared to the module average represents a serious anomaly requiring immediate intervention, while differences of less than 5 °C may be associated with dirt or temporary defects [35]. Temporal analysis of the images (ΔT trend) also allows transient phenomena to be distinguished from permanent faults.

1.4.3. Operating Measurement Conditions

To obtain reliable thermal images, IEC TS 62446-3 and the IEA-PVPS Task 13 guidelines stipulate that the inspection must be carried out under steady-state conditions and with sufficient irradiation, preferably during the middle of the day. The recommended parameters are summarised in Table 2.

Table 2. Recommended parameters values for IR inspections, based on normative reference.

Parameter	*Recommended Value*	*Normative Reference*
Global irradiance on the module plane	≥ 700 w/m² (optimal > 800 w/m²)	IEC TS 62446-3:2017 § 5.2
Ambient temperature	15 – 35 °c	IEC TS 62446-3 / IEA-PVPS T13-09
Wind speed	≤ 10 m/s (optimal < 5 m/s)	IEC TS 62446-3 § 5.3
Cloud coverage	Clear sky / ≤ 2 oktas	IEA-PVPS T13-09
Minimum detectable thermal difference	≥ 2 °c between cell and reference	IEC TS 62446-3 ANNEX A

Recommended viewing angle	< 45° with respect to the normal	IEC TS 62446-3 § 6.2

Compliance with these conditions ensures a good radiometric signal-to-noise ratio, minimising the effects of reflection, wind and variable radiation.

In addition, the standard requires that each thermal acquisition be accompanied by irradiance, ambient temperature and wind data from certified sensors or a local weather station to enable traceability and repeatability of measurements.

In the context of this research, IRT is therefore considered a key diagnostic methodology for the predictive maintenance of PV modules, as it provides physically interpretable information that can be standardised and integrated into automatic processing pipelines based on AI applications.

1.4.4. AI for predictive diagnostics of PV systems

The advancement in AI and DL has revolutionised the way data from PV systems is analysed, enabling the automation of monitoring and diagnostic procedures. Increased computing power, the availability of IR image datasets and the spread of edge devices have made it possible to overcome the limitations of traditional monitoring methods based on electrical thresholds or simplified physical models.

AI is now used in all phases of the PV plant life cycle: from power forecasting to module SoH estimation, to automatic defect identification and predictive maintenance [36].

Unlike methods based on regression or manual classifiers, neural models learn non-linear relationships between environmental variables, electrical signals, and images directly from the data, making them extremely adaptable to different operating conditions. In particular, a CNN consists of a sequence of convolutional, pooling and fully connected layers that enable the automatic extraction of hierarchical features (edges, patterns, textures). CNNs have proven to be particularly effective in processing thermal images acquired by IR cameras or drones, thanks to their ability to extract spatial feature hierarchies and discriminate anomalous patterns with high precision [36, 37].

One of the first studies in this field introduced a combination of Mask R-CNN, U-Net and Feature Pyramid Network (FPN) for the automatic identification of defective cells in thermal images acquired by UAVs, laying the foundations for automated module inspection and defining one of the first benchmarks in the PV domain [39]. Subsequently, another contribution compared machine learning approaches (SVM, Random Forest, KNN) with lightweight CNNs for IR image classification, demonstrating the clear superiority of convolutional architectures in terms of accuracy and robustness against thermal noise [40]. This work marked the transition from models based on manual features to end-to-end models, capable of automatically learning discriminative

representations from thermal data. A subsequent contribution presented a two-stage pipeline consisting of a U-Net network for module segmentation and a fully connected classifier for defect diagnosis [41]. This approach introduced for the first time a hierarchical thermal analysis procedure, in which accurate segmentation of the region of interest improved the subsequent defect classification. Another study proposed a comparative analysis between U-Net, FPN and DeepLabV3+, evaluating the performance of different architectures on images acquired in real environmental conditions. The analysis showed that U-Net maintains the best compromise between accuracy and computational complexity, making it particularly suitable for large-scale applications [42].

In parallel, a lightweight CNN model was developed for the early detection of hotspots on large PV fields [43].

The main objective was to ensure near real-time inference while keeping computational resources low, an essential requirement for implementation on drones and embedded devices.

A further contribution introduced a hybrid CNN–Machine Learning model, in which automatically extracted features were classified using traditional algorithms such as SVM or RF, achieving greater robustness to variations in irradiation and climatic conditions [44].

A U-Net-based model operating in the HSV domain introduced innovative pre-processing to reduce false positives related to reflections and thermal gradients, improving the separability between healthy and defective regions [45].

Another study presented an enhanced Mask R-CNN with an edge-guided spatial attention module, capable of emphasising thermal discontinuities and locating small anomalies more accurately [46]. This approach represented one of the first successful attempts to apply spatial attention mechanisms to PV thermography.

A further contribution developed a deep CNN for the automated thermal inspection of PV modules, with data balancing and augmentation strategies to manage unbalanced datasets and improve model generalisation [47]. The work highlighted the direct correlation between dataset size and performance stability, emphasising the importance of IR image diversity.

A subsequent approach proposed an optimised version of YOLO (called ST-YOLO) for automatic defect detection on PV thermal images [48]. The network was reduced in complexity through pruning and quantisation, while improving accuracy through a training phase specific to PV thermal patterns.

Another study introduced an improved VarifocalNet, with an adaptive loss function that penalises false negatives in rare defects such as cracks or soiling, thus improving the model's generalisation ability [49].

The integration of CNNs with IoT devices has enabled the creation of a distributed real-time diagnostic platform capable of continuously

acquiring and processing thermal and environmental data, highlighting the potential of embedded AI systems for predictive monitoring [50].

A particularly interesting contribution used a U-Net for the analysis of thermal video sequences, allowing the estimation of the temporal variation of the temperature of the modules and the monitoring of the evolution of degradation over time [51].

A comprehensive review study provided a systematic overview of the state of the art, identifying the main limitations: restricted datasets, lack of standardised models and little attention to computational scalability [52].

An important step forward is represented by a U-Net with customised ASPP, which introduced a multi-scale aggregation module optimised to capture thermal patterns of different sizes and intensities, improving the identification of thin or extended hotspots [53].

Another study proposed a CNN with dual attention (spatial and channel), capable of dynamically modulating feature importance and reducing defect region fragmentation [54].

This approach consolidated the effectiveness of combined attention in the thermographic context, highlighting how the fusion of spatial and channel attention improves model sensitivity.

A subsequent contribution introduced a lightweight Transformer model, which combines local convolutions and global self-attention mechanisms to capture long-range spatial relationships [55].

This hybrid CNN–ViT architecture represents a natural evolution towards more interpretable and generalisable models.

Finally, an in-depth literature review on image processing techniques, demonstrating the feasibility of a continuous and autonomous diagnostic flow for large PV plants [56].

A complete review of the literature reveals a consistent evolution:

- From classification to segmentation. Early studies focused on binary classification, while encoder–decoder architectures introduced pixel-wise segmentation, improving spatial accuracy [40, 41].
- Towards multi-scale and attention. The introduction of ASPP modules and spatial or channel attention mechanisms has increased effectiveness in detecting minute or distributed defects [45, 52, 53].
- Efficiency and real-time. The latest models favour lightweight architectures and pruning techniques to reduce complexity and enable use on UAV or embedded platforms [47, 54].
- Integration with IoT and predictive maintenance. Several studies have integrated CNN with field sensors or electrical data, bringing thermographic diagnostics closer to a comprehensive predictive maintenance framework [39, 55].

Despite the significant progress achieved by the studies analysed, several limitations persist in the application of DL to the thermographic diagnostics of PV modules.

A first critical issue concerns the poor generalisation of models: many studies are based on proprietary or small datasets, often acquired under specific climatic and angular conditions, which reduces the ability of models to adapt to real scenarios or different installations [38, 41, 44].

Secondly, most of the proposed architectures favour segmentation accuracy at the expense of computational efficiency, making implementation on edge devices or UAV platforms for field inspections difficult [42, 45, 47].

A further limitation is the lack of functional integration with the electrical parameters of the system: in most cases, thermal maps are analysed as isolated entities, without a direct link to performance indicators, IV curves or power loss [48, 49, 52].

Finally, only a few studies address the robustness of the model to thermal disturbances (wind, reflection, uneven radiation), which often generate false positives or fragmentation in the segmentation of defective areas [43, 50, 53].

To overcome these limitations, the research in this thesis focused on semantic segmentation architectures such as U-Net and its variants (U-Net++, Attention U-Net, DeepLabv3+) [57]. Encoder–decoder architectures have been developed, which combine a compression phase (encoder) with an expansion phase (decoder), returning segmentation maps that describe the position and extent of defects. Encoder–decoder architectures capable of producing pixel-wise maps that highlight the morphology and extent of defects. These models are particularly suitable for IRT, as they allow different types of anomalies to be distinguished and their area and thermal intensity to be quantified.

The work presented in this thesis introduce an architecture called Efficient Attentive U-Net, designed to combine accuracy, generalisation, and computational lightness. The model integrates ASPP, Attention Gates (AGs) and Squeeze-and-Excitation (SE) blocks, combining the ability to capture multi-scale patterns with spatial selectivity and adaptive weighting of thermal channels. This fusion reduces noise and environmental interference, improving segmentation accuracy even under variable radiation conditions.

Furthermore, the use of a MobileNetV2 encoder allows the number of parameters and FLOPs to be limited, ensuring real-time inference on UAV or embedded platforms.

Finally, the network has been designed to be integrated into a predictive maintenance context, correlating segmented IR maps with the system's electrical data, thus overcoming the traditional separation between visual diagnostics and performance analysis.

1.4.5. Long Short-Term Memory Networks and electrical components analysis

IRT is extremely useful for monitoring and preventive maintenance of electrical equipment. It allows early detection of thermal anomalies

caused by loose connections, current overloads, phase imbalances or insulation degradation. Thermographic inspections are used on a wide range of components, such as electrical switchboards, circuit breakers, busbars, power cables, transformers, and electric motors. Further applications include inverters and static converters (inverters, DC/DC converters), uninterruptible power supply systems (UPS systems) and storage systems (battery modules). In addition to images, condition monitoring of electrical components makes use of the analysis of electrical signals (current, voltage, power), providing an integrated approach capable of correlating thermal anomalies with electrical phenomena such as load imbalances, increased contact resistance, efficiency variations or high losses.

Recurrent neural networks (RNNs) are used in this field, in particular their LSTM (Long Short-Term Memory) and GRU (Gated Recurrent Unit) variants, which are designed to model time series data.

LSTM networks store long-term dependencies and filter out noise and short-term fluctuations, making them ideal for predicting:

- short-term energy production (15–60 minute forecasting);
- battery state of charge (SOC) trends;
- dynamic anomalies in electrical parameters that can anticipate failures in modules or inverters [58].

In many studies, CNNs and LSTMs are combined in hybrid CNN-LSTM architectures, where the former extract spatial features (from images or spectral signals) and the latter model temporal dynamics. The combination of CNN and LSTM allows the spatial and temporal dimensions of the data to be modelled simultaneously, paving the way for multimodal predictive diagnostic systems based on IR images and synchronous electrical signals [59].

Other contributions have exploited IR thermography for predictive maintenance of industrial components, using CNN to automatically identify hotspots and abnormal dissipation with an accuracy of close to 92%, confirming the effectiveness of non-destructive methods [60].

A comparative analysis of fault prediction methods highlighted the advantages of LSTM over DNN and SVM, thanks to its ability to handle noisy and non-stationary signals, achieving 89% precision [5].

Subsequently, lightweight CNN models applied to low-resolution thermal images showed remarkable results in the recognition of faults in rotating machinery, with 97% accuracy, reducing inference time and computational complexity [61]. The combined use of wavelet transform and multilayer LSTM also improved electricity consumption forecasting, reducing the mean percentage error thanks to the multi-frequency decomposition of time series [62].

Further research has developed image analytics pipelines for automatic thermal segmentation in complex industrial environments, achieving mIoU = 74% and F1-score = 86%, improving the robustness of the analyses compared to manual methods [63]. At the same time, attention has shifted to the management of unbalanced datasets, a

crucial issue for increasing diagnostic accuracy in real-world scenarios [64].

Among the most mature approaches are those based on U-Net, now considered the standard in semantic segmentation of IR images. In applications on conveyor belts and industrial plants, U-Net has achieved meanPA=99.25% showing excellent performance in operational scenarios [65]. In another study, a method for diagnosing thermal faults in substations was proposed, using a lightweight convolutional neural network based on U-Net, with an improvement in mIoU of between 1.5% and 8% compared to other approaches, using a reduced dataset without overfitting [66].

Finally, the latest investigations into predictive asset management of switchgear have highlighted the effectiveness of AI in improving safety and reducing equipment downtime [67].

Despite the progress described, most previous studies maintain a separate approach between thermographic analysis and electricity consumption forecasting, limiting the possibility of directly correlating the two dimensions of the phenomenon. Furthermore, real-time implementations on economical platforms remain difficult to achieve.

The work described in this thesis, in Chapter 4, introduces a multimodal and integrated solution that merges temporal and spatial data into a single predictive framework [68].

The LSTM-U-Net (L-UN) model uses an LSTM network to predict hourly current absorption and a U-Net to segment IR thermal images, automatically identifying overheated areas.

The system, implemented on Raspberry Pi and Arduino, achieves MSE = 0.005, MAE = 0.03, MAPE = 3.5% for consumption prediction and IoU = 0.82, F1-score = 90.1% for thermal segmentation.

Compared to previous models, the combination of the two domains (temporal and spatial) allows for a 20% reduction in unnecessary shutdowns, improving the predictive management of electrical panels and overall energy efficiency.

1.4.6. Challenges and prospects

The main challenges for the application of AI in condition monitoring of PV systems and other electrical components concern:

- the availability of large annotated datasets, especially in real conditions;
- the generalisation of models with respect to environmental variability (irradiation, wind, reflections);
- the explainability of decisions (Explainable AI), which is essential for regulatory recognition in industrial contexts;
- computational scalability, necessary for implementation on drones or embedded systems in the field.

Recent research is addressing these critical issues through physically consistent data augmentation, lightweight models and integration with PV digital twins, which allow the thermal evolution of defects to be

simulated and the parameters of AI models to be dynamically adapted during operation.

1.5. EMS and PdM in Hybrid MG

1.5.1. Architectures, operating principles, control approaches and PQ assessment

A MG is a local electricity network that integrates distributed energy resources (DER), storage systems and controllable loads, capable of operating both connected to the main grid (grid-connected) and in isolated mode (islanded) [69].

The main objective is to ensure reliability, power quality and energy optimisation, maximising self-consumption of renewable sources and reducing operating costs.

The shift towards a decarbonised and digitalised energy paradigm is promoting the spread of hybrid AC/DC MG. They combine both AC and DC lines and converters, allowing PV generators, batteries and DC loads (e.g., LEDs, servers, electric vehicles) to be connected directly, reducing the number of conversions and overall losses [70].

The typical architecture of a hybrid MG includes:

- RES generation subsystems (PV, wind, fuel cells);
- electrochemical storage systems (Li-ion or Na-S batteries);
- bidirectional DC/DC and DC/AC converters with vector control;
- a Point of Common Coupling (PCC) that regulates power exchanges and quality;
- Energy Management System (EMS) as the upper level control.

In a MG, energy flows are coordinated by an EMS, which acts as a supervisory and optimisation layer. The EMS manages production from renewable sources, battery state of charge (SOC), exchanges with the main grid and load priorities, pursuing multiple objectives such as minimising operating costs and conversion losses, maximising local self-consumption, maintaining PQ parameters within regulatory limits and extending the useful life of devices [71].

1.5.2. EMS structure and control levels

The EMS is the "brain" of the MG, responsible for coordinating resources and optimising energy use based on operational variables and multiple objectives (cost, efficiency, emissions, comfort, reliability).

The EMS optimisation functions include:

- power dispatch between renewable sources, batteries and the main grid;
- battery state of charge (SOC) management to maximise useful life;

- reduction of imported energy costs, considering dynamic tariffs and hourly prices;
- maintaining PQ indices within regulatory limits.

Maintaining PQ is a fundamental requirement for system stability and reliability. Standards EN 50160, IEC 61000-3-6 and IEEE 519-2014 define the permissible limits for voltage deviations (ΔV), frequency (Δf), total harmonic distortion (*THD*) and Total Demand Distortion (*TDD*), setting typical values of ±10 % for voltage, ±1 % for frequency and $THD < 5$ % for LV networks [69, 70]. Compliance with these limits is complex in the presence of unpredictable distributed generation and dynamic loads: for this reason, advanced control systems are required that are capable of compensating for imbalances and mitigating disturbances in real time.

In grid-connected conditions, the EMS regulates bidirectional exchange with the grid (import/export) and the power factor (*PF*), while in islanded mode it ensures voltage and frequency stability through droop control strategies and virtual power reserve.

In general, the EMS is structured on three levels [73]:

I. Primary level (local control) – manages voltage and frequency regulation using converters and inverters.
II. Secondary level (coordinated control) – stabilises the system by compensating for deviations (ΔV, Δf) and ensuring proportional load sharing between generators.
III. Tertiary level (energy management or supervision) – plans the dispatch of resources based on economic signals, generation forecasts, state of charge and load priorities.

The tertiary level, the core of the EMS, can be implemented through different control and optimisation approaches. Recent systematic reviews have highlighted the increasing complexity introduced by RES, static converters and electronic loads [74].

Hybrid AC/DC MGs reduce multiple conversions and losses, improving compatibility with renewable sources and electronic loads [75]. Comparative analyses have shown that the inclusion of a DC bus significantly reduces conversion losses and stabilises voltages at the nodes [76].

Other contributions have shown that coordination between AC and DC subsystems and the use of storage can compensate for energy overproduction and deficits, improving voltage and frequency stability [77].

For the optimal management of such networks, several EMS approaches have been developed, which can be summarised in four main categories, as described in Table 3.

Table 3. Summary of main EMS control approaches for hybrid AC/DC microgrids, highlighting their operating principles and main advantages

Approach	*Brief Description*	*Main Advantages*
Deterministic (rule-based, fuzzy) [78]	Predefined rules based on *SOC* thresholds, tariff, and PV power	Simplicity, robustness, real-time operation
Mathematical optimization [79]	Formulated as an Optimal Power Flow (OPF) or Mixed-Integer Linear Programming (MILP) problem	Optimal solutions, but high computational cost
Metaheuristic algorithms (GA, PSO, DE) [80]	Nature-inspired algorithms for multi-objective optimization	Flexibility, good global convergence
Machine learning /AI-based[81]	EMS based on neural networks, multi-agent systems, or reinforcement learning	Predictive and adaptive capability

Studies on PV-WT-BESS MGs have shown that fuzzy controls reduce oscillations and improve stability with lightweight architecture [82]; in residential DC MGs, fuzzy-EMS with HESS ensure robust charge/discharge management [83]. Model Predictive Control (MPC) approaches formulate the problem as constrained optimisation, coordinating resources and PQ constraints; however, they are sensitive to model errors and computationally heavy [84].

In recent years, Reinforcement Learning (RL) and its deep extensions (DRL) have introduced self-adaptive control policies capable of learning optimal strategies in the presence of uncertainty about RES and energy prices [85].Despite promising results, long training times and poor interpretability limit their industrial deployment. In parallel, the issue of PQ has been addressed by several studies that have analysed the impact of islanded mode on *THD* and voltage stability, suggesting the integration of filters and compensators in EMS control [86]. However, such strategies increase architectural complexity and require additional hardware resources. Recent work has explored hybrid fuzzy-MPC or fuzzy-RL strategies that combine robustness and adaptability, but these often remain validated only in simulation and not on real-time platforms [87].

An overall analysis of the literature shows that the simultaneous integration of PQ indicators (ΔV, Δf, THD_V, *TDD*) and dynamic tariff signals in the tertiary level remains an open and strategic research topic.

A comparative analysis of the most recent work on EMS in hybrid AC/DC MGs highlights some structural limitations that hinder its actual adoption.

Mathematical optimisation-based approaches (OPF, MILP, MPC) provide accurate solutions but are computationally expensive and heavily dependent on accurate models of system dynamics. In the presence of uncertainties related to renewable resources and variable loads, such models become difficult to calibrate, making implementation on embedded platforms and in real-time applications complex [77].

Solutions based on ML and RL (ANN, RL, DRL) introduce predictive and adaptive capabilities, but have long training times, require extensive datasets and lack decision transparency, all of which limit their transferability and industrial validation [79].

Fuzzy and neuro-fuzzy approaches, while offering computational lightness and interpretability, often treat PQ in a simplified manner, focusing on energy balance and SOC. Only rarely are AC/DC PQ indices (ΔV, Δf, THD_V, TDD) and dynamic tariff signals integrated into the same inferential logic [88]. Furthermore, the lack of common benchmarks and hardware-in-the-loop validations limits the comparability of results [89].

The research presented in this thesis proposes a Mamdani fuzzy EMS for hybrid AC/DC MGs that integrates AC/DC PQ indices, state of charge (SOC) and dynamic tariff signals into a single inferential structure, allowing simultaneous optimisation of technical (ΔV, Δf, THD_V, TDD) and economic (import/export cost) parameters.

The approach is characterised by low computational complexity, robustness to operational variations and decision-making transparency, features that make it suitable for real-time execution and implementation on embedded platforms. The linguistic formulation of fuzzy rules also allows for clear interpretation of EMS decisions, overcoming the "black-box nature" of AI methods.

The model is validated on a hybrid PV–WT–PEMFC–BESS MG with AC/DC loads, showing joint improvements in power quality and operating cost in compliance with EN 50160, IEC 61000 and IEEE 519 standards.

In summary, the proposed system combines computational efficiency, regulatory compliance, and application scalability, bridging the gap between high precision but heavyweight methods (MPC, DRL) and lightweight but limited methods (traditional fuzzy), representing a balanced and industrially applicable solution for energy management and predictive maintenance of hybrid MGs.

1.6. Scientific goal and original contributions

The energy transition in the EU context requires increasingly reliable, integrable and intelligent PV systems capable of ensuring service continuity and maximum efficiency in distributed generation contexts. However, the growing complexity of the plants, the variability of operating conditions and the proliferation of small-scale sites make maintenance based on manual inspections or traditional periodic measurements impractical.

In this scenario, the combined use of IRT and AI represents a technological frontier of great interest, as it allows for rapid, non-destructive, and automatable diagnostics, laying the foundations for truly scalable PdM integrated with MG management.

This thesis therefore lies at the intersection between advanced monitoring of PV systems and electrical components and intelligent control of AC/DC hybrid MGs, with the aim of unifying the two areas through a coherent methodological platform based on data analysis, physical modelling, and efficient neural architectures.

The research activity described in this thesis is structured around three macro-objectives:

i. Development of an automatic diagnostic methodology for the detection and classification of defects in PV modules using thermographic images acquired in the field, compliant with international standards (IEC TS 62446-3) and robust under variable environmental conditions.
ii. Design and validation of efficient CNN architectures for PdM optimisation of PV plants and electrical components. Those models are capable of combining segmentation accuracy and computational lightness, for applications on edge devices and UAV platforms.
iii. Integration of diagnostic information into the energy control of a hybrid AC/DC MG through an EMS based on fuzzy logic and predictive techniques, to optimise energy dispatch, improve PQ and reduce operating costs.

These objectives aim to bridge the gap that still exists between PV and electrical components diagnostics and distributed system management, providing a replicable framework for the intelligent monitoring of renewable generators.

The main scientific and technological contributions achieved can be summarised as follows:

- Definition of a multi-class thermographic dataset of real PV modules, annotated according to IEC guidelines and comprising six categories of class defects (normal, hotspot, bypass diode fault, substring fault, soiling/shading, glass damage).
- Development of the Efficient Attentive U-Net architecture, which integrates MobileNetV2 encoders, AGs, SE modules and ASPP, achieving an optimal balance between accuracy and complexity.
- Cross-domain methodological extension to other electrical elements through IRT, developing a hybrid LSTM+U-Net model for monitoring the SoH of industrial electrical switchboards, demonstrating the transferability of the AI + IRT paradigm.
- Modelling and simulation in MATLAB/Simulink of a hybrid AC/DC MG, with implementation of a fuzzy tariff-aware EMS that interacts with the AI diagnostic module to optimise PQ and costs.
- Integrated analysis between diagnostics and dispatch for PQ optimisation.

2. Thermographic Campaign and PV Dataset Construction

The experimental campaign conducted at the DICEAM Department, University "Mediterranea" of Reggio Calabria provided the database for training and validating the AI architecture proposed in this work. The chapter describes in detail the configuration of the PV system under study, the instrumentation used for thermographic measurements, the environmental conditions of acquisition in accordance with IEC TS 62446-3:2017, the pre-processing and normalisation phases of the images, as well as the annotation and class balancing procedure.

2.1. Description of the PV system

The PV system under analysis is located at the Energy and Environment Laboratory of the DICEAM Department, University "Mediterranea" of Reggio Calabria, in Via Rodolfo Zehender (geographical coordinates: 38.1093° N, 15.6430° E) (Figure 1).

Figure 1. PV system under examination, located at the DICEAM Department, University "Mediterranea" of Reggio Calabria, in Via Rodolfo Zehender.

It is an ideal test bed for experimenting with predictive diagnostic methodologies in real operating conditions, as the site is characterised by high average annual insolation and an urban environment free of obstacles that could cause accidental shading.

The plant is installed on naturally sloping ground, facing south, and inclined at approximately 38°, which is the optimal value for the site's latitude and for maximising energy production throughout the year. The total nominal power is 150 kWp, consisting of polycrystalline modules

with a unit power of 250 W arranged in strings of 20 units each. The strings are connected to three-phase inverters, ensuring DC/AC conversion and connection to the local 400 V grid.

The plant area faces south (azimuth 0°) with an average inclination of 30°, consistent with the geographical latitude of the site (38°N). The mounting conditions favour natural heat dissipation and allow for optimal inspection using a front-view thermal camera.

During the campaign, measurements were taken at different times of the day to analyse the thermal stability of the modules and the evolution of surface defects. The PV system, selected as a case study, consists of 18 SunPower X Series panels: X22-360-COM [90] and has the characteristics shown in Table 4.

Table 4. Electrical data of the PV system under investigation.

Electrical characteristics	*Values*	*Unit of measurement*
Nominal power	360	W
Power tolerance	+5/0	%
Module efficiency	22,1	%
Voltage at maximum power point	59,1	V
Current at maximum power point	6.09	A
Open circuit voltage (Voc)	69.5	V
Short circuit current (Isc)	6.48	A
Maximum system voltage	1000 IEC & 1000 U	V
Maximum fuse current	15	A
Power temperature coefficient	-0.29	%/ °C

This installation was chosen because it represents a typical medium-sized PV system in which fault detection has a direct impact on overall energy yield and operational reliability. In particular, the system had already shown signs of performance degradation during preliminary inspections, making it a suitable candidate for testing thermographic and AI-based diagnostic methodologies.

The monitoring campaign, carried out while the PV system was operating under normal grid connection conditions, ensured that all measurements reflected the realistic thermal and electrical behaviour of the modules. The normal operation of the system allowed the acquisition of thermographic data under load, revealing temperature anomalies associated with defects such as hot spots, bypass diode failures or cell interconnection problems. The measurement campaign, performed on the grid-connected PV system under load conditions, ensured realistic data acquisition directly linked to actual energy losses. In fact, several studies have shown that thermal signatures are often attenuated or even absent when modules are tested in open circuit, while load conditions generate current imbalances that amplify localised heating [91]. This approach therefore ensures that the anomalies recorded are not only visible from a thermal point of view, but also directly related to actual energy losses, making the dataset particularly suitable for evaluating predictive maintenance strategies in terms of energy efficiency.

2.2. Instrumentation description and environmental parameters

The thermographic survey stems from the need to collect high-quality infrared (IR) images of PV modules under realistic operating conditions, with the aim of capturing both normal and abnormal behaviour. The measurements were taken using a FLIR SC660 radiometric IR camera with a thermal sensitivity of approximately < 50 mK, a spectral response in the 7.5-14 µm range and a detector resolution of 640 × 480 pixels (miniaturised bolometer) [92]. The uncooled microbolometer sensor ensures stability in environmental measurements, while the dual recording mode (radiometric and JPEG) allows for quantitative thermographic analysis. NIST-traceable calibration ensures adherence to metrological standards. These specifications ensured the ability to detect small temperature gradients, which are essential for identifying early-stage hot spots or subtle interconnection defects. Monitoring was conducted during periods of stable irradiation, typically in the middle of the day, when the modules were operating at or near maximum power. Environmental conditions, including solar radiation, air temperature, and wind speed, were monitored simultaneously using a pyranometer and a weather station to ensure consistent acquisition conditions. Measurements were taken with the PV system under electrical load, as thermal anomalies are most evident when current flows through defective cells or bypass diodes. The camera was placed 3–5 m from the modules and angled to minimise reflections and ensure full field coverage. The thermographic inspection campaign has been performed following the principal international requirements for PV field testing. Specifically, the IEC TS 62446-3 prescribes the requirements for IRT measurements on PV module and array samples under field operating conditions, obtaining reproducibility and comparability of results. Additional guidelines of IEC 61215 (design qualification and type approval of crystalline module), IEC 61730 (PV module safety qualification), and UNI EN ISO 9712 (qualification of non-destructive testing personnel) have been also taken into consideration to ensure technical reliability and operator conformity.

According to IEC TS 62446-3, thermographic inspections should be done when the sky is clear. The modules should get direct sunlight of at least 600 W/m² (preferably above 700 W/m²) to see enough difference in temperature between broken and normal cells. The wind speed should be under 4–5 m/s because wind can cool the temperature differences that help find problems. The ambient temperature and humidity must be watched all the time, as these two things affect how well IR light passes through the air and how accurate the calibration is. The thermographic inspection was carried out using the traditional method of manual thermography, walking around the PV site and inspecting each module with the thermal imaging camera. The thermographic acquisitions were carried out over a period of two months, from mid-April to mid-June

2025. Table 5 defines the statistical distribution of the main environmental parameters recorded during the IRT campaign, compliant with the IEC TS 62446-3 standard.

Table 5. Statistical summary of environmental conditions during the infrared thermographic campaign (April–June 2025).

Parameter	*Symbol / Unit*	*Min*	*Max*	*Mean ± SD*	*IEC TS 62446-3*
Solar irradiance	*G* (W/m²)	610	890	742 ± 86	≥ 600 W/m²
Ambient temperature	*Tamb* (°C)	18	27	22.3 ± 2.8	15 – 35 °C
Relative humidity	*RH* (%)	55	72	63.9 ± 5.3	< 75 %
Ambient wind speed	v_w (m/s)	0.5	3.8	2.1 ± 0.9	< 5 m/s
Cloud coverage	*C* (oktas)	0	2	0.8 ± 0.6	≤ 2 oktas

In total, 500 thermographic images were collected on different days and under different environmental conditions. The raw thermographic data were stored in radiometric format, preserving pixel-level temperature information.

This was essential for subsequent pre-processing and normalization, as well as for accurate annotation of fault regions. Representative examples of the acquired thermal images are shown in Figure 2, where typical fault patterns such as hot-spots, shading effects, and soiling are clearly visible.

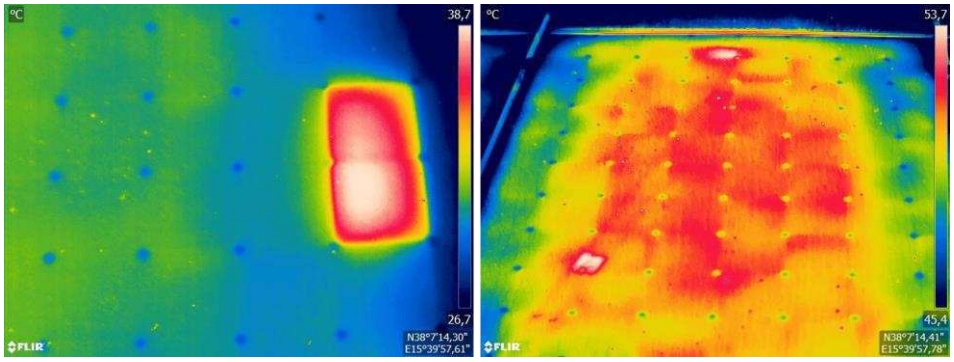

Figure 2. IR example images collected with FLIR SC660 thermal camera.

2.3. Dataset

The test dataset considered in the present work consists of IRT images of PV modules that were captured through a focused inspection campaign. It was taken in actual operating conditions, thus ensuring that the environmental and the irradiance profile truly represented typical field conditions.

Out of the collected thermograms, the images that totalled 100 original thermograms were selected as representative samples including different defect types as well as normal modes of operation.

They were all captured at native resolution, which was 640 × 480 pixels, in pseudo-RGB format, wherein the thermal intensity values were mapped into a three-channel colormap both for visualization and subsequent processing.

2.3.1. Data annotation

The dataset was annotated on a pixel-wise basis, assigning each pixel to one of six predefined classes relevant for PV fault detection: (1) background/normal module, (2) hotspot, (3) bypass diode fault, (4) substring fault, (5) soiling/shading, and (6) glass damage. The annotation process was performed manually with expert supervision to ensure accuracy and consistency across images, following established guidelines in thermographic PV diagnostics.

The thermographic images collected during inspections of PV systems showed anomalies on specific cells. For this reason, each of these images was subsequently associated with a multi-coloured mask, in which the white pixels identify the cells considered anomalous.

The identification of abnormal cells is based exclusively on thermal data. In fact, the operator can immediately recognise the location of the anomaly thanks to the clear deviation in the cell temperature compared to the surrounding cells.

Based on evidence provided by scientific literature and field inspections, five representative categories of defects were considered, as shown in Table 6.

Table 6. Description of the six annotated classes in the PV thermographic dataset.

Class ID	*Class Name*	*Description of Anomaly*	*Typical Visual Appearance in IR Images*
1	Background / Normal	Areas of the module without observable thermal anomalies	Uniform temperature distribution, homogeneous pseudo-RGB colour
2	Hotspot	Localized overheating due to defective cells or soldering	Small bright spots with higher intensity compared to surroundings
3	Bypass diode fault	Failure or malfunction of bypass diodes causing string-level anomalies	Larger regions with abnormal heating pattern
4	Substring fault	Partial malfunction of cell substrings	Linear overheated regions aligned with substrings
5	Soiling/Shading	Dirt, dust, bird droppings, or shading from external objects	Irregular cooler or warmer patches depending on irradiance
6	Glass damage	Surface cracks or mechanical stress on protective glass	Irregular fragmented patterns with sharp temperature contrasts

Each of these types of faults has a direct and quantifiable impact on the energy yield of the affected module string, ranging from slight reductions in efficiency to severe power losses of more than 70% in the case of extensive hot spots or defective bypass diodes. Each of them is identified by an RGB colour described in Table 7.

Table 7. RGB colour identification for each classes of the IR dataset.

Class	*Description*	*RGB Color*
0	Background	Black (0, 0, 0)
1	Hotspot	Green (0, 255, 0)
2	Bypass diode fault	Red (255, 0, 0)
3	Substring fault	Cyan (0, 255, 255)
4	Soiling / Shading	Blue (0, 0, 255)
5	Glass damage / Bird dropping	Yellow (255, 255, 0)

The central role of thermography in identifying defects in PV modules allows for the rapid detection of hotspots, diode failures, and damaged cells directly in the field, facilitating more efficient maintenance [91, 92]. The use of machine learning algorithms, combined with thermal images captured by drones, improves the automatic classification of defects, provided that the dataset is well annotated [95]. However, the reliability of thermographic analysis can be influenced by environmental variables, and, in some cases, additional checks are necessary to avoid false positives. For these scientific reasons, the set of thermographic data collected during the measurement campaign was annotated and a pixel-level segmentation approach was adopted, in which defective regions were delineated using polygonal masks on radiometric thermal images. This annotation strategy ensured the generation of ground-truth segmentation masks corresponding to each defect category, providing the basis for multi-class semantic segmentation. In addition to defective areas, areas corresponding to intact cells were also annotated, allowing the model to learn a balanced distinction between anomalies and normal operating conditions.

The acquired thermographic images were initially saved in JPG format and then the 100 most significant images were loaded into LabelMe© software, which was used to perform a manual semantic segmentation process. Since raw thermal images are affected by variations in ambient temperature, radiation levels and acquisition geometry, radiometric normalisation was applied first [96]. For each image, polygons were drawn to identify and delimit areas corresponding to potential faults or thermal defects, assigning each polygon a semantic label describing the type of defect observed.

LabelMe© then saved this information in annotation files in JSON format, which contain the geometric data relating to the polygons traced, the labels assigned and references to the source image [97]. This process transformed the visual information contained in the JPG images into a structured, machine-readable format, which is essential for

subsequent statistical analysis, automated processing, or training of defect classification algorithms.

The images in Figure 3 show some examples of manual segmentation performed with LabelMe© software. They show polygons drawn on areas of the PV module that have potential thermal defects, such as hotspots, soiling, shadows, or diode malfunctions. Each polygon is associated with a specific semantic label, which allows the different types of anomalies present in the data to be systematically classified.

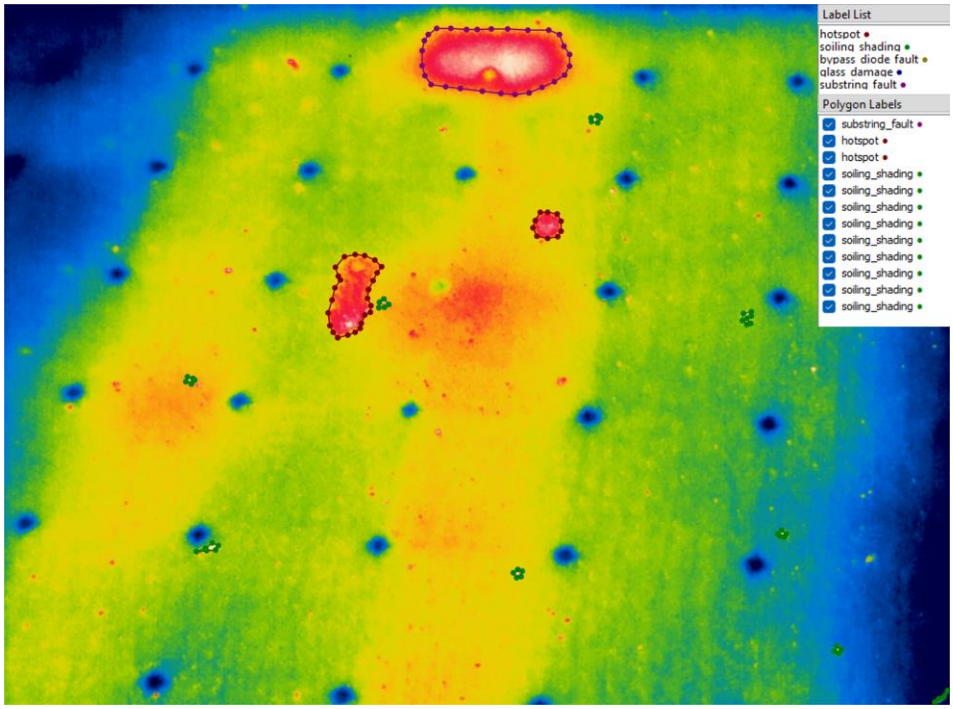

Figure 3. Manual annotation process of the six annotated classes in the PV thermographic dataset through LabelMe© software.

Although manual annotation allows for accurate, customised masks for each image, the segmentation phase of thermographic images requires a significant investment in terms of time and resources, especially when working with large data sets [98]. Segmenting thermal defects is challenging because blurred contours and artefacts can mislead even expert operators. This operation reduced the influence of environmental fluctuations and ensured that thermal contrasts due to defects remained comparable between different acquisition sessions. By explicitly linking each annotated defect to its potential energy impact, the dataset provided not only a solid training basis for the proposed DL model, but also a reference framework for evaluating diagnostic accuracy.

2.3.2. Class distribution

Each thermogram was manually annotated on a pixel-wise basis using six semantic classes representing the main categories of PV defects: background, hotspot, bypass diode fault, substring fault, soiling/shading, and glass damage. The annotation process was performed under expert supervision to ensure consistency across images. Table 8 summarizes the class distribution in the original dataset of 100 thermographic images. The statistics report the total number of pixel occurrences per class and their relative percentage with respect to the total dataset. Although the data augmentation process (Section 2.3.3) expanded the dataset to 400 images, it preserved the same class proportions, ensuring a balanced distribution among training, validation, and test folds.

Table 8. Pixel-wise class distribution in the original dataset (100 IR images).

Class ID	*Class Name*	*Number of Occurrences (pixels ×10⁴)*	*Percentage (%)*	*Description*
1	Background / Normal	9,420	85.3	Module areas without defects
2	Hotspot	300	2.7	Localized overheating due to defective cells
3	Bypass diode fault	240	2.2	String-level heating pattern
4	Substring fault	80	0.7	Partial malfunction of cell substrings
5	Soiling/Shading	810	7.3	Dirt or shadows on the surface
6	Glass damage	200	1.8	Cracks or surface delamination
–	**Total**	**11,050**	**100.0**	–

As expected, the background pixels dominate the dataset (85.3% of the total percentage).

2.3.3. Pre-Processing and Data augmentation

To enable model training using architectures with pretrained backbones, all images were resized to 224×224 pixels, which is a standard input size compatible with lightweight CNN encoders such as MobileNetV2 and with downsampling and upsampling operation, as it is a multiple of 32 [99]. While 224 × 224 served as the baseline resolution, additional experiments were conducted at 256 × 256 to evaluate the impact of higher spatial resolution on the detection of small-scale defects. In both cases, the original three-channel format was preserved to fully exploit the pseudo-RGB thermal representation.

Prior to training, all images underwent a pre-processing pipeline designed to enhance the visibility of defects and to normalize the input data for robust learning. A denoising filter was first applied to reduce sensor-induced noise while preserving structural details of the module surface [100]. This was followed by pixel intensity normalization to standardize the dynamic range of thermal values across the dataset, ensuring consistency among different acquisitions and operating conditions. The normalization step is particularly important for thermographic data, as it reduces the influence of varying irradiance or ambient temperature on the model's predictions [101].

To increase the dataset size and improve variability, data augmentation techniques were applied, resulting in an expanded dataset of 400 images. Standard geometric transformations included random horizontal and vertical flips, as well as rotations at fixed angles (90°, 180°, 270°) to simulate different module orientations. Additional augmentations were applied to reproduce realistic variations in thermographic inspections:

- Brightness and contrast adjustments, emulating changes in irradiance, sensor calibration, or module emissivity.
- Gaussian noise injection, simulating thermal sensor disturbances.
- Random erasing and partial occlusions, reproducing effects of soiling, shading, or dirt accumulation on the module surface.
- Elastic and affine transformations with small intensity, introducing geometric variability while avoiding distortion of fine structural details.

All augmentations were applied with controlled probabilities to maintain a balance between dataset diversity and fidelity to real operating conditions. The augmentation pipeline expanded the dataset from 100 original images to 400 samples, ensuring that each fold in the validation process included a representative distribution of defect types.

To preserve the integrity of model evaluation, a strict anti-leakage policy was enforced. Dataset partitioning into training, validation, and test sets was performed on the original 100 images before augmentation. Consequently, all augmented variants derived from a single original thermogram were assigned exclusively to the same fold, preventing data leakage across different subsets. This strategy ensured that the test sets only contained unseen images, thereby providing a reliable measure of model generalization. Figure 4 shows an example of data augmentation techniques applied on a PV thermal image.

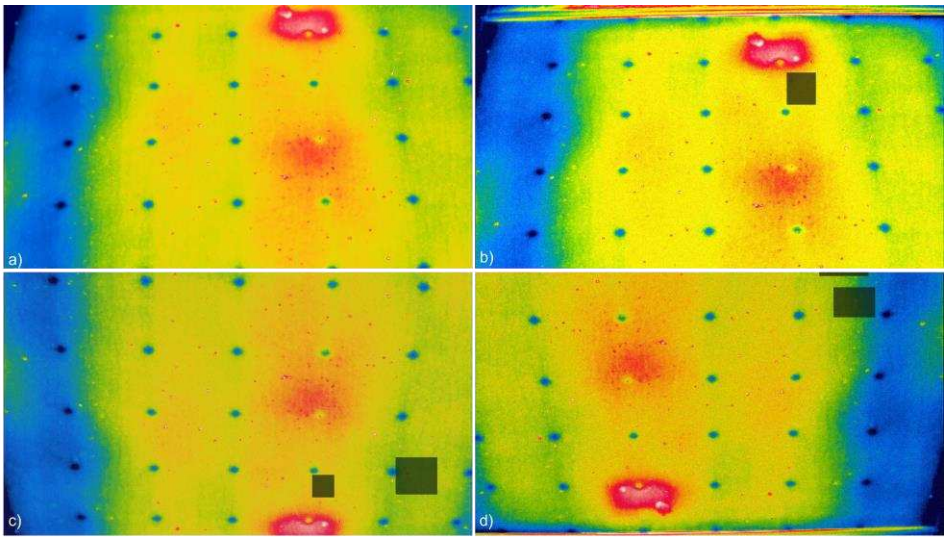

Figure 4. Data augmentation for PV IR images: (a) original frame; (b–d) three variants using fixed rotations/flips, mild brightness–contrast jitter, Gaussian noise, and small occlusions to emulate orientation, irradiance changes, and soiling while preserving panel structure.

The resulting dataset, comprising the augmented and annotated thermograms, served as the foundation for all subsequent training and evaluation of the proposed AI model descripted in the next chapter.

3. AI Architecture for Photovoltaic Fault Diagnosis

This chapter describes in detail the proposed convolutional neural network architecture, called Efficient Attentive U-Net, developed for multi-class semantic segmentation of PV defects identified by IRT.

The goal is to provide a lightweight but accurate model capable of operating in real time on embedded or edge platforms while maintaining high levels of accuracy and generalisation.

The design of the model was guided by three fundamental principles:

i. Computational efficiency achieved using a pre-trained MobileNetV2 encoder.
ii. Spatial focus capability, ensured by the introduction of AG modules.
iii. Sensitivity to discriminating information channels, achieved through SE blocks and ASPP modules in the bottleneck.

3.1. Proposed DL Architecture: Efficient Attentive U-Net

The proposed DL model, referred to as Efficient Attentive U-Net, was designed to achieve a favourable trade-off between segmentation accuracy and computational efficiency, with a particular focus on enabling real-time deployment in UAV-based inspections and edge-computing scenarios. The architecture builds upon the standard U-Net encoder–decoder structure while integrating several improvements that enhance feature representation, attention to relevant regions, and multi-scale context aggregation.

At its core, the encoder is based on MobileNetV2, a lightweight convolutional neural network pretrained on ImageNet. MobileNetV2 employs depth wise separable convolutions and inverted residual blocks, which drastically reduce the number of parameters and floating-point operations (FLOPs) while preserving the ability to extract discriminative features. This choice makes the architecture significantly more compact compared to encoders such as VGG or ResNet, and therefore more suitable for real-time inference on resource-constrained hardware. To further improve the model's capability to detect small and irregular anomalies in PV modules, AGs were integrated along the skip connections between encoder and decoder. These gates learn to suppress irrelevant activations from the background and to highlight thermally anomalous regions such as hotspots or cracks. The attention mechanism ensures that the decoder focuses on features most relevant to the segmentation task, thereby reducing false positives in large uniform background areas. In addition, SE blocks were incorporated in

the skip pathways to adaptively recalibrate channel-wise feature responses. By emphasizing informative channels and suppressing redundant ones, the SE mechanism enhances the discriminative power of the feature maps passed to the decoder. This is particularly useful in thermographic images, where subtle variations in intensity may carry significant diagnostic information.

The bottleneck stage of the network includes an ASPP module, which applies parallel dilated convolutions with different dilation rates. This design allows the model to capture both fine-grained details and larger contextual patterns, enabling robust segmentation of defects that vary in size and shape. The ASPP module enriches the receptive field of the bottleneck without substantially increasing the computational burden.

The decoder reconstructs the full-resolution segmentation map by progressively upsampling the encoded features. Skip connections from the encoder, refined through AGs and SE blocks, are concatenated with the decoder features at corresponding resolutions. Convolutional layers with reduced filter sizes are used in the decoder to maintain a lightweight structure. The final output layer applies a softmax activation function to produce a dense pixel-wise classification into the six predefined classes.

A detailed description of the network configuration is provided in Table 9, which summarizes the main layers, their output dimensions, kernel size, stride, and padding, assuming an input resolution of 224 × 224 × 3.

Table 9. Layer configuration of the proposed Efficient Attentive U-Net (input size: 224 × 224 × 3).

#	*Layer / Block*	*Output Dimensions*	*Kernel Size*	*Stride*	*Padding*
1	Input	224 × 224 × 3	–	–	–
	Encoder (MobileNetV2 backbone)				
2	Conv2D + BN + ReLU6	112 × 112 × 32	3 × 3	2	1
3	Inverted Residual Block ×2	112 × 112 × 16	3 × 3	1	1
4	Inverted Residual Block ×3	56 × 56 × 24	3 × 3	2	1
5	Inverted Residual Block ×4	28 × 28 × 32	3 × 3	2	1
6	Inverted Residual Block ×3	14 × 14 × 64	3 × 3	2	1
7	Inverted Residual Block ×3	7 × 7 × 96	3 × 3	1	1
8	Bottleneck (ASPP module)	7 × 7 × 256	{1, 3, 5, pooling}	–	same
	Decoder				
9	Upsampling + Conv (skip + AG + SE)	14 × 14 × 128	3 × 3	1	1
10	Upsampling + Conv (skip + AG + SE)	28 × 28 × 64	3 × 3	1	1

11	Upsampling + Conv (skip + AG + SE)	56 × 56 × 32	3 × 3	1	1
12	Upsampling + Conv (skip + AG + SE)	112 × 112 × 16	3 × 3	1	1
13	Upsampling + Conv	224 × 224 × 16	3 × 3	1	1
14	Output Softmax Layer	224 × 224 × 6	1 × 1	1	0

The overall architecture is illustrated in Figure 5, which schematically represents the MobileNetV2 encoder, the attention-enhanced skip connections with SE blocks, the ASPP bottleneck, and the lightweight decoder that reconstructs the final segmentation masks.

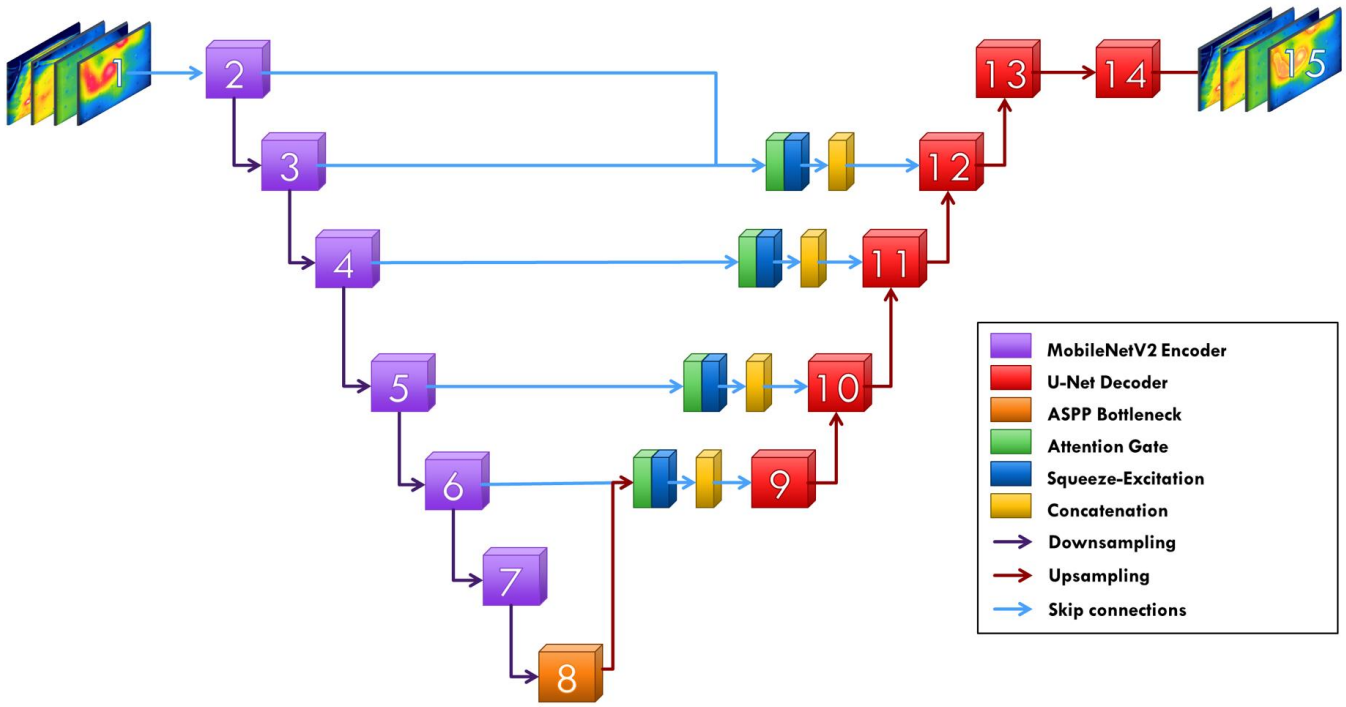

Figure 5. Schematic diagram of the proposed Efficient Attentive U-Net architecture, showing the MobileNetV2 encoder on the left, skip connections refined by Attention Gates (AG) and Squeeze-and-Excitation (SE) blocks, the ASPP bottleneck, and the lightweight decoder producing the final six-class segmentation map

3.1.1. Validation Protocol and Training Setup

The study presents a validation and training system to ensure performance is measured reasonably and reproducibly. Due to the relatively small dataset, we used a nested 5×2 cross-validation (CV) framework, which contributed to a robust hyperparameter estimation along with a reasonable out-of-sample performance estimate.

The dataset in the outer loop, meticulously divided into five segments, presents each segment with an appropriate mixture of the six labelled classes. During each iteration, the model was trained on four segments (90% of the data), and the last segment (10%) was kept as a separate test set. The process was repeated five times so that each sample was tested exactly once. The outputs of the outer cycle were then averaged, and the standard deviations were calculated as a measure of how much they deviated.

The model used 2-fold internal cross-validation on each external training partition during hyperparameter search. The internal cycle during the search for the following parameters is:

- Learning rate (LR): {1e−3, 5e−4, 1e−4};
- Weight decay (WD): {1e−4, 5e−5};
- Batch size: {8, 16};
- Number of epochs: up to 50 (with early stopping).

The configuration used achieved the highest mIoU value on the internal folds. Outer fold tests were never observed during hyperparameter optimisation, thus preventing any loss and offering independent tests.

For training purposes, the Adam optimiser was used, with $\beta_1 = 0.9$ and $\beta_2 = 0.999$ as momentum values. The initial learning rate was determined by optimising the inner loop and was dynamically adjusted by reducing the learning rate by a factor of 0.1 when no improvement in validation loss was observed for five epochs, with the help of a Reduce-on-Plateau scheduler.

To prevent overfitting, training was stopped using an early stopping rule, which terminated training when no progress was observed for ten consecutive epochs. Training took an average of about 30 epochs.

3.1.2. Loss Functions and Class Imbalance Handling

The segmenting thermal images of PV modules presents some difficulties because background pixels are much more common than defective pixels.

To address this issue, a combined loss function was used, which combines Weighted Cross-Entropy (WCE) and Dice Loss. This combination benefits from both: the ability of Cross-Entropy to penalise pixel misclassifications and Dice overlap-based optimisation.

The Weighted Cross-Entropy part gives more importance to rare classes, such as glass damage or small hotspots, and less importance to

the common background. The class weights (w_i) were calculated using the median frequency balancing method, defined as (2).

$$w_i = \frac{median(f)}{f_i} \tag{2}$$

where f_i is the pixel frequency of class i and $median(f)$ is the median frequency across all classes. This strategy prevents the model from being biased towards the background while ensuring that small but diagnostically important regions are not overlooked. The loss of Dice directly alters the spatial overlap between the predicted mask *P* and the ground truth *G*. For each class *i*, the Dice coefficient is written as (3):

$$Dice_i = \frac{2 \cdot |P_i \cap G_i|}{|P_i| + |G_i|} = \frac{2TP_i}{2TP_i + FP_i + FN_i} \tag{3}$$

where TP_i, FP_i, and FN_i denote the number of true positives, false positives, and false negatives, respectively. The Dice Loss is then defined as 1 - $Dice_i$, averaged across all classes. This formulation is particularly effective in handling small or fragmented defects, where overlap-based metrics are more informative than pixel accuracy.

The final loss function used for training was a linear combination of the two terms (4):

$$L = \alpha \cdot L_{\mathrm{WCE}} + (1 - \alpha) \cdot L_{Dice} \tag{4}$$

with α empirically set to 0.5 to balance their contributions.

To verify the robustness of the model with large class imbalances, a study was conducted using Focal-Tversky loss. Although it wasn't included in the final training, this check provided insights into how the model reacts to changes in imbalance management.

3.2. Results

3.2.1. Evaluation Metrics Description

To correctly evaluate the suggested segmentation frame, two types of measurements were used: (i) segmentation accuracy, which controls the quality of the predicted masks, and (ii) machine performance, which measures how well the models work and whether they can be used in real-time.

Segmentation Accuracy

The predicted images are compared with truth areas to note the numbers of true positive (TP), true negative (TN), false positive (FP), and false negative (FN), for each class *i*.

These values are then used to derive the following metrics: PA (5), mean IoU (6), and macro F1-score (7).

$$PA = \frac{\sum_{i=1}^{N} TP_i}{\sum_{i=1}^{N} (TP_i + FP_i + FN_i)} \quad (5)$$

Although intuitive, PA may overestimate performance in the presence of class imbalance, as large background areas dominate the evaluation.

$$IoU_i = \frac{TP_i}{TP_i + FP_i + FN_i} \quad (6)$$

The mIoU is the average across all classes. The F1 score considers both FP and FN. This makes it a better choice than PA when checking smaller categories like hotspots or glass damage.

$$F1_i = \frac{2TP_i}{2TP_i + FP_i + FN_i} \quad (7)$$

When dealing with multiple categories, the macro F1 score is found by averaging the scores for each category without adding extra weight. This ensures that each category is seen as equally vital, regardless of how often its pixels appear. This score is helpful when the data is uneven because it shows if the model can identify small but key problem areas well.

Computational Complexity

To implement the models for their operation on drones or in edge computing, their computational cost is being evaluated.

- Number of learnable parameters (M): This is the total number of modifiable weights, in millions. It shows how much memory the model requires and how likely it is to overfit the data;
- Floating-point operations (FLOP): This is the number of calculations needed for one forward pass, in gigaflops (GFLOPs). Fewer FLOPs mean faster processing and lower energy consumption;
- Inference time per image (ms): This is the average time to process an image at a defined resolution, measured on the same hardware. It provides a realistic idea of how easy it is to use the model in real-time situations.

The accuracy of segmentation and computational complexity show which models are more precise in identifying defects and which one's better balance accuracy and speed. Monitoring both parameters is important to understand if deep learning models can be used in functioning PV monitoring systems.

3.2.2. Quantitative Results

To supervise the model training and find the best objective function for the proposed architecture, several loss functions are examined and compared (Section 3.1.2). The results (Table 10) show that the combination of Weighted Cross-Entropy + Dice Loss achieved the best overall performance, the highest mean IoU and F1-score values, and maintained stable training. The results confirm the use of the configuration as the final loss function in our Efficient Attentive U-Net.

Table 10. Metrics evaluation of the proposed model on different Loss Functions.

Loss Function	*PA (%)*	*mIoU (%)*	*F1-score (%)*
Cross-Entropy (CE)	95.76 ± 0.28	73.12 ± 0.58	83.87 ± 0.52
WCE	96.27 ± 0.26	75.41 ± 0.47	85.56 ± 0.42
Dice Loss	96.03 ± 0.37	76.25 ± 0.62	86.42 ± 0.43
WCE + Dice (proposed)	**96.88 ± 0.27**	**77.83 ± 0.43**	**87.47 ± 0.36**

The performance of the proposed Efficient Attentive U-Net is calculated by selecting a set of widely used segmentation architectures for comparison, including U-Net, U-Net++, Attention U-Net, DeepLabv3+, and SegFormer-B0. The objective is to evaluate whether the proposed model achieves a superior trade-off between segmentation accuracy and computational efficiency.

To ensure methodological consistency, all trained and validated models use the same pre-processing pipeline (Section 2.3.3) and the 5×2 nested cross-validation scheme (Section 3.1.1). Considering the structural differences between the architectures, each trained model has its own optimal hyperparameter configuration, rather than being constrained to a uniform setting. This strategy guarantees that the comparison reflects the best achievable performance of each network. The adopted configurations are reported in Table 11.

Table 11. Hyperparameters configuration for each used segmentation architectures for comparison with the proposed model.

Model	*Epochs*	*Optimizer*	*LR*	*Momentum (β_1/β_2)*	*Weight Decay*
U-Net	*50*	*Adam*	*1e−3*	*0.9 / 0.999*	*1e−4*
U-Net++	*50*	*Adam*	*5e−4*	*0.9 / 0.999*	*1e−4*
Attention U-Net	*45*	*Adam*	*5e−4*	*0.9 / 0.999*	*1e−4*
DeepLabv3+ (ResNet-50)	*60*	*SGD*	*1e−2*	*0.9 / –*	*5e−5*
SegFormer-B0	*60*	*AdamW*	*6e−5*	*0.9 / 0.999*	*1e−2*
Proposed (Eff. Att. U-Net)	*50*	*Adam*	*1e−3*	*0.9 / 0.999*	*1e−4*

The evaluation results, averaged across the outer folds of the nested CV and reported as mean ± standard deviation, are presented in Table 12.

Metrics include PA, mIoU, and macro F1-score, as well as computational indicators: number of parameters, FLOPs, and inference time per image.

Table 12. Metrics evaluation between the proposed Efficient Attentive U-Net and baseline models. Values are reported as mean ± standard deviation across the outer folds.

Model	*PA (%)*	*mIoU (%)*	*F1-score (%)*
U-Net	93.46 ± 0.40	65.12 ± 0.80	78.80 ± 0.70
U-Net++	94.92 ± 0.35	69.36 ± 0.60	81.50 ± 0.55
Attention U-Net	95.62 ± 0.30	71.12 ± 0.50	83.60 ± 0.50
DeepLabv3+ (ResNet-50)	96.26 ± 0.25	75.00 ± 0.40	85.70 ± 0.40
SegFormer-Bo	95.77 ± 0.30	73.50 ± 0.55	84.80 ± 0.45
Proposed (Eff. Att. U-Net)	**96.88 ± 0.27**	**77.83 ± 0.43**	**87.47 ± 0.36**

The results confirm that all metrics are consistently high across all model, but the proposed model demonstrates its superiority in metrics that are more sensitive to class imbalance, such as mIoU and F1. Table 13 defines the computational complexity analysis for all the evaluated models.

Table 13. Computational complexity analysis of the evaluated models.

Model	*Parameters (M)*	*FLOPs (G)*	*Training Time per Fold (s)*	*Inference Time per Image (ms)*
U-Net	31.40	46.83	972.65	748.37
U-Net++	34.78	52.14	1091.42	809.76
Attention U-Net	31.35	48.92	1015.37	669.21
DeepLabv3+ (ResNet-50)	28.57	36.41	862.84	594.18
SegFormer-Bo	**3.72**	12.64	**487.29**	241.53
Proposed (Eff. Att. U-Net)	5.24	**10.27**	603.71	**118.64**

In terms of computational cost, the proposed network remains extremely lightweight, requiring only 5.24M parameters and 10.27 GFLOPs per inference, with an average inference time of 118.64 ms per image. Compared to U-Net++ and Attention U-Net, the model reduces computational requirements by nearly an order of magnitude while still delivering better accuracy. SegFormer-Bo achieves competitive efficiency (3.72M parameters, 12.64 GFLOPs, 241.53 ms) but does not match the accuracy of the proposed model.

Therefore, carefully optimised CNN-based architectures for PV thermography can still outperform transformer-based solutions on small domain-specific datasets.

The Efficient Attentive U-Net achieves the best trade-off between accuracy and efficiency, demonstrating its potential for real-time implementation in UAV-based PV inspection and integrated monitoring platforms.

3.2.3. Per-Class Performance

While global metrics such as PA, mIoU, and F1-score provide an overall indication of performance, they may conceal important differences in how individual defect classes are segmented. We evaluated IoU and F1-score for each of the six annotated classes: background, hotspot, bypass diode fault, substring fault, soiling/shading, and glass damage. Table 14 summarises the results for the Efficient Attentive U-Net, highlighting the following considerations.

Table 14. Evaluation metrics of the proposed model for each six annotated classes.

Class	*IoU (%)*	*F1-score (%)*
Background / Normal	98.47 ± 0.23	99.18 ± 0.14
Hotspot	74.36 ± 0.95	85.27 ± 0.78
Bypass diode fault	76.82 ± 0.88	86.93 ± 0.72
Substring fault	77.45 ± 1.07	87.36 ± 0.91
Soiling/Shading	73.59 ± 1.18	84.72 ± 0.96
Glass damage	68.43 ± 1.42	81.26 ± 1.15
Macro Average	78.19 ± 0.94	87.46 ± 0.74

The background class achieved almost perfect segmentation, which was predictable given its dominance in the dataset. Among the defect categories, the best performance was observed for substring and bypass diode defects, which often manifest as extensive, high-contrast thermal patterns, making them easier to detect.

Hotspots and shading also showed relatively high IoU and F1 values, confirming the model's ability to locate small or irregular regions despite their limited pixel representation. Glass damage represented the most challenging class, achieving lower IoU and F1 values. The explanation for this can be attributed to its rarity in the dataset and the irregular and fragmented nature of its thermal signature.

The results highlight the importance of reporting metrics by class, where global indicators show the superior performance of the proposed architecture. The results by class reveal areas where improvements are still needed, especially for rare or complex anomalies like glass damage.

3.2.4. Ablation Study

The ablation study on the Efficient Attentive U-Net evaluates the contribution of each architectural component and the effect of input resolution. The analysis investigated the impact of (i) the ASPP bottleneck, (ii) AGs, (iii) SE blocks, and (iv) the input image size (224 × 224, 256 × 256, and 512 × 512), described in Table 15. All variants were trained and evaluated using the same nested 5×2 cross-validation strategy described in Section 3.1.1.

Table 15. Ablation study of the proposed architecture. Values are reported as mean ± standard deviation across outer folds.

Model Variant	*mIoU (%)*	*F1-score (%)*	*Params (M)*	*FLOPs (G)*
Baseline (U-Net with MobileNetV2)	72.46 ± 0.83	83.87 ± 0.59	4.20	8.47
+ ASPP	75.02 ± 0.71	85.64 ± 0.54	4.63	9.12
+ ASPP + Attention Gates (AG)	76.74 ± 0.66	86.79 ± 0.51	4.84	9.63
+ ASPP + AG + SE	78.11 ± 0.69	87.53 ± 0.58	5.02	10.28
+ ASPP + AG + SE @ 256 × 256 resolution	78.93 ± 0.77	88.09 ± 0.62	5.02	12.46
+ ASPP + AG + SE @ 512 × 512 resolution	79.28 ± 0.85	88.36 ± 0.67	5.02	40.37

The results, shown in Table 15, provide important information:

- Starting from the MobileNetV2 U-Net baseline, adding the ASPP module improved mIoU by +2.6 points and F1-score by +1.8, confirming the benefit of multi-scale context aggregation.
- The introduction of AGs further increased mIoU (+1.7) and F1 (+1.2), demonstrating that spatial attention effectively suppresses background noise and emphasises defective regions.
- The addition of SE blocks achieved the best performance at 224 × 224, with mIoU = 78.11% and F1 = 87.53%, while maintaining a lightweight complexity of 5.02 million parameters and 10.28 GFLOPs.
- Increasing the input size to 256 × 256 improved segmentations of small or elon-gated anomalies (mIoU +0.8, F1 +0.6 compared to 224 px) with only a modest increase in FLOPs (+25%).
- Further enlarging the input to 512 × 512 led to only a marginal gain (+0.35 mIoU, +0.27 F1 compared to 256 pixel), while more than tripling the FLOPs (from 12.46 to 40.37). This highlights that higher resolution provides diminishing returns in accuracy while severely impacting computational efficiency.

Overall, the ablation confirms that each architectural addition—ASPP, AGs, and SE blocks—contributes positively to accuracy, and that 256 × 256 pixel represents the best trade-off between performance and computational cost for UAV-based PV inspection.

3.3. Qualitative Results

In addition to quantitative metrics, qualitative examples were analysed to further assess the ability of the proposed architecture to segment different types of defects in PV modules. Representative results are reported in Figure 6, which shows side-by-side comparisons of the

original thermographic images, the corresponding ground-truth annotations, and the predicted masks produced by the Efficient Attentive U-Net.

The visual results confirm the quantitative findings and highlight several aspects of the model's behaviour. In particular, the network demonstrated high sensitivity to subtle temperature variations, accurately identifying small and intense hotspots, often only a few pixels in size, which are among the earliest indicators of soldering degradation or partial interconnection failure [102].

This behaviour aligns with recent studies showing that early-stage hotspot localization is crucial for preventive maintenance and accurate power-loss estimation in PV systems. The model accurately found small, intense hotspots, often just a few pixels in size. AGs helped reduce background noise, which allowed for precise location of these hotspots. Extended thermal patterns, like those from bypass diode and substring faults, were also accurately marked, showing clear edges and few errors.

The ASPP module was important here because it captured information at different scales, needed to spot these long defects. Similar results were reported in [103], where multi-scale context aggregation through ASPP improved the robustness of segmentation for elongated and diffuse thermal defects in industrial thermography. This confirms that multi-dilation receptive fields are essential for detecting both macro and micro anomalies under varying irradiance conditions. Even with irregular shapes and low contrast, the system could outline shaded areas, aided by SE blocks that sharpened the key features.

The SE mechanism also improved the discrimination between low-intensity shading and true hotspots, enhancing class separability and reducing false positives, consistent with observations in recent edge-guided segmentation models for PV thermograms. Glass damage was the toughest problem, but the model did a better job than basic U-Net versions at spotting broken, uneven patterns. This improvement shows the value of attention and channel recalibration methods.

To better understand how the network made its choices, Grad-CAM was used to view attention maps. Figure 8 shows examples of these maps, with brighter areas showing where the model focused when it predicted defects [104]. These views show that the model focused on areas with unusual heat and ignored background noise.

This visual evidence is coherent with interpretability analyses conducted in explainable AI models, confirming that gradient-based attention visualization provides a reliable means to validate the physical coherence of thermal-based defect detection. Such approaches improve confidence in AI-driven monitoring by ensuring that feature activation corresponds to real thermophysical phenomena rather than artefacts or background biases.

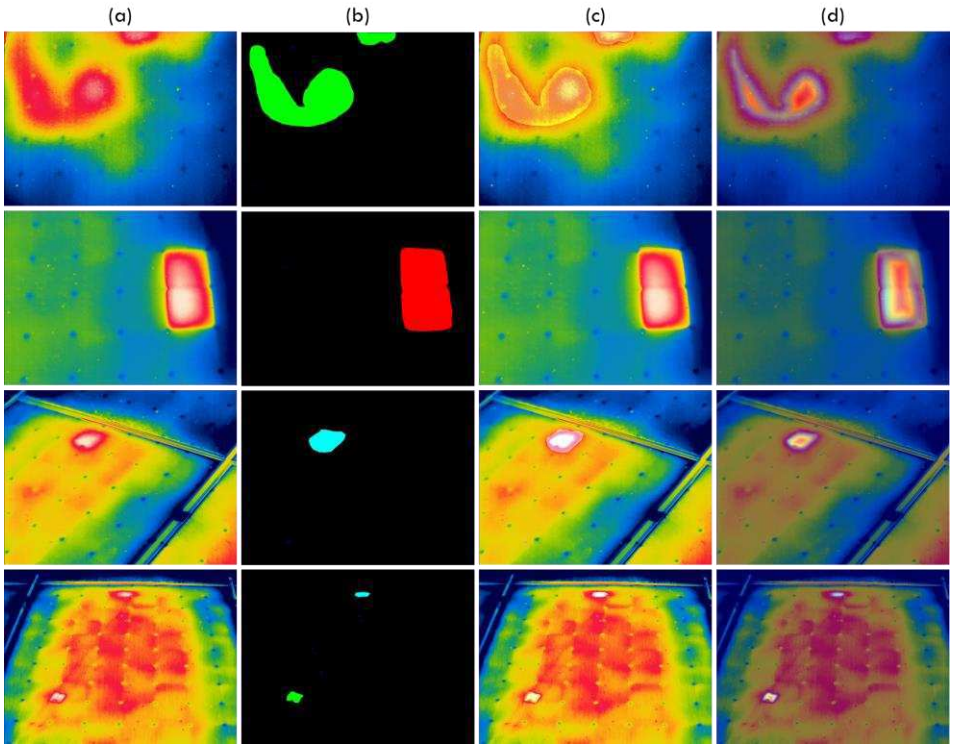

Figure 6. Qualitative results of the proposed Efficient Attentive U-Net on PV infrared imagery. Columns: (a) original thermogram, (b) ground-truth mask, (c) model prediction, and (d) Grad-CAM attention map. Rows illustrate four representative cases: (i) hotspot, (ii) bypass diode fault, (iii) soiling/shading, and (iv) glass damage. (Colour palette: background—black; hotspot—green; bypass diode fault—red; substring fault—cyan; soiling/shading—blue.)

3.4. Discussion

Detailed tests and analyses demonstrate that Efficient Attentive U-Net effectively balances image segmentation quality with processing speed. Comparing it to standard U-Net versions and more sophisticated configurations like DeepLabv3+ and SegFormer-B0, our network achieved better results in terms of average IoU and F1 scores [105]. Additionally, it maintained a relatively low number of parameters and FLOPs. This outcome confirms the central hypothesis of this study, meaning that lightweight encoder–decoder architectures, when carefully enhanced with attention and multi-scale modules, can outperform heavier designs in domain-specific tasks such as PV-IRT.

The use of AGs and SE blocks made it easier to identify small problems and damaged parts. The bottleneck in the ASPP helped identify issues with long, thin diodes. Using 256 × 256-pixel images is the best choice because they offer good quality, similar to 512 × 512-pixel images, but they don't require as much processing power from the computer. To ensure the tests were robust, a special cross-validation setup was used, so that each example was tested only once, and we tuned the settings using the training groups. By following these guidelines, the results provide a clear understanding of how it works. This approach is necessary

for PV IRT because limited-size datasets can easily lead to incorrect results if simple testing methods are used.

Nevertheless, the dataset is quite small (100 original images, increased to 400), so it might not perform as well for larger PV systems or under different weather conditions. This limitation could be reduced by fusing data from UAV thermography, satellite images, and ground sensors. Additionally, a federated learning system could be adopted to train the model collaboratively across multiple sites without requiring centralised data sharing. These strategies, already proven effective in the fields of biomedical imaging and sensory fusion, have demonstrated how data diversity significantly improves model robustness and reduces overfitting.

Moreover, some issues, such as glass damage, are still difficult to identify because they don't occur often and look different. Finally, it is necessary to implement a system that can process each image in less than 120 ms to use it in real-time on simple devices. Efficient Attentive U-Net could be incorporated into UAV inspection systems and PV monitoring configurations. The proposed system is accurate and capable of finding very small problems without requiring much computing power. In the future, with a more robust database obtained from a dataset from various sources, it would be possible to examine the combination of CNN-Transformer models and find ways to make the system even faster for specific devices.

The results obtained demonstrate that the proposed network provides a solid basis for a scalable and self-learning diagnostic system capable of supporting the continuous monitoring of large-scale PV systems.

The approach developed will be further extended in Chapter 4, dedicated to the predictive diagnostics of industrial electrical switchboards, where the methodology based on thermographic images will be integrated with LSTM temporal models for the prediction of electrical parameters.

Subsequently, in Chapter 5, this philosophy will be applied to support PdM strategies at the level of hybrid AC/DC MGs, where diagnostic information from AI-thermographic models can be implemented in O&M activities for a fuzzy-oriented EMS, capable of predictively adapting energy management according to the health status of generators and conversion devices.

4. PdM of industrial electrical switchboards using AI and IRT

This chapter introduces an integrated framework for PdM of industrial electrical switchboards, combined IRT with an electronic acquisition system based on current sensors, embedded control units and 4G LTE communication. The IRT campaign serves to identify hotspots and electronic system measures current absorption (CA) on the electrical switchboards lines. Then, a hybrid LSTM + U-Net model, called L-UN, is proposed. L-UN can correlate thermal anomalies visible in IR images with the temporal evolution of electrical signals [68].

4.1. Context and motivation

The AI-IRT diagnostic methodology described in the previous chapters, originally developed for the analysis of PV modules, has been extended and adapted to the monitoring of industrial electrical switchboards. These devices are fundamental elements in distribution systems and hybrid MG, as they concentrate elements subject to electrical and thermal wear: switches, contactors, junctions, busbars, and wiring. Defects such as loose terminals, load imbalances or harmonic currents, which can generate localised hotspots, which are often undetectable by conventional systems until they reach an advanced stage of deterioration [106].

IRT allows these anomalies to be visualised in a non-invasive manner and in real time, but the manual interpretation of thermograms is highly dependent on the operator's experience.

The integration of CNN and LSTM overcomes this limitation by automating both the spatial segmentation of defects and the temporal prediction of their thermal development.

The aim is to provide automatic predictive diagnostics that identify the symptoms of overheating at an early stage and predict their development over time, enabling proactive maintenance strategies in electrical power systems.

4.2. Data acquisition system description

4.2.1. IRT measurement campaign

The thermographic measurement campaign was conducted in a three-phase electrical panel 400 V – 50 Hz installed in an industrial environment and evaluates the point temperature variation on switchboards. The information obtained from the measurements makes

it possible to create a dataset. The thermographic analysis (Figure 7) shows that areas of excessive voltage overload can be detected, which visually results in the switchgear overheating.

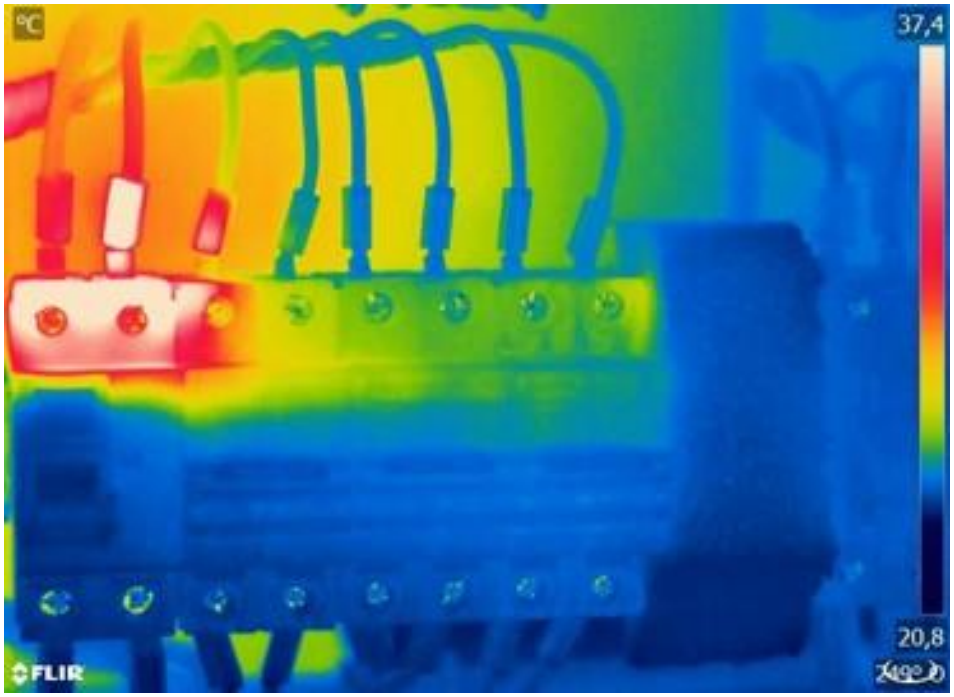

Figure 7. Switchboard infrared acquisition.

This study used an IR camera FLIR T640 with an optical sensor of 640 × 480 pixels, spectral coverage of 7.5–14 µm, and a thermal sensitivity of -30 to 30 ◦C. The distance between the IR sensor and the electrical cabinet is in the range of 0.5-2.0 meters. Errors during the measurement campaign can result from several variables in the temperature measurement equation of a typical thermal imaging camera, including emissivity, reflected ambient temperature, transmittance, atmospheric temperature, and camera response. In fact, IR cameras strongly compress the captured images, increasing the error rate. The emissivity (ε), the fraction of energy radiated by the material compared to the energy radiated by a black body placed at the same temperature, is set at 0.90 [107]. In this study, electrical equipment was classified manually using the ΔT (temperature difference) criterion [108]. The ΔT criterion is based on the temperature difference between the hot area and the reference location. The temperature exceeding that of the reference point in a malfunctioning component is known as the hot spot temperature. The reference point is the same type, load, or repeated component of the equipment with the lowest temperature. The conditions are divided into two categories according to their importance: background and hotspot. Table 16 shows these classifications, and the recommended activities associated with them.

Table 16. ΔT and actions of the component thermal state.

Thermal Condition	*ΔT (°C)*	*Priority Level*	*Recommended action*
Overheated	$\Delta T \geq 15$	I	There is a significant discrepancy that must be fixed right away.
Medium heated	$5 < \Delta T < 15$	II	If there is a possible flaw, fix it as quickly as you can.
Normal heated	$\Delta T \leq 5$	III	Overheating of a minor kind demands further study

The examination was performed with an equipment ambient temperature between 15 and 25 °C. A dataset of 1000 images was acquired at different thermal conditions, to detect hot zones (HZs) and assess the temperature variation in switch cabinets.

4.2.2. Electronic monitoring system

The electronic monitoring system was developed to enable continuous acquisition and remote transmission of electrical and thermal parameters from industrial switchboards, with the aim of enabling PdM strategies based on AI. The architecture is modular and autonomous and is based on a Central Unit (CU) equipped with Arduino and Raspberry Pi microcontrollers, responsible respectively for real-time measurement management and communication with the remote platform. The CU integrates a Wi-Fi module, a GSM/GPRS 3G/4G module with SIM card for connection to the mobile network, and a signal conditioning circuit designed to reduce measurement uncertainty and ensure the reliability of readings.

Electrical quantities are monitored using SCT-013 non-invasive current sensors, capable of detecting alternating currents up to 30 A without interrupting the circuit, generating a voltage signal proportional to the instantaneous current. The acquired data is digitised, saved locally, and processed to extract summary information, then transmitted in real time to a remote database via a 4G LTE connection. This infrastructure, detailed in Figure 8, allows for constant monitoring of consumption and the detection of abnormal variations in CA or temperature, providing a continuous flow of data for advanced analysis using soft computing and DL algorithms.

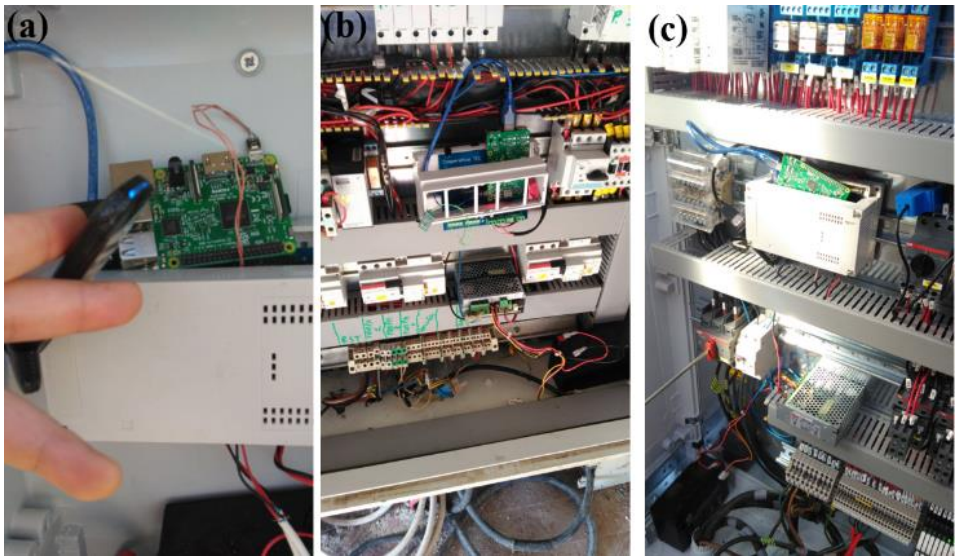

Figure 8. Integrated monitoring system: Case study: (a) Data transmission with 4G LTE Internet; (b) Monitoring system inside with CU and Raspberry in evidence; (c) Monitoring system integrated into the switchboard.

The system was tested for a period of ninety (90) days on different industrial electrical switchboards in operation, guaranteeing stable signal acquisition and the construction of a reliable thermal-electrical dataset.

The results confirmed the stability of the connection, the accuracy of the measurements and the possibility of integrating the system with predictive models based on deep neural networks. This solution therefore represents a significant step towards the digitalisation of industrial maintenance processes, with a scalable, low-cost approach that can be easily implemented in existing infrastructures.

4.3. L-UN Model

4.3.1. L-UN Description

In this study, a novel approach based on the integration of an LSTM network for the assessment of the CA data, stored by the system described in Figure 8 and of a convolutional architecture U-Net for binary mask segmentation of the switchboards IR images. The model work, called the LSTM-U-Net approach (L-UN) is presented in the following sections. L-UN model needs an initial phase of collecting CA values to produce a supervised model capable of predicting CA absorption over the following 24 hours. Subsequently, an IR image collection campaign is carried out. The collected IR images are appropriately pre-processed to allow U-Net to perform the segmentation of the thermal risk areas, while the LSTM analyses the temporal current draw data to predict possible critical situations. This synergy between temporal CA prediction and IR image segmentation makes the model extremely effective for monitoring and timely intervention in case of problems on plant. The

goal is to provide a timely emergency management system. LSTM network is an advanced RNN model designed to learn long-term time sequences [109]. The key difference between feed-forward neural networks and RNN is their ability to retain information across time steps, using the input data and an internal state. RNN model face challenges like gradient disappearance and gradient explosion. LSTM models are often used for prediction energy consumption [110].

LSTM models incorporate specialized mechanisms known as gates: the forget gate (f_t) (8), the input gate (i_t , $\tilde{c}_t$) (9, (10) the update cell state gate (c_t) (11), and the output gate (o_t) (12(13). These gates, along with an internal memory component called the cell state, allow LSTMs to regulate the flow of information and preserve long-term dependencies more effectively.

$$f_t = \sigma\big(W_f \cdot [h_{t-1}, x_t] + b_f\big) \tag{8}$$

$$i_t = \sigma(W_i \cdot [h_{t-1}, x_t] + b_i) \tag{9}$$

$$\tilde{c}_t = tanh(W_c \cdot [h_{t-1}, x_t] + b_c) \tag{10}$$

$$c_t = f_t * \ c_{t-1} + i_t * \tilde{c}_t \tag{11}$$

$$o_t = \sigma(W_o \cdot [h_{t-1}, x_t] + b_o) \tag{12}$$

$$h_t = o_t * \ \tanh\,(c_t) \tag{13}$$

Where W_f, W_i, W_c and W_o represent the input weight vectors, while b_f, b_i, b_c, b_o represent the bias vectors, and Sigmoid σ, tanh represents the activation functions. In the proposed model, LSTM is designed to learn the sequential dependencies in CA time series data. The LSTM receives 2160 CA values as input, which are normalised with a min-max scaling process, which reduces values between 0 and 1. LSTM layers captures long-term dependencies in the sequence. Dropout layers help prevent overfitting and ensure the generalization of the model. Finally, a single value output layer is produced for the next time step. LSTM model layer details are presented in Figure 9.

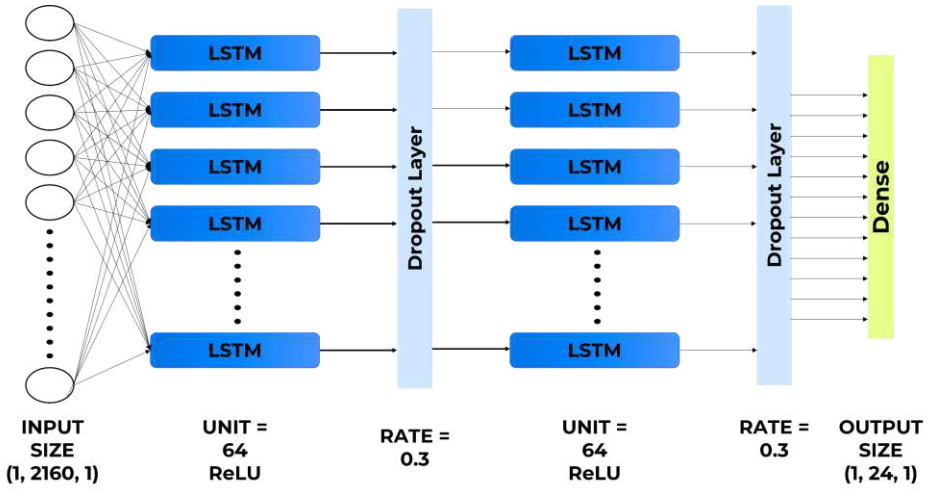

Figure 9. LSTM model architecture.

U-Net is composed of an encoder-decoder architecture. The encoding and decoding process describes the contraction path and the expansion path. The skip connection maintains the fine-grained details from the encoder and improves the segmentation accuracy by merging them with the up sampled feature maps in the decoder [111]. Original images of size 640x480 pixels are resized to 256x256 pixels. Pixel values are normalised between 0 and 1 to facilitate model training. The U-Net is designed to perform binary mask segmentation on IR images to distinguish 'medium heated' and 'overheated' areas. As presented in Figure 10, the U-Net structure begins with an input layer configured for resized grayscale images.

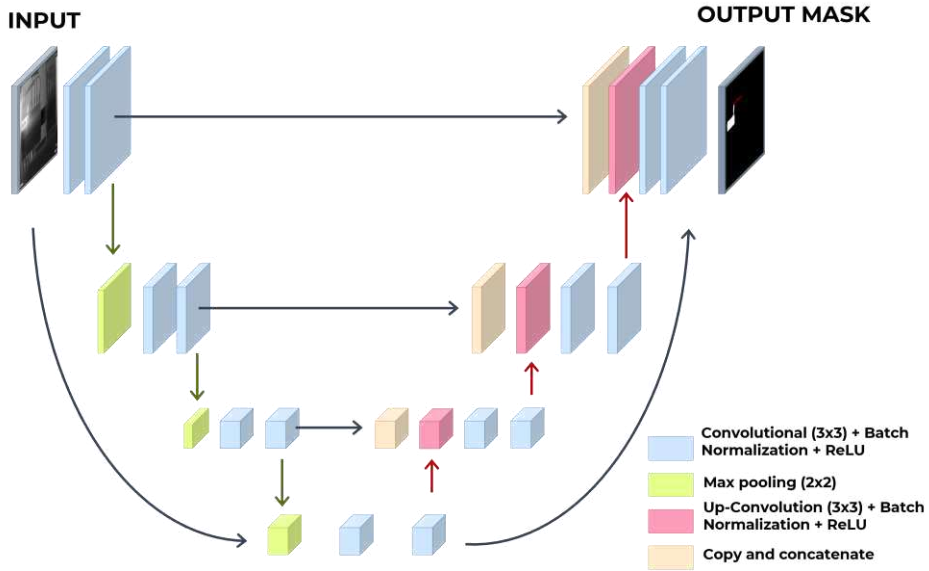

Figure 10. U-Net model architecture description.

The encoder part is composed of two sets of convolutional layers followed by two max-pooling layers. The number of convolution kernels increases progressively through the layers.

The skip connections link the encoder and decoder paths. At the centre of the network is the bottleneck layer, the bridge of the network, able to captures the high-level features of the images. The decoder part mirrors the decoder parts. The number of filters decreases progressively, and the spatial dimensions are restored. Convolutional and Up-Convolutional layers are always followed by Batch Normalization and ReLU layer. Batch Normalization (BN) stabilizes training by normalizing activations, reducing internal covariate shift, and allowing higher learning rates. ReLU introduces non-linearity, prevents the vanishing gradient problem, and improves convergence speed. Finally, the output layer is a SoftMax layer that produces the segmentation output. In Table 17 the layer details are described.

Table 17. U-Net layer details

Layer	*Output Dimensions*	*Kernel Size*	*Stride*	*Padding*
Input	(256, 256, 1)	-	-	-
Conv2D_1	(256, 256, 32)	(3, 3)	(1, 1)	same
Conv2D_2	(256, 256, 32)	(3, 3)	(1, 1)	same
maxPooling2D_1	(128, 128, 32)	(2, 2)	(2, 2)	valid
Conv2D_3	(128, 128, 64)	(3, 3)	(1, 1)	same
Conv2D_4	(128, 128, 64)	(3, 3)	(1, 1)	same
maxPooling2D_2	(64, 64, 64)	(2, 2)	(2, 2)	valid
Conv2D_Bottleneck_1	(64, 64, 128)	(3, 3)	(1, 1)	same
Conv2D_Bottleneck_2	(64, 64, 128)	(3, 3)	(1, 1)	same
Conv2DTranspose_1	(128, 128, 64)	(3, 3)	(1, 1)	same
Conv2D_5	(128, 128, 64)	(3, 3)	(1, 1)	same
Conv2D_6	(128, 128, 64)	(3, 3)	(1, 1)	same
Conv2DTranspose_2	(256, 256, 32)	(2, 2)	(2, 2)	same
Conv2D_7	(256, 256, 32)	(3, 3)	(1, 1)	same
Conv2D_8	(256, 256, 32)	(3, 3)	(1, 1)	same
Output	(256, 256, 1)	(1, 1)	(1, 1)	same

4.3.2. L-UN Logic Integration

The proposed architecture based on the integration of LSTM and U-Net networks is designed as an event-based predictive diagnostic system, rather than a continuous monitoring system.

The main objective is not the instantaneous estimation of current absorption, which is already available through direct measurements, but rather the early prediction of critical operating conditions that justify the activation of targeted thermographic inspections.

The current threshold of 30 A has not been defined arbitrarily but derives directly from the electrical dimensioning and nominal characteristics of the protection devices (industrial circuit breakers) installed in the electrical panels analysed.

This value represents the operating limit beyond which the system may be subject to significant thermal stress, increased Joule losses,

accelerated ageing of insulating materials and an increased probability of localised faults (e.g. on terminals, busbars or contacts).

Exceeding the 30 A threshold therefore constitutes an engineering risk, which makes it advisable to activate advanced diagnostic procedures, such as thermographic inspection.

The LSTM network is used for predictive purposes, and not simply to reconstruct the current signal. In particular, the model is trained to estimate whether, in the next 24 hours, there will be a time interval in which the current absorption will exceed the critical threshold of 30 A.

Let $I(t)$be the measured current and $\hat{I}(t+\tau)$the LSTM forecast over a prediction horizon t<24h. The inspection trigger is defined as (15):

$$u(t) = 1\{max_{\tau\in[0,24h]}\hat{I}(t+\tau) \geq I_{th}\}, I_{th} = 30A \quad (14)$$

where $u(t) = 1$ activates the thermographic inspection process.

The LSTM network analyses CA data per hour. If an anomaly is predicted, the system generates an alert based on the threshold of 30A. If the CA is greater than 30A, the threshold in question triggers the procedure for thermographic control. The collected IR images are processed by the U-Net to identify 'medium heated' and 'overheated' areas, if present.

The images are classified as 'normal heated' if there are no critical areas. The CA prediction process with LSTM complements the image analysis performed with U-Net to assess the action that should be made on the plant.

As shown in Figure 11, the logic workflow of the proposed model.

Table 18 resumes the operating logic of the proposed model.

Table 18. L-UN System Logic

Current Absorption predicted (LSTM)	*Class detected (U-Net)*	*Action on plant*
<30A	*///*	*No action required*
≥ 30A	*medium heated*	*Monitor closely*
≥ 30A	*overheated*	*Shut down*

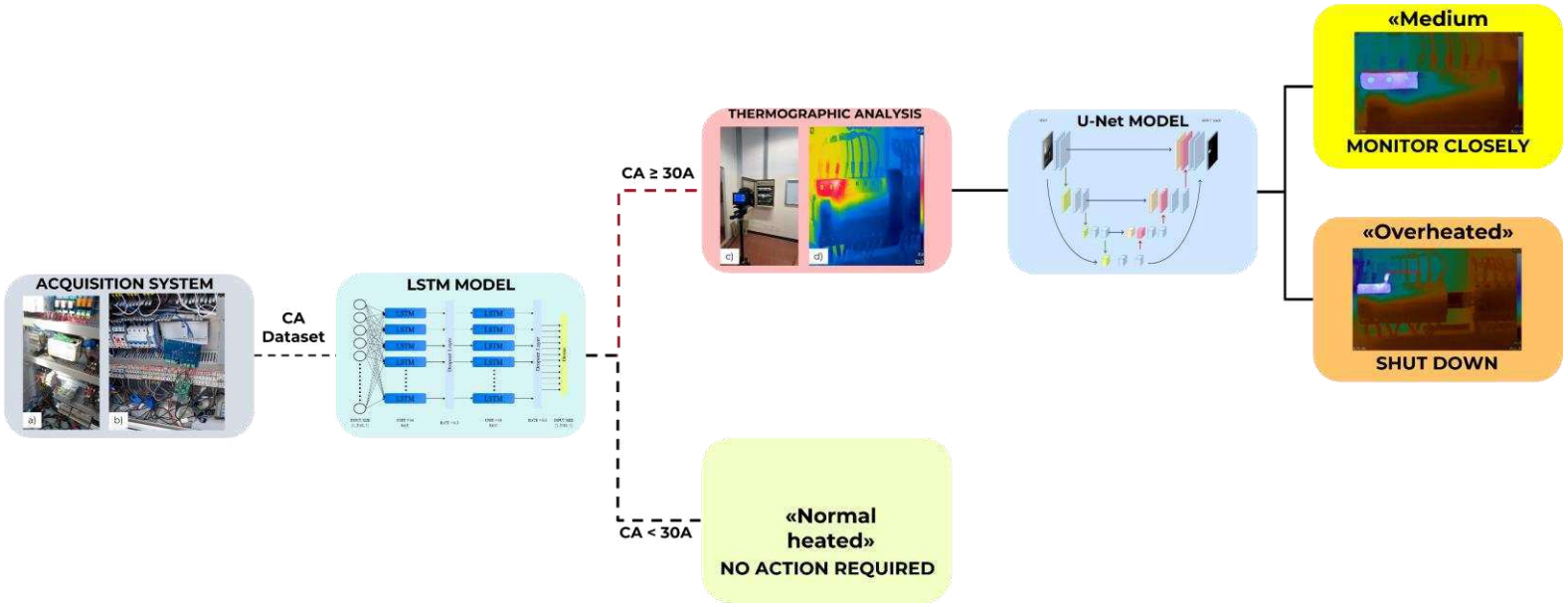

Figure 11. Logic workflow of the proposed model.

4.3.3. Operational advantages and limitations

LSTM for CA prediction

Compared to a purely reactive approach based on the observation of the measured instantaneous CA, the proposed strategy introduces a substantial conceptual change in the way IR inspection is triggered. In reactive systems, in fact, inspection is only initiated after the current threshold has been exceeded, when the electrical stress condition is already present, and the risk of degradation or failure is potentially high.

The use of the LSTM network, on the other hand, makes it possible to anticipate such conditions by predicting whether, in the next 24 hours, there will be a time interval characterised by current absorption above the critical design threshold. In this way, IR inspection can be activated before the overcurrent condition occurs, promoting more proactive risk management.

This ability to anticipate translates operationally into a reduction in emergency interventions and the implementation of a planned and predictive maintenance strategy that is more compatible with the needs of industrial contexts. IR inspection is no longer performed as an immediate response to an event that has already occurred, but as a preventive action based on the prediction of an imminent critical condition. This results in a reduction in the overall number of unnecessary inspections and an improvement in the operational efficiency of maintenance activities.

The experimental validation presented in this work focuses mainly on demonstrating the methodological feasibility and engineering consistency of the predictive approach. The limited availability of labelled industrial datasets does not currently allow for large-scale statistical validation, which is a common constraint in many real-world industrial applications. However, the proposed framework provides a solid basis for future extensions, which will include validation on a larger number of electrical panels and quantitative comparison with purely reactive triggering strategies.

U-Net for IRT heated region detection

In industrial contexts, IR analysis of electrical switchboards is often carried out using simplified approaches based on the ΔT compared to a pre-set threshold or an environmental reference. Although these methods are easy to implement, they have structural limitations that reduce their reliability and diagnostic capability in real operating scenarios.

In fact, ΔT thresholds are highly dependent on environmental and operating conditions, such as external temperature, radiation, load regime and electrical panel ventilation. As a result, the same electrical anomaly can manifest itself with different temperature increases under different conditions, making it difficult to define universal thresholds and increasing the risk of both false positives and missed detections.

Furthermore, methods based exclusively on ΔT provide information limited to the extent of the temperature increase, without allowing accurate spatial localisation of the anomaly. In the case of complex electrical panels, characterised by a high density of components such as switches, busbars and terminals, this information is often insufficient to distinguish between physiological heating phenomena and actual localised degradation conditions.

The use of a U-Net segmentation network overcomes these limitations by introducing a structured spatial analysis of the thermographic image. The network can automatically identify and segment overheated regions, preserving their shape, extent and relative position within the electrical panel. This is crucial for discriminating between widespread heating compatible with normal operation under load and localised hotspots attributable to contact defects, mechanical loosening, or material degradation.

A further advantage of the U-Net-based approach lies in the model's ability to learn complex thermal patterns that cannot be described solely by a temperature threshold. The network is able to capture spatial configurations, thermal gradients and contextual relationships between different areas of the image, allowing for a more robust assessment even in the presence of operational or environmental variations.

From an operational point of view, the adoption of U-Net integrates naturally with the LSTM-based predictive activation logic described in this chapter. Since thermographic inspection is only performed when significant electrical stress is expected, segmentation-based analysis maximises the information content of the inspection itself, avoiding redundant or poorly interpretable assessments. In this way, thermography becomes a targeted and contextualised tool within an advanced predictive maintenance strategy.

4.4. Results and Discussion

4.4.1. Dataset Description

CA Dataset

The dataset built to train the LSTM model represents the temporal data of the CA, stored on microSD memory from the electronic monitoring system. The dataset constructed to train the LSTM model represents the temporal data of the current draw (in amperes) of the industrial plant. CA values of the analysed system were collected for 90 days. Every hour, the average current is measured on a basis of six measurements collected every 10 minutes. Table 19 shows the daily CA values in terms of mean, minimum, maximum, and standard deviation for the first 10 days, in amperes.

Table 19. Brief Description of CA Dataset (A)

Day	*Mean*	*Min*	*Max*	*Std*
1	22.46	10.68	31.12	5.62
2	22.45	10.93	33.41	6.49
3	22.65	10.81	30.55	5.20
4	22.20	11.90	32.24	4.88
5	22.04	11.18	33.33	5.89
6	22.82	10.01	31.24	6.11
7	22.65	11.11	32.40	5.47
8	21.33	11.51	28.91	4.50
9	23.70	14.52	36.01	4.80
10	22.40	10.24	30.57	4.71

The LSTM model receives 2160 hourly average current consumption data as input. The goal of the LSTM model is to predict the CA values in the following 24 hours based on the patterns observed in the previous hours.

IR Dataset

The dataset of IR images on switchboards consists of 1000 images divided into classes according to the priority level of maintenance work to be carried out. IR images are divided into three classes derived from the temperature variation between the hottest and coldest points of the analysed switchboard. The priority levels, based on ΔT criterion, are defined in Table 20.

Table 20. Dataset classes based on ΔT values

Number of images	*ΔT (°C)*	*Priority Level*	*Class*
568	ΔT≤ 5	III	Normal heated
274	5<ΔT<15	II	Medium heated
158	ΔT≥ 15	I	Overheated

IR images are divided into an 80-20 working split, 80% for the training phase and 20% for the test phase. Data augmentation was performed to increase dimension by two times (2000 IR images) and robustness of the dataset. For the augmentation process random horizontal flip, random vertical flip, and random rotation [112]. Note that different classes may be present in each image. However, maintenance intervention must be based on the hottest point, so classifying the images according to this criterion ensures that decisions are made based on maximum risk. To do this, an ad hoc manual segmentation process was implemented and described in the next section.

4.4.2. Segmentation Process

For the manual segmentation process, the FLIR Tools® software was used to understand the thermal characteristics of the images. For image annotation, the open-source LabelMe tool was used. Initially, as shown in Figure 12, the thermal tuning process ensured the colour homogeneity

of all images, maintaining a consistent colour scale between 20° Celsius and 45° Celsius.

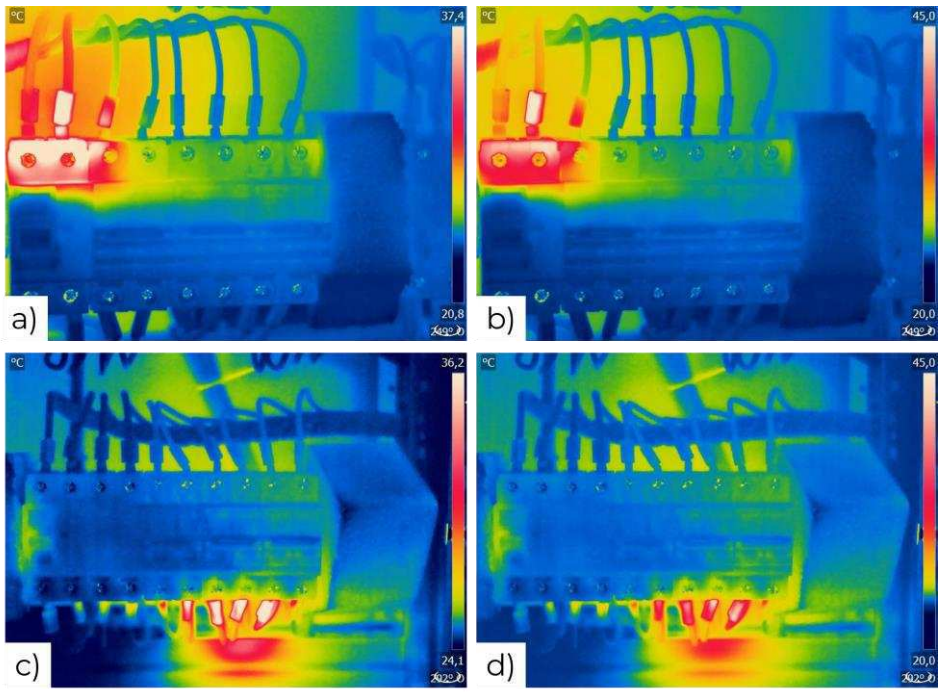

Figure 12. Thermal tuning process. a, c) medium heated and overheated images; b, d) medium heated and overheated images (thermal tuned).

As presented in Figure 13, the logic behind the manual segmentation process is based on evaluating the average temperature of the critical zones and finding the maximum temperature in the analysed images.

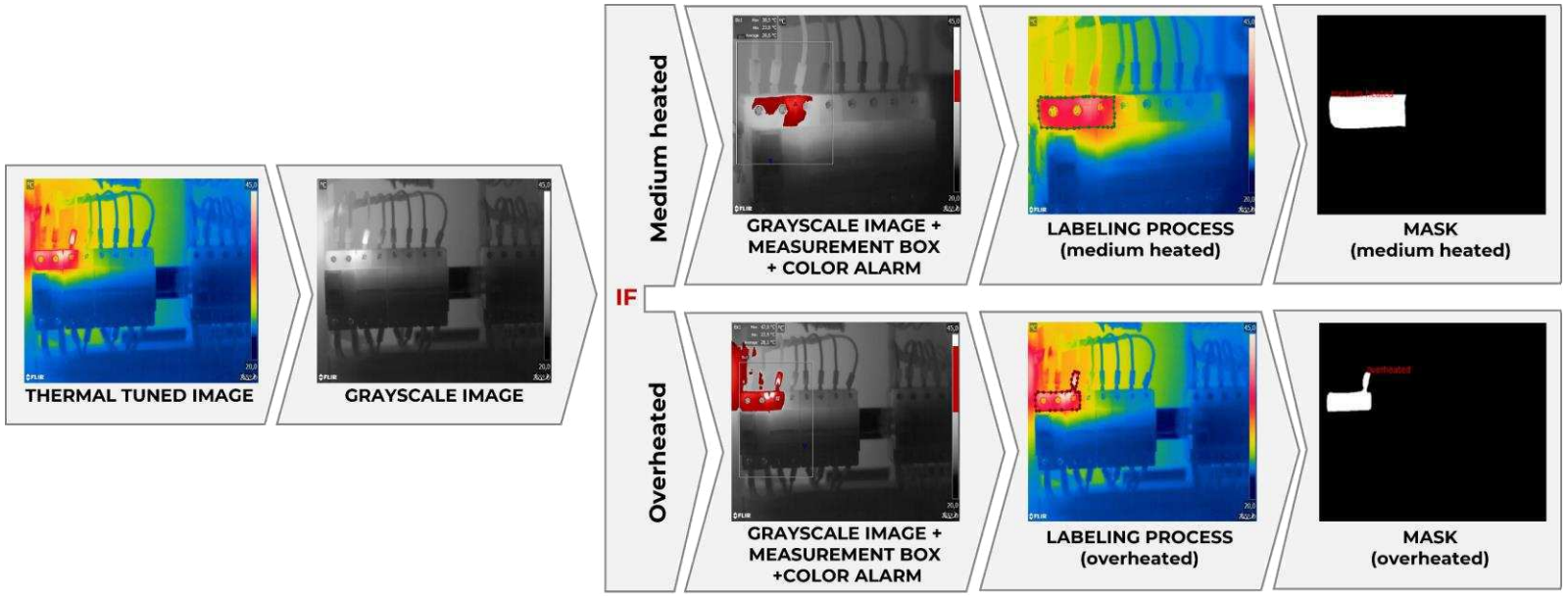

Figure 13. Logic workflow of the manual segmentation process.

The images were converted from the rainbow palette to the grayscale palette to properly identify the hottest spots, according to the ΔT criterion [63]. The FLIR Tools box and color alarm tools were used. To highlight the classes "normal heated ", 'medium heated', and 'overheated', the maximum temperature inside the box, which encloses a single switchboard, was assessed. It should be noted that for classification purposes, the only two classes considered significant for system health monitoring are 'medium heated' and 'overheated'. The aim is to create a binary mask segmentation to distinguish between these two classes in IR images.

4.4.3. Evaluation Metrics

The proposed L-UN model is evaluated through six metrics, three for LSTM model and three for U-Net model. LSTM model assessment is made with: Mean square error loss (MSE Loss) (15), mean absolute error loss (MAE) (16) and Mean Absolute Percentage Error (MAPE) (17). The reliability and accuracy of the prediction is measured by comparing the true value from the data (y_i) with the predicted value from the model ($\hat{y}_i$).

$$MSE = \frac{1}{n}\sum_{i=1}^{n}(y_i - \hat{y}_i)^2 \quad (15)$$

$$MAE = \frac{1}{n}\sum_{i=1}^{n}|y_i - \hat{y}_i| \quad (16)$$

$$MAPE = \frac{1}{n}\sum_{i=1}^{n}\left|\frac{y_i - \hat{y}_i}{y_i}\right| \quad (17)$$

U-Net model is evaluated with: Intersection over Unit (IoU) (18), pixel accuracy (PA) (19), and F1-score (20, (21). The predicted images are compared with truth areas to note the numbers of true positive (TP), true negative (TN), false positive (FP), and false negative (FN). These values are then used to derive the following metrics: IoU, PA, recall (REC), precision (PRE), and F1-score.

$$IoU = \frac{TP}{TP + FP + FN} \quad (18)$$

$$PA = \frac{TP + FN}{TP + TN + FP + FN} \quad (19)$$

$$PRE = \frac{TP}{TP + FP};\ REC = \frac{TP}{TP + FN} \quad (20)$$

$$F1 = \frac{2 \times REC \times PRE}{REC + PRE} \quad (21)$$

LSTM Performance

The LSTM model achieved a high level of precision in predicting CA over the next 24 hours of evaluation. Mean Squared Error (MSE) was used as the loss function. The train/test split was set to 80% train and 20% test, meaning the first 72 days were used for training and the subsequent 18 days for testing. Adaptive momentum estimation (Adam) was used as optimizer. LSTM model was trained for 50 epochs, the learning rate set to 10-3. As shown in Figure 14, the model performs well in generating accurate forecasts for current draw, providing reasonable forecasts for both days with CA less than 30 A and scenarios with hourly current demands greater than 30 A.

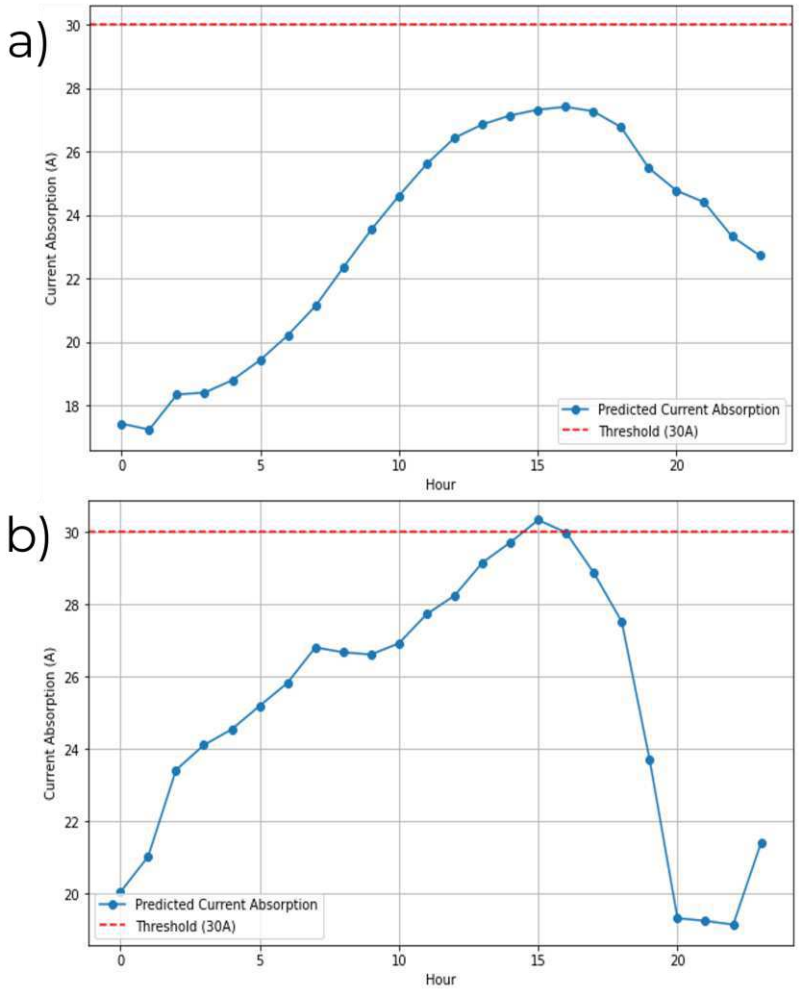

Figure 14. LSTM Current Absorption forecasting on next 24 hours. a) hourly CA under 30A (no threshold activated); b) hourly CA above 30A (threshold activated).

The model has the following performance metrics: MSE of 0.005, MAE of 0.03, and MAPE of 3.5%. This level of accuracy ensures that the model is suitable for monitoring and optimizing energy management systems.

U-Net Performance

The performance of the U-Net was assessed after a series of hyper-parameter tests. Of all of them, Adam was chosen as the network optimizer. The model was trained for 100 epochs, the learning rate set to 10^{-5}, with momentum 0.9 and weight decay 10^{-8}. The model was evaluated on several loss functions including MSE Loss, focal loss, BCE Loss and BCEWithLogits Loss. BCEWithLogits Loss was chosen for its best performance. In Table 21 the performance assessment of the proposed U-Net model was based on different loss functions and on the loss function used on the non-augmented dataset.

Table 21. Proposed Method Results - Different Loss functions

Loss	*IoU (%)*	*PA (%)*	*F1- Score (%)*
MSE Loss	60.71	98.14	38.14
Focal Loss	77.23	98.43	73.72
BCE Loss	78.48	99.14	74.12
BCEWith Logit Loss	80.12	99.72	75.42
BCEWith Logit Loss (no augmentation)	74.26	99.36	71.35

4.4.4. Implementation Details

The choice of the proposed combination of techniques is due to the ability to process the data. The ideal LSTM network for real-time applications was implemented on a Raspberry Pi using the TensorFlow framework. The choice is also motivated by the efficient inference processing capability for sequential data. Google Colab's implementation of U-Net exploits the computing resources accessible on the web. The training process was accelerated using the NVIDIA Tesla T4 GPU with 16GB of GDDR6 memory, which enabled large data sets to be handled efficiently.

4.4.5. Ablation study

To show the superiority of the integration of the techniques used, we performed an ablation study specifically focused on the predictive capacity of CA through the LSTM model. In this experiment, the U-Net classification component, associated with thermographic analysis, was excluded to quantify the effect of relying solely on electrical current prediction for shutdown decisions. It is important to notice that an ablation experiment that evaluate the thermographic measurement with U-Net classification alone would not be practically meaningful. The thermographic assessment is inherently dependent on prior indications of abnormal electrical absorption and thus cannot serve independently as a predictive measure.

CA values were collected every 10 minutes over 14 days. During this time, we deliberately increased absorption above 30A on 20 occasions, which triggered 16 shutdowns. Our proposed method reduced

unnecessary shutdowns by around 20%, significantly lowering energy use from reactivation. A simple >30A threshold was insufficient, as it often reflected transient or non-critical events unrelated to localized overheating in the switchboard. Furthermore, our investigation highlighted that CA>30A does not necessarily indicate a critical localized overheating condition symptomatic of switchboard malfunctions. As such, solely utilizing the current measurement method tends to increase false positives, leading to unnecessary interruptions in the operational process. Consequently, the thermographic component was validated as crucial in discriminating genuinely critical overheating scenarios requiring immediate shutdown (as described in Table 18). The combined approach (LSTM-U-Net) thus proves to be more reliable for targeted intervention compared to the standalone current absorption forecasting. This reinforces our assumption of integrating both components to optimize system reliability and maintenance actions.

4.4.6.Comparison Results

CA Prediction Comparison

To perform a comparison with other models and finalize the choice towards LSTM, four types of algorithms were analysed: GRU, RNN, Transformer and LSTM. All four models were trained using the same set of hyperparameters, ensuring consistency in input dimensions, network complexity, regularization, training duration, batch processing, and optimization strategy. Table 22 describes the performance evaluation for all the models.

Table 22. Performance Evaluation – CA Prediction

Model	*MSE*	*MAE*	*MAPE (%)*
RNN	*0.008*	*0.036*	*4.2*
GRU	*0.006*	*0.033*	*3.8*
Transformer	*0.007*	*0.033*	*3.9*
Proposed LSTM	*0.005*	*0.03*	*3.5*

Our proposed LSTM model was evaluated on different time windows size to assess the impact on the accuracy of prediction. We considered four different time frames (TFs) for collecting CA data points (DPs) for 90 days: 4-hours TF (540 DPs), 2-hours TF (1080 DPs), 1-hour TF (2160 DPs), 30-minutes TF (4320 DPs). Each DP was computed as the average of CA values recorded every 10 minutes over the corresponding time window. Table 23 presents the performance metrics for each time frame analysed.

Table 23. Performance on different TFs – CA Prediction

TF	*MSE*	*MAE*	*MAPE (%)*
4 hours - 540 DP	0.0092	0.056	6.1
2 hours - 1080 DP	0.0068	0.042	4.7
1 hour - 2160 DP	0.005	0.03	3.5
30 minutes - 4320 DP	0.0046	0.027	3.2

Even if the 1-hour TF is not the best in terms of accuracy, the 30-minute TF does not provide a significant accuracy gain that justifies its use for training the model. Given that the implementation is on a device like Raspberry Pi, which has limited computational power, a compromise between accuracy and computational cost was chosen.

IR Image Segmentation Comparison

To ensure a fair comparison, this study evaluate multiple U-Net architectures, including U-Net++, Attention U-Net, and U-Net_resnet34, against the Proposed U-Net. The objective is to assess whether the proposed model offers an improved balance between computational efficiency and segmentation accuracy. We tailor the arguments to each network's unique structure to achieve best performances. Table 24 presents the selected training hyperparameter.

Table 24. Training hyperparameters of each model

Model	*Epochs*	*Optimizer*	*LR*	*Momentum*	*Decay*
U-Net++	100	Adam	$1e^{-5}$	0.9	$1e^{-6}$
Attention U-Net	120	Adam	$1e^{-5}$	0.95	$1e^{-7}$
U-Net _resnet34	100	Adam	$1e^{-5}$	0.95	$1e^{-7}$
Proposed U-Net	100	Adam	$1e^{-5}$	0.9	$1e^{-8}$

The evaluation procedure examines the predicted and labelled images at the pixel level, applying the three previously introduced metrics. Table 25 provides a detailed overview of the results, where higher values signify improved segmentation performance of the model.

Table 25. Performance Evaluation – Segmentation

Model	*mIoU (%)*	*PA (%)*	*F1-Score (%)*
U-Net++	79.46	99.55	74.14
Attention U-Net	79.22	99.41	73.88
U-Net _resnet34	78.80	99.46	74.07
Proposed U-Net	80.12	99.72	75.42

4.4.7. Complexity Analysis

This section compares the models described above for CA and IR image segmentation based on key complexity parameters, including the number of leaning parameters, floating point operations per second (FLOPs), training and test time.

CA Complexity Analysis

In Table 26 the complexity parameters described shows that proposed LSTM approach. While it has more parameters and FLOPs than RNN and

GRU, it remains significantly lighter than the Transformer model while achieving comparable or superior performance.

Table 26. Computational Complexity Analysis - CA Prediction

Model	*Parameters (M)*	*FLOPs (GF)*	*Training Time (min)*
RNN	**17.48**	**2.21**	**2.83**
GRU	51.37	6.23	4.45
Transformer	238.72	19.55	15.72
Proposed LSTM	67.62	8.62	5.56

IR Image Segmentation Complexity Analysis

From Table 27, it is evident that the proposed U-Net strikes a balance between computational efficiency and segmentation accuracy. While it has higher FLOPs than U-Net _resnet34, it provides better segmentation performance, making it a feasible choice for real-time applications.

Table 27. Computational Complexity Analysis – Segmentation

Model	*Parameters (M)*	*FLOPs (GFlops)*	*Time (s)*	*Time Per Image (ms)*
U-Net++	42.26	192.84	63.06	158
Attention U-Net	36.24	244.11	82.13	206
U-Net _resnet34	**27.35**	**73.25**	**36.61**	**92**
Proposed U-Net	38.56	206.35	65.47	164

4.5. Discussion

The conducted research addresses industry and societal needs concerning energy savings and environmental protection. Industrial plants have a major impact on global electricity consumption. Soft computing technologies play a crucial role, enabling the production system to predict energy consumption.

The proposed monitoring system aims to forecasts CA from lines of industrial plants and identifies potential faults in real-time. The results demonstrate that the integration of LSTM and U-Net for monitoring electrical switchboards can lead to significant advancement in the field of predictive maintenance. This ensures both electricity consumption optimization and safety. AI, combined with a high-resolution thermal fault model from IR, is a breakthrough for switchgear fault analysis. Ongoing research challenges involve understanding 'when' and 'how' each fault occurs during field operations, even after identification. To address this, a monitoring system has been developed, controlling the real-time energy consumption of previously identified machinery. Future challenges include standardizing IR readings in the field for diagnostics and preventive maintenance strategies. Future fault detection systems for industrial machinery will be IR-based, utilizing thermography for electrical diagnostics and predictive maintenance. The overarching goal is to expedite the integration process between sensors and intelligent

algorithms, with IR and AI modelling likely encountering the described challenges.

The approach proposed for thermographic diagnosis and fault prediction in electrical panels represents a logical evolution of the PdM paradigm outlined in the previous chapters. This approach is part of a broader vision of predictive maintenance and intelligent management of complex electrical systems. The proposed LSTM-U-Net model is, in fact, a first example of multimodal integration between thermal analysis and electrical modelling, capable of connecting the domain of Condition Monitoring with that of Energy Management.

The medium- to long-term goal is to extend this philosophy beyond individual devices to a systemic vision in which AI-based diagnostics are fully integrated into intelligent energy management.

In this perspective, PdM becomes an informational function of the EMS, which can thus make decisions not only based on electrical and economic parameters, but also according to the actual operating condition of the resources. In this context, the following chapter presents the modelling of a hybrid AC/DC MG developed in MATLAB/Simulink©, in which the principles of predictive maintenance and intelligent management are integrated into a holistic O&M framework based on fuzzy logic.

5. Modelling and EMS description of a Hybrid AC/DC Microgrid

The problem of a strategy that combines ease of implementation, the ability to improve PQ, and attention to economic aspects, with a scalable and real-time-suitable architecture, therefore remains open. In this context, this chapter proposes a fuzzy-based EMS for hybrid AC/DC MG, capable of coordinating RES (PV and WT), a fuel cell unit, storage systems, and heterogeneous loads in real-time. The aim is to design and simulate a fuzzy-based EMS for a hybrid AC/DC MG, implemented in MATLAB/Simulink©. The main innovation lies in the joint integration of energy quality indices (ΔV, Δf, THD_V, TDD, and continuity) and dynamic tariff signals into the decision-making process, pursuing a balance between technical reliability and economic efficiency. Compared to other advanced EMS solutions (e.g., MPC, ANN), the proposed fuzzy controller—although composed of 80 rules—remains computationally lighter and more easily implementable on integrated hardware platforms (DSP, FPGA). Simulation results demonstrate significant improvements in electrical stability (ΔV maintained within ±2%, THD_V <3%, TDD <5%) and operating cost reduction (about 10/15% compared to a baseline EMS without PQ–tariff integration). The proposed model integrates PV, WT, and fuel cell generation units with a battery storage system, multiple AC/DC loads, and bidirectional converters. The fuzzy EMS is evaluated in terms of its ability to ensure optimal power dispatch, efficient use of storage, and enhancement of PQ indicators under variable operating conditions.

The contribution of this chapter is divided in two parts:

i. providing a comprehensive modelling framework of a hybrid AC/DC MG with RES, storage, and grid interface;
ii. demonstrating how a fuzzy-based EMS can effectively improve PQ and reliability, while reducing operational costs and support flexible energy flows.

5.1. Context and motivation

This chapter draws on experimental activities conducted at the Energy and Environment Laboratory of the DICEAM Department, University "Mediterranea" of Reggio Calabria, where a pilot plant for the production of green hydrogen powered by a PV system is implemented.

This infrastructure, described in detail in [113], represents a real-world testbed for the integrated study of RES generation, electrochemical storage, hydrogen production by electrolysis, and energy conversion using fuel cells.

Although the laboratory operates with nominal power in the order of a few kilowatts, the modular structure and functional completeness of

the system allow for the replication on a small scale of the entire energy cycle of a hybrid MG, including RES generation, electrochemical conversion, storage, and reconversion into electricity.

Based on this laboratory experiment, an extended modelling program was developed in a MATLAB/Simulink© environment, extending its scale and complexity while maintaining its logical architecture and control philosophy. This experimental setup represents the basis on which the higher-scale hybrid MG model was built.

The integration of real-world experimentation and numerical simulation is the methodological approach adopted in this thesis, aimed at extending laboratory findings to more complex grid scenarios representative of hybrid energy communities with high renewable energy penetration.

Furthermore, the modelling of the hybrid MG presented in this chapter is a logical continuation of the methodology developed in the previous chapters, in which PdM of PV systems and electrical switchboards was addressed using IRT and DL for automatic fault detection and component health assessment.

The overall objective is to build an integrated O&M platform capable of combining the physical and functional modelling of energy systems with AI-based intelligent diagnostics, creating a unified approach that encompasses prediction, control, and optimisation.

In this vision, the hybrid MG modelled in MATLAB/Simulink©, takes on the role of a digital twin of the real system: each subsystem – PV, wind, FC, battery, loads and grid – is described with physical and parametric precision, while overall management is entrusted to a fuzzy EMS, designed to coordinate energy flows, regulate exchanges with the main grid and optimise operating strategies according to load profiles, environmental conditions and dynamic tariffs.

Unlike traditional approaches based on deterministic logic or purely economic criteria, the EMS developed here is designed to integrate, in perspective, with the diagnostic information provided by AI models. In this way, dispatch and storage management strategies can be adapted in real time to the actual health status of generators and conversion devices, achieving truly predictive and adaptive energy control.

The hybrid MG thus becomes the systemic level of an extended intelligent maintenance methodology, in which thermographic and diagnostic information from AI models is integrated with Power Quality indicators (ΔV, Δf, THD_V, TDD) and the decision-making logic of the EMS.

5.2. Pilot-Scale Plant Description

The experimental plant, installed on the university campus in Via Zehender, is designed as a small-scale hybrid AC/DC MG, aimed at

validating control strategies and characterizing the performance of energy devices under real-world operating conditions.

The entire system is housed in a technical container and divided into several interconnected functional units:

- a PV section, consisting of two strings of monocrystalline modules (9 x 2 panels, total power 6.48 kWp) connected to a 6 kW hybrid inverter and a 12 kWh lithium storage system (240 V, 50 Ah x 5 modules);
- a power conditioning section, which converts and regulates the flow of energy between the PV array, the electrolyzer, and the loads;
- a hydrogen production section, based on a 2 Nm^3/h alkaline electrolyzer (AWE) (nominal power 10 kW, operating pressure 20 bar), equipped with heat exchangers, gas-liquid separators, demineralized water recirculation systems, and cooling;
- purification section, which uses a catalytic deoxidation reactor, condensers, drying unit, and storage tank (0.7 m^3, H_2 purity > 99.99%);
- reconversion section, consisting of a 1.7 kW DC PEM fuel cell and a multifunction inverter for AC power supply and charging the auxiliary battery pack (48 V, 368 Ah);
- control and monitoring section, managed via an industrial PLC, HMI interface, and sensor network dedicated to monitoring electrical, thermal, and environmental parameters.

The system can operate in three configuration modes: on-grid, stand-alone, and selective stand-alone, allowing analysis of the interaction between PV, storage, and the electrolysis process with or without grid power. The pilot-scale plant architecture in on-grid configuration is presented in Figure 15.

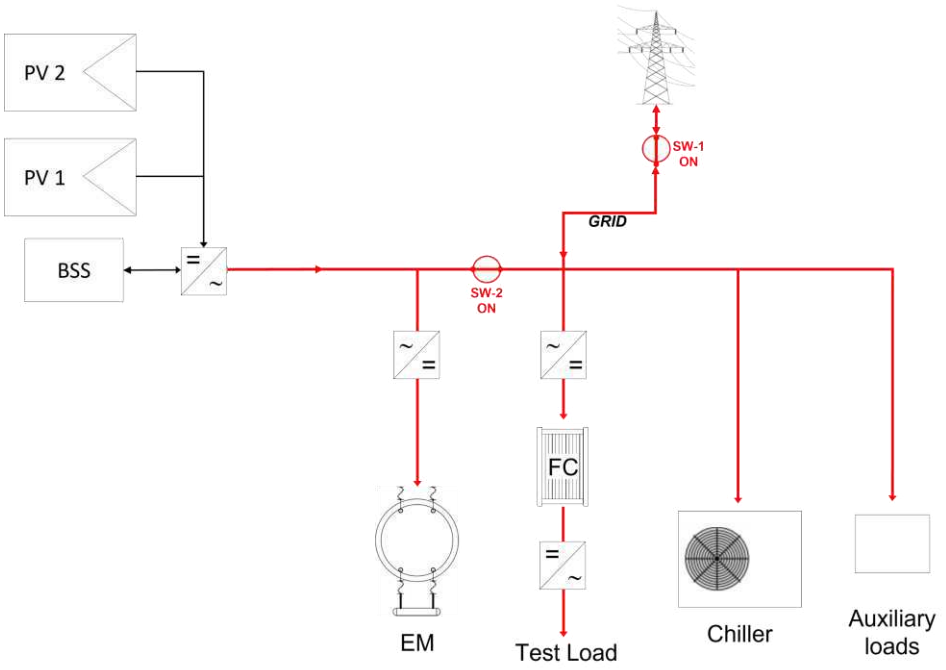

Figure 15. Pilot-scale plant architecture (on-grid configuration) [113].

The experimental tests conducted covered the entire operating cycle—from start-up and inerting mechanism to pressurization, production, and depressurization—with continuous acquisition of electrical (voltage, current, electrolyser power), thermal (internal temperature, H_2 pressure), and environmental (global irradiance, external temperature, and humidity) parameters.

The proposed hybrid MG described in next sections allows to analyse scale effects and energy interactions between the different sections, evaluating the impact of fuzzy-based EMS on voltage and frequency stability (ΔV, Δf), PQ (THD_V, TDD), overall efficiency, and operating costs.

5.3. Hybrid AC/DC MG Architecture: PV, WT, Fuel Cell, Battery, Utility Grid

The adopted hybrid AC/DC MG is designed with a 400 V, 50 Hz PCC and a 750 V DC bus, enabling the integration of multiple distributed energy resources (DERs), storage devices, and loads. Its architecture is representative of real low-voltage networks, and it is located in the city of Reggio Calabria (Italy). Figure 16 describes the structure of the adopted hybrid AC/DC MG.

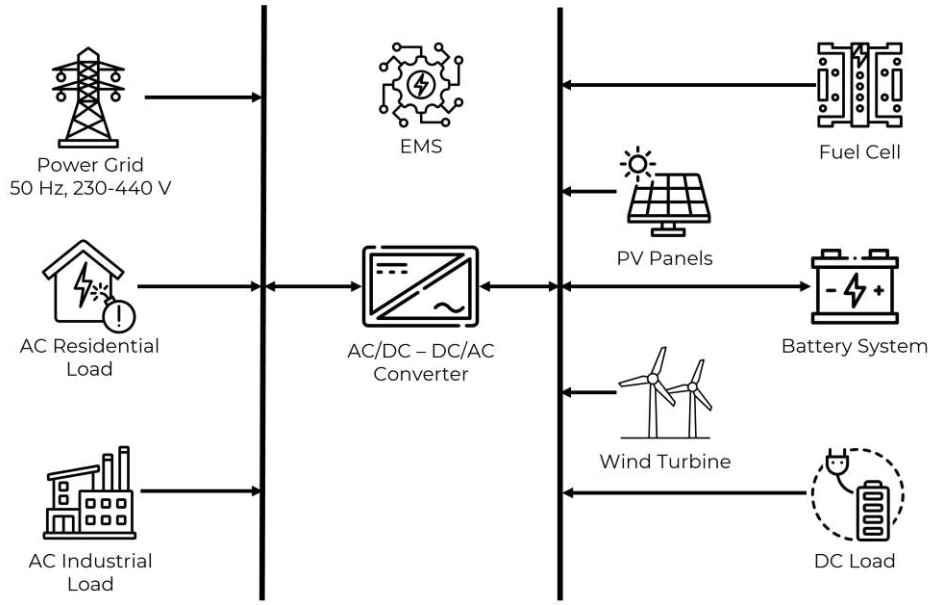

Figure 16. Schematic of the adopted hybrid AC/DC microgrid, including PV, WT, fuel cell, battery storage, AC and DC loads, bidirectional converters, and the point of common coupling (PCC) at 400 V, 50 Hz. The DC bus operates at 750 V, enabling the integration of RES and storage units.

Adopted hybrid AC/DC MG has renewable structure of a 150 kWp PV array, corresponding to approximately 270 commercial modules rated at 550 W each. This size was selected to represent a typical community PV installation in Southern Italy, with rooftop and small ground-mounted PV systems. The PV subsystem is modelled through the single-diode equivalent and regulated by a DC/DC boost converter equipped with perturb-and-observe (P&O) MPPT, which stabilizes the output voltage at the 750 V DC bus. Complementing the PV generation, a 60 kW WT is included, characterized by cut-in and rated wind speeds of 3–4 m/s and 12 m/s, respectively, and a cut-out at 25 m/s. The selected capacity is representative of medium-scale wind machines frequently adopted in hybrid community MGs. Its output is rectified through a diode bridge and further conditioned by a dedicated DC/DC converter before being injected into the DC bus. A 20-kW proton exchange membrane fuel cell (PEMFC) is integrated to support resilience during renewable scarcity. The stack operates at a nominal voltage of 48–50 V and is modelled considering activation, ohmic, and concentration losses. The size of the PEMFC was dimensioned to cover the essentials loads rather than the full demand. Its output is elevated to the DC bus level via a DC/DC boost converter, and its operation is constrained by ramp-rate and warm-up dynamics. The flexibility of the system is provided by the battery energy storage system, rated at 200 kWh of capacity and 100 kW of power. This sizing corresponds to approximately 2–3 hours of autonomy for the adopted load profile and is consistent with commercial lithium-ion storage units available at the community scale. The storage unit follows an R_{int} model with open-circuit voltage dependent on the *SOC* and is interfaced through a bidirectional buck–boost DC/DC converter. Operational limits are set within a 30–90% *SOC* window to prolong

battery lifetime, while the overall round-trip efficiency is assumed at 85–90%. The link between the AC and DC subsystems is realized by a 150 kVA bidirectional voltage source converter (VSC), which can operate in grid-following mode when the MG is connected to the utility, or in grid-forming mode during islanded operation. The converter includes an LC filter at the AC side to reduce harmonic distortion and is responsible for regulating active/reactive power exchange as well as ensuring voltage and frequency stability at the PCC. The load profile combines different demand categories representative of community-scale applications. The residential AC demand reaches a peak of approximately 50 kW during evening hours with nearly unity *PF*. The commercial/industrial AC demand peaks at 45 kW during daytime, with an average *PF* of 0.9 and reactive demand up to 15 kvar. In addition, DC loads directly connected to the 750 V bus contribute up to 15 kW of variable demand [114].

5.4. Physical Modelling in MATLAB/Simulink–Simscape Electrical

The methodology adopted in this study aims at ensuring both PQ and efficient operation in a hybrid AC/DC MG that integrates renewable and dispatchable units. The workflow is articulated in four steps: (i) definition of PQ indicators, (ii) measurement architecture and signal processing, (iii) design and implementation of the fuzzy EMS, and (iv) validation through MATLAB/Simulink© scenarios. The approach is modelled in Simscape Electrical using a physical-network approach, where each component is represented by its constitutive equations and interconnected through Kirchhoff's laws. This framework captures resistive losses, non-linearities, and transient dynamics with higher fidelity, as the solver automatically handles the underlying differential-algebraic equations (DAE). The fuzzy EMS is designed to deal with the stochastic variability of RES and loads, offering robust decision-making without relying on precise system models. Input variables (e.g., PV and wind power, AC/DC loads, battery state of charge, and dynamic tariffs) are collected via MATLAB/Simulink© functional blocks and processed in real time. All simulations were performed in MATLAB R2024b using Simulink and Simscape Electrical Toolbox on a workstation equipped with an Intel® Core™ i7-8550U processor (1.80 GHz) and 12 GB RAM. The complete model of the hybrid AC/DC MG required approximately 3 hours for setup and parameter tuning and about 35 minutes of simulation runtime for a 24-hour equivalent scenario compressed into 24 seconds of simulation time. The computational complexity of the fuzzy EMS is very low: each inference cycle (rule evaluation and defuzzification) takes about 5–10 µs per simulation step, corresponding to a ratio of approximately 1:1000 between controller processing time and electrical system dynamics, thus ensuring real-time compatibility. The selected day is representative of the entire month of June in Reggio Calabria

(Italy), chosen to avoid rainfalls or extreme weather events, thus ensuring reproducibility of the results over longer time horizons.

5.4.1. PV Subsystem

The PV array is modelled using the single-diode equivalent circuit, which captures the nonlinear I–V characteristics of a solar cell. The output current is expressed as (22) [115]:

$$I_{PV} = I_{ph} - I_0(e^{\frac{q(V_{PV} + I_{PV}R_s)}{nkT}} - 1) - \frac{V_{PV} + I_{PV}R_s}{R_{sh}} \quad (22)$$

where I_{ph} is the photocurrent proportional to irradiance, I_0 the diode reverse saturation current, R_s the series and shunt resistances, and n the diode ideality factor.

The output power is (23) [115]:

$$P_{PV}(t) = V_{PV}(t) \cdot I_{PV}(t) \quad (23)$$

To maximize energy extraction, the PV subsystem is interfaced with a DC/DC boost converter, regulated by the Perturb & Observe (P&O) Maximum Power Point Tracking (MPPT) algorithm. The duty cycle *D* is iteratively adjusted by comparing successive measurements of output power: if a perturbation in voltage leads to an increase in power, the duty cycle is further adjusted in the same direction; otherwise, it is reversed. This simple yet robust strategy allows the converter to continuously track the maximum power point (MPP) under variable irradiance and temperature conditions. The PV field is dimensioned according to standard test conditions (STC: 1000 W/m², 25 °C). Each solar cell is characterized by an open-circuit voltage of 0.5–0.6 V and a short-circuit current density of 30–40 mA/cm². Cells are connected in series and parallel to form commercial PV modules, whose parameters—open-circuit voltage, short-circuit current, temperature coefficients, and number of cells per string—are set in the Solar Cell block of Simscape Electrical. The array configuration is designed to match the DC bus requirements of the hybrid MG, providing a nominal output power in the order of several tens of kilowatts. This ensures compatibility with the battery storage subsystem and with the expected load demand of the case study. The boost converter and MPPT controller are tuned to guarantee efficient operation under dynamic irradiance and temperature profiles. The PV subsystem model implemented in MATLAB/Simulink© is described in Figure 17.

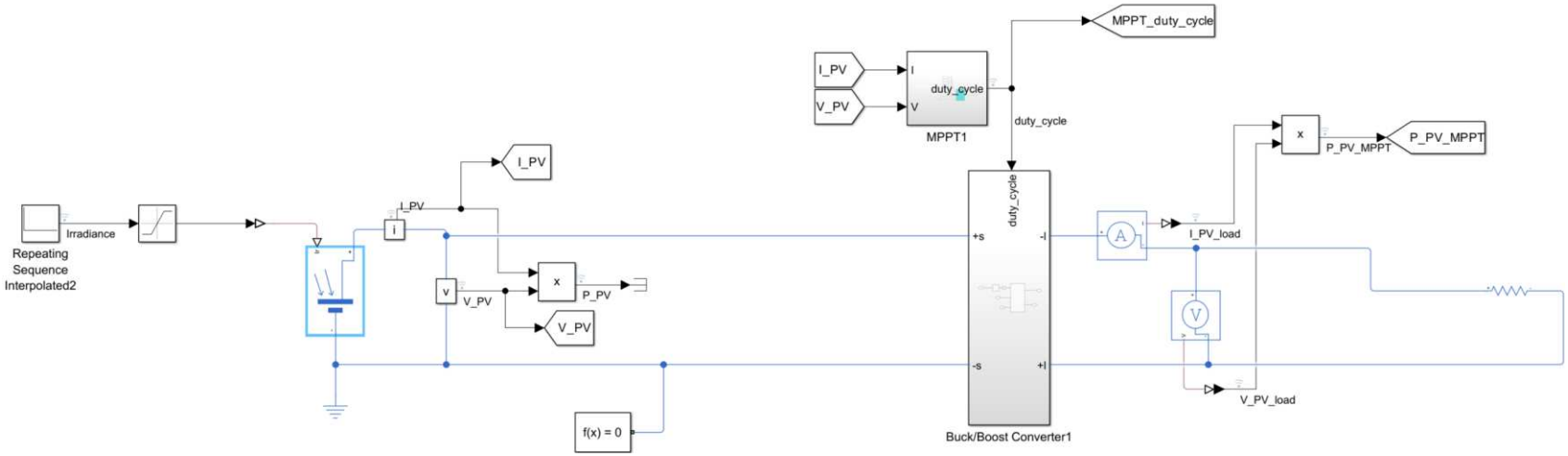

Figure 17. PV subsystem model in MATLAB/Simulink© (150 kWp, 270 modules, 550 W each). The array is represented with the single-diode model and interfaced to the 750 V DC bus via a DC/DC boost converter with P&O MPPT control.

5.4.2. WT Subsystem

The wind turbine converts wind kinetic energy into mechanical shaft power. The aerodynamic power captured by the rotor is given by (24) [116]:

$$P_{wind} = \frac{1}{2}\rho A v^3 C_P(\lambda, \beta) \tag{24}$$

Where ρ air density, A the rotor swept area, v wind speed, and C_P the power coefficient (function of tip speed ratio λ and pitch angle β).

The maximum theoretical C_P is bounded by the Betz limit ($C_{p,max} = 0.593$). The turbine exhibits the typical four operating regions: (i) start-up, overcoming inertia; (ii) cut-in speed (4 m/s), when production begins; (iii) rated power at 12 m/s, where nominal output is achieved; and (iv) cut-out speed (25 m/s), where the turbine disconnects for safety. The shaft power drives a generator modelled with its electromechanical dynamics (25) [117]:

$$J\frac{d\omega_r}{dt} = T_m - T_e - B\omega_r \tag{25}$$

with inertia J, mechanical torque T_m, electromagnetic torque T_e, and damping B.

The electrical output is rectified and interfaced to the DC bus through a DC/DC converter.

The generator's three-phase AC output is rectified through a diode bridge (Universal Bridge), producing a pulsating DC voltage. A 1 µF capacitor and a 100 Ω resistor connected at the rectifier output act as a filter to smooth voltage ripple and stabilize simulation. A downstream DC/DC converter regulates the voltage to match the DC bus level required by the MG.

The turbine, detailed in Figure 18, is dimensioned as a small-to-medium-scale system (tens of kilowatts), suitable for community-level hybrid MGs. The wind profile is provided as a daily time series (e.g., Reggio Calabria case study), ensuring realistic variability for PQ analysis.

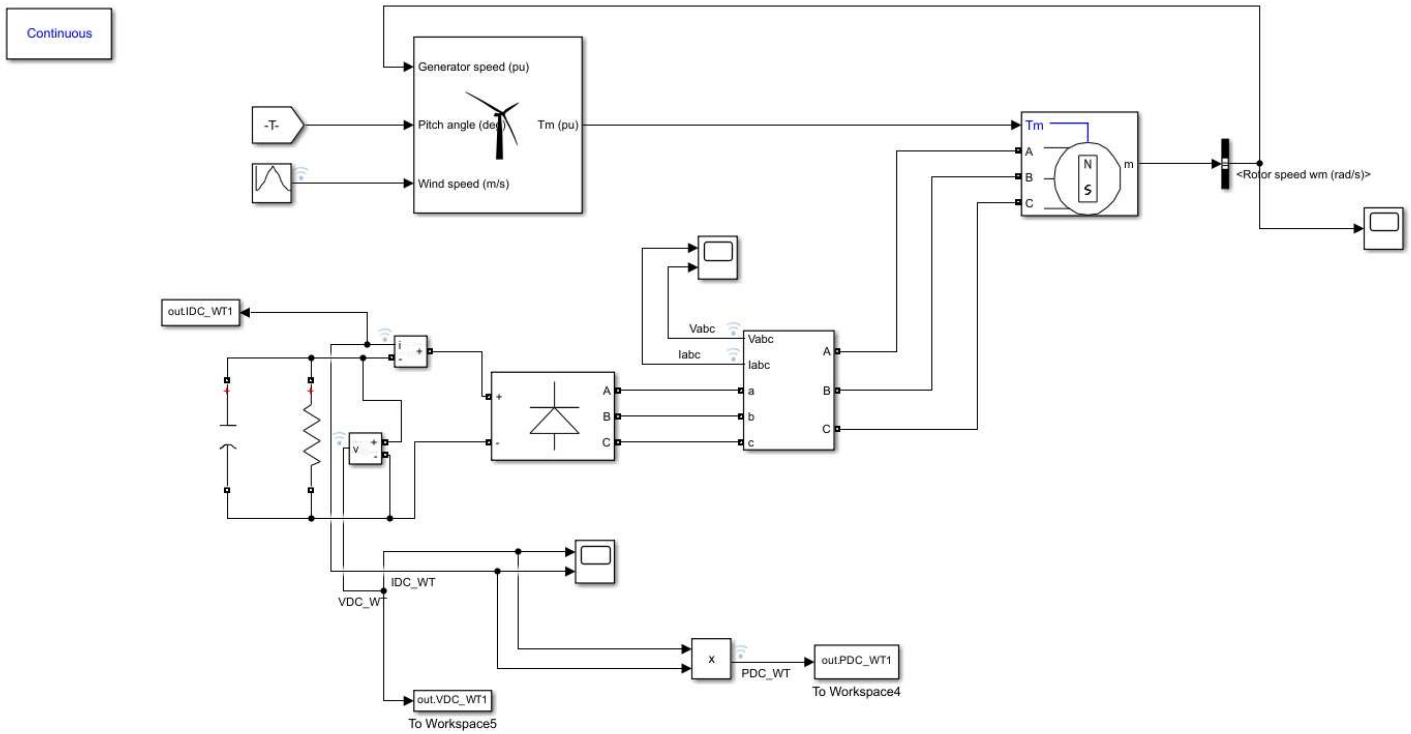

Figure 18. Wind turbine subsystem model in MATLAB/Simulink© (60 kW). The aerodynamic model with PMSM generator is rectified via a diode bridge and interfaced to the 750 V DC bus through a DC/DC converter.

5.4.3. Fuel Cell (FC) Subsystem

The fuel cell (FC) subsystem is modelled as a Proton Exchange Membrane Fuel Cell (PEMFC). The FC converts hydrogen and oxygen into electricity via redox reactions (26(28) [118]:

$$\text{Anode: } H_2 \rightarrow 2H^+ + 2e^- \tag{26}$$

$$\text{Cathode: } \frac{1}{2}O_2 + 2H^+ + 2e^- \rightarrow H_2O \tag{27}$$

$$H_2 + \frac{1}{2}O_2 \rightarrow H_2O + energy \tag{28}$$

The open-circuit voltage of a single cell is derived from the Nernst equation (29) [119]:

$$E = E^0 + \frac{RT}{2F}\ln\left(\frac{p_{H_2} \cdot p_{O_2}^{1/2}}{p_{H_2O}}\right) \tag{29}$$

Polarization losses (activation, ohmic, concentration) are included in the cell model, yielding the output voltage (30) [120]:

$$V_{FC} = N \cdot (E - V_{act} - V_{ohm} - V_{conc}) \tag{30}$$

where N is the number of cells in series.

The FC stack is configured with a nominal voltage of 50 V, achieved through series connection of elementary cells. Its rated power output is in the range of a few kilowatts, consistent with the hybrid MG's scale. Polarization curves (V–I) are used to characterize performance, identifying the safe operating region that avoids mass transport limitations. To connect to the DC bus, the FC output is regulated via a DC/DC Boost converter, modelled with an average-value approach. A PI controller adjusts the duty cycle based on the error between the DC bus reference voltage and the FC output. A small series resistance (10^{-3} Ω) is included to emulate internal resistance and stabilize simulation numeric. Operational constraints include maximum current limits, ramp-rate restrictions, and warm-up requirements to prevent degradation of the electrochemical stack.

The FC, described in Figure 19, is connected to the DC bus via a unidirectional DC/DC converter, enabling controlled dispatch.

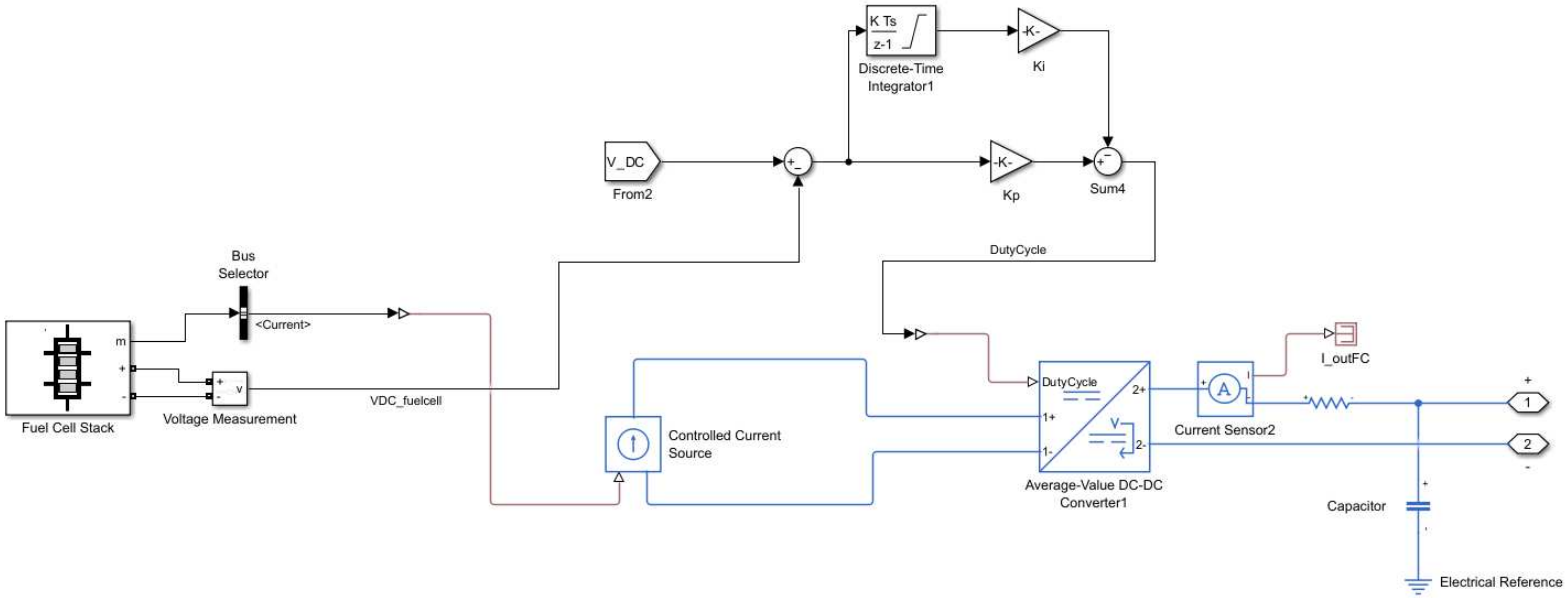

Figure 19. FC subsystem model in MATLAB/Simulink© (20 kW PEMFC). The stack output (50 V) is boosted to the 750 V DC bus via a DC/DC converter, considering activation, ohmic, and concentration losses.

5.4.4. Battery Storage Subsystem

The battery acts as a buffering element that balances generation–load mismatches and supports PQ during transients. In the model, the storage unit is parameterized from a commercial Li-ion product and interfaced to the DC bus through a bidirectional Buck/Boost DC/DC converter governed by a PI regulator; the EMS decides charge/discharge according to ΔP, SOC and tariff signals. Continuous monitoring of SOC prevents deep discharge/overcharge and guides dispatch choices between storage, grid import/export, and fuel-cell activation. The battery is represented by the R_{int} model, which includes an open-circuit VSC and an internal resistance R_0. The SOC is updated dynamically (31) [121]:

$$SOC(t) = SOC(0) - \frac{1}{Q_N}\int_0^t I_{batt}(\tau)d\tau \tag{31}$$

where Q_N is the nominal capacity.

The storage interfaces the DC bus via a bidirectional Buck/Boost stage; a PI controller regulates the duty cycle to meet the DC-bus reference while obeying converter/device ratings (current and thermal limits). This average-value implementation ensures numerically stable simulation and realistic closed-loop dynamics for charge/discharge transitions commanded by the EMS [SOC_{min}, SOC_{max}].

Within the fuzzy EMS policy, the battery absorbs surplus RES (raising SOC) and supplies deficit periods before resorting to fuel-cell activation or grid import, with the choice modulated by tariff signals. This policy is explicitly framed in the thesis discussion on tariff-aware dispatch and SOC-driven decisions. The battery storage subsystem is described in Figure 20.

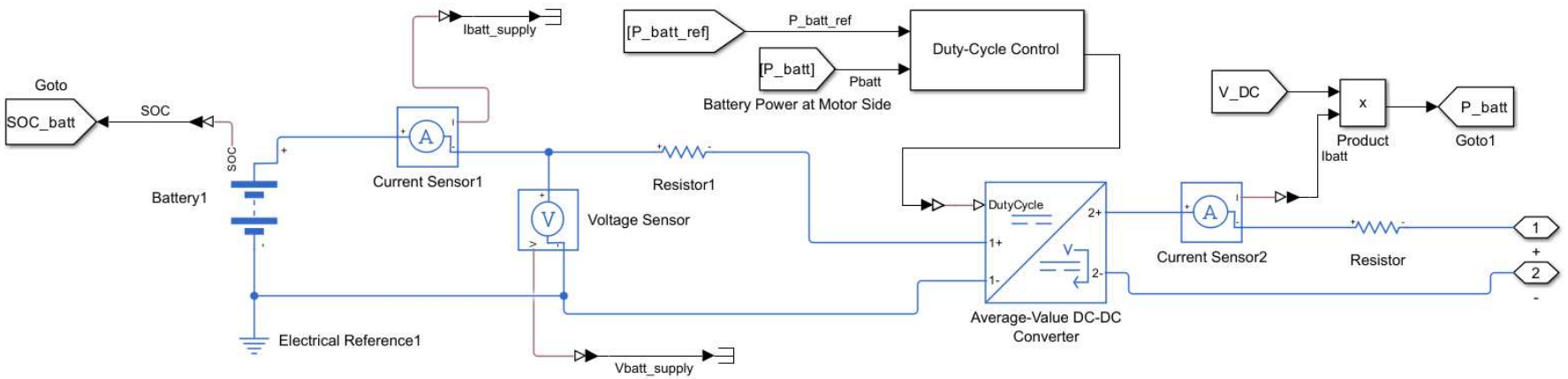

Figure 20. Battery storage subsystem in MATLAB/Simulink© (200 kWh/100 kW). The Li-ion battery, modelled with an R_{int} equivalent circuit, is interfaced to the 750 V DC bus through a bidirectional buck–boost DC/DC converter.

5.4.5. Power Electronic Converters

Power electronic converters are essential for integrating heterogeneous sources, storage units, and loads within the hybrid AC/DC MG. They provide voltage regulation, MPPT, bidirectional energy flow, and synchronization with the main grid. The PV subsystem employs a boost converter, while the battery subsystem uses a bidirectional buck–boost converter for charging/discharging. The governing equations are (32) [122]:

$$V_{out,boost} = \frac{V_{in}}{1 - D}, \quad V_{out,buck} = D \cdot V_{in} \tag{32}$$

where D is the duty cycle. Duty cycles are controlled via PWM signals generated by PI regulators.

A three-phase Voltage Source Inverter (VSI) is used to supply AC loads. Its dynamic behaviour is represented in the *dq* reference frame, enabling decoupled control of active and reactive power. A sinusoidal PWM scheme is implemented, with PI regulators adjusting modulation indices to maintain voltage and frequency stability.

This converter interconnects the AC and DC buses and provides the interface with the main utility grid. In grid-connected mode, it regulates the PCC voltage and ensures synchronization with grid frequency. In islanded mode, it switches to grid-forming control, maintaining local voltage and frequency within PQ standards. Switching logic is implemented via EMS commands, ensuring smooth transitions between operating modes.

All converters are subject to thermal and current ratings. Saturation of duty cycles (0–0.99) is applied to prevent overmodulation and protect switching devices. LC filters are included at inverter outputs to limit harmonics and ensure compliance with PQ standards.

5.4.6. Load Models

The hybrid MG supplies heterogeneous demand profiles, modelled as a combination of DC and AC loads with distinct temporal behaviours. This diversity ensures that the EMS is tested under realistic operating conditions. DC load is represented by a variable resistance connected to the DC bus, emulating typical electronic equipment and power electronics demand. The resistance varies dynamically according to a predefined profile, creating time-varying current demand directly from the DC subsystem. AC residential load is modelled as a single-phase resistive–inductive (R–L) equivalent connected to the AC bus. The daily profile peaks during evening hours, consistent with household usage patterns (lighting, appliances). The load exhibits both active and reactive components, requiring the EMS to manage *PF* and PQ indices. AC commercial/industrial load are implemented as a three-phase time-dependent impedance, combining resistive and reactive elements. The

load profile is highest during daytime working hours, with significant active and reactive power consumption. This component increases the stress on PQ indicators, especially *THD$_V$*, *TDD* and *ΔV*, when connected in parallel with renewable sources and converters. The simultaneous presence of DC, residential AC, and commercial AC loads guarantees that the EMS must coordinate multi-domain energy flows while preserving PQ. This allows robust validation of the controller under realistic MG demand conditions. Load models description is presented in Figure 21.

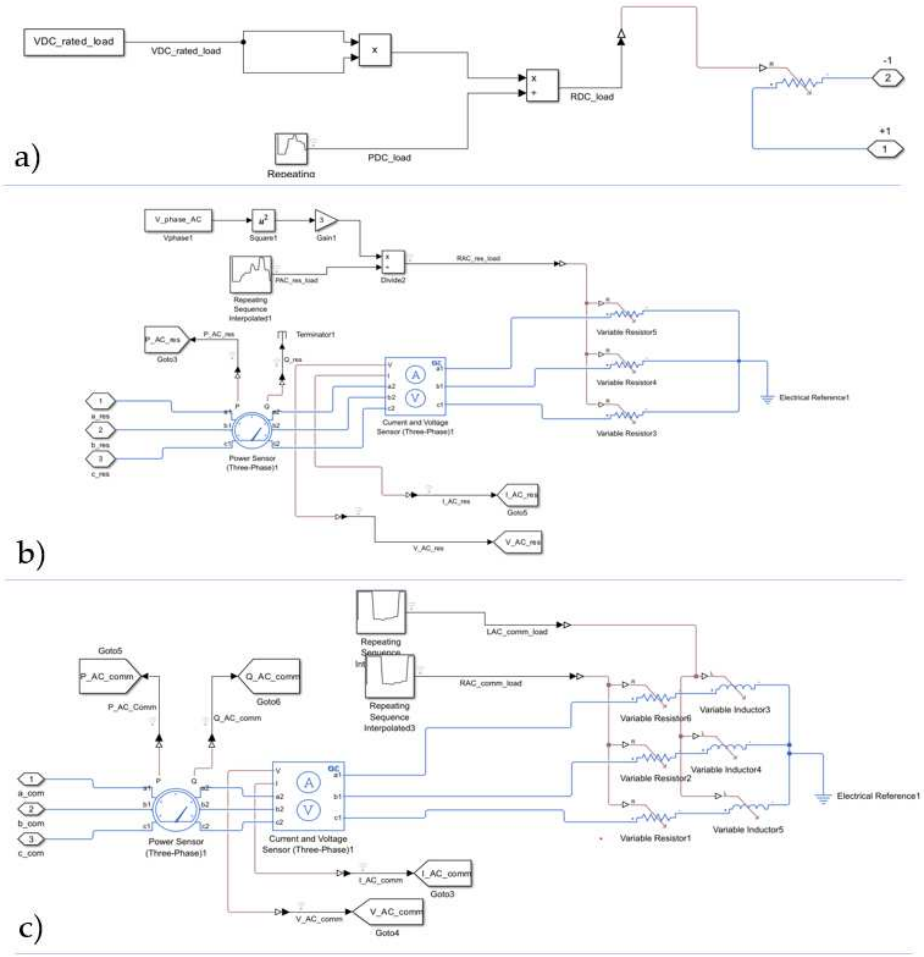

Figure 21. Load models in the hybrid microgrid in MATLAB/Simulink©: a) DC load (up to 15 kW); b) residential AC load (50 kW peak, PF ≈ 1); c) commercial/industrial AC load (45 kW peak, PF ≈ 0.9, Q up to 15 kvar).

Recently, data-driven regression approaches, such as Gaussian process regression (GPR), have also been applied to modelling complex physical behaviours. GPR shows potential of for advanced modelling activities in power supply systems by characterising the dielectric permittivity of materials with high accuracy and generalisation capabilities [123].

5.4.7. Grid Interface and PCC

The interfacing of the hybrid MG with the public grid is achieved through a PCC-located bidirectional AC/DC converter. The bidirectional AC/DC converter is mandatory to achieve a good quality of power and smooth mode transition from grid-connected and islanded modes of operations. It becomes accountable for local voltage and frequency retention at PQ standards, supplying critical loads with the aid of battery and fuel cell subsystems. Concerning PQ monitoring the CCP acts as the point of reference for PQ indices (ΔV, Δf, THD_V, TDD) measurement. In grid-connected mode, the converter operates in grid-following control, synchronising with the grid frequency and regulating the voltage PCC. The exchange of active and reactive power is regulated based on EMS commands, allowing the MG to import energy during RES deficits or export excess generation when rates are favourable. In island mode, in case of disconnection from the public grid, the inverter switches to grid-forming control. It becomes responsible for maintaining local voltage and frequency within PQ standards, powering critical loads with the support of battery and fuel cell subsystems. Regarding PQ monitoring at the PCC. The bidirectional AC/DC converter at the PCC, shown in Figure 22, illustrates the two operating modes.

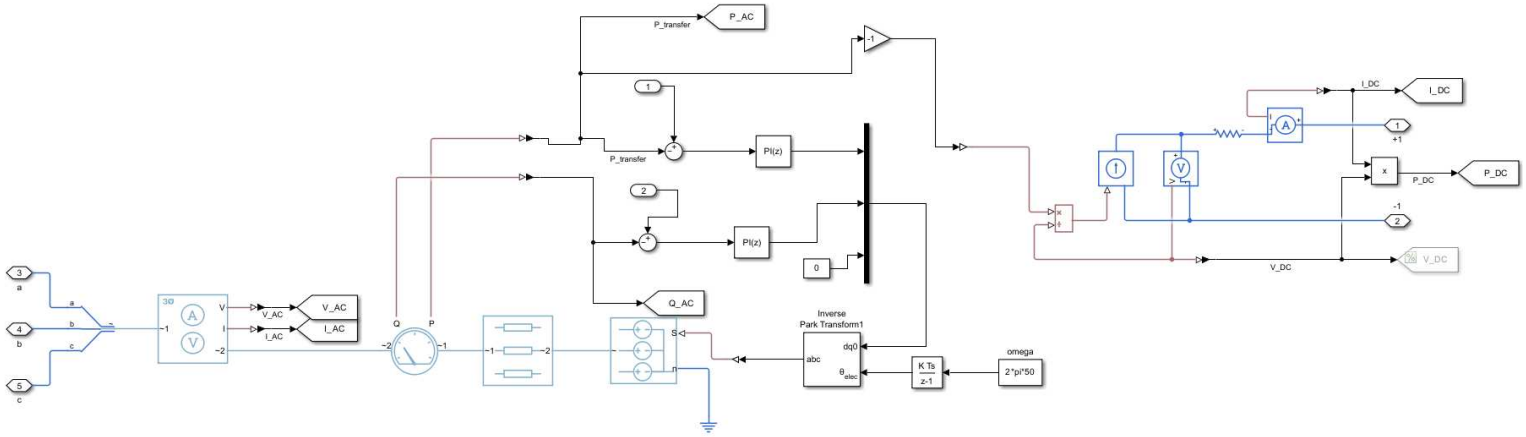

Figure 22. AC/DC inverter at PCC in MATLAB/Simulink©. A 150 kVA bidirectional VSC with LC filter connects the AC and DC buses, operating in grid-following or grid-forming mode while regulating ΔV, Δf, THDV and TDD at the PCC.

5.4.8. Summary of Microgrid Components

Table 28 summarize the principal components, models and converters used in the proposed model, including the key parameters and converter/interface description.

Table 28. Summary of components, models, and converters used in the hybrid AC/DC microgrid.

Component	*Modeling Approach*	*Key Parameters*	*Converter / Interface*
PV subsystem	Single-diode equivalent circuit	Nominal power: 150 kWp; cell Voc=0.5–0.6 V; Isc=30–40 mA/cm²; STC: 1000 W/m², 25 °C.	DC/DC Boost with MPPT (P&O)
Wind turbine	Aerodynamic model + PMSM generator	Rated power: 60 kW; cut-in: 3–4 m/s; rated: 12 m/s; cut-out: 25 m/s; Cp =0.4–0.5.	Diode rectifier + DC/DC regulator
Fuel cell	PEMFC polarization model	Stack voltage: 48–50 V; rated power: 20 kW; losses: activation, ohmic, concentration.	DC/DC Boost
Battery	R_{int} model (Voc (SOC)+Ro)	Li-ion; SOC limits: 30–90%; rated power: 200 kWh/ 100 kW; DoD ≤80%; capacity sized for daily autonomy.	Bidirectional DC/DC Buck–Boost
Converters	Average-value + PWM control	Duty cycles: 0–0.99; PI controllers; sinusoidal PWM (inverter in dq frame).	VSI (dq frame) Bidirectional AC/DC
Loads	Resistive/inductive impedances	DC load: variable resistance; residential AC: evening peak (R–L); industrial AC: daytime demand with reactive component.	Direct to DC and AC buses
Grid interface (PCC)	Bidirectional AC/DC converter	PQ monitoring: ΔV, Δf, THD_V, TDD; grid-following (connected) and grid-forming (islanding) modes.	PCC coupling with utility grid

5.5. Power Quality Indicators

PQ assessment in hybrid AC/DC MG requires a multidimensional set of indicators to ensure compliance with international standards (e.g., IEC 61000, IEEE 1159). Individual isolated indicators do not account for the interactions between conversions, loads, and accumulation. ΔV measures the deviation of the root mean square (RMS) value from the

nominal value. Voltage must remain within ±10% of the nominal reference to avoid malfunction of end-user equipment (33) [124].

$$\Delta V(t) = \frac{V_{PCC}(t) - V_{nom}}{V_{nom}} \cdot 100[\%] \quad (33)$$

In the adopted model, the reference is 230/400 V for AC and 750 V for DC, which represents a typical value for low-voltage DC MGs. This setup provides efficiency in power conversion and compatibility with commercial converters and storage systems [125]. The protection of devices requires maintaining the voltage within predetermined limits to avoid overvoltage-induced insulation stress, overheating, or malfunction of power electronics. Δf quantifies the deviation from the 50 Hz synchronous grid. According to the ENTSO-E guidelines, deviations must remain within ±0.2 Hz during normal operation [126]. Excursions exceeding the value determined by the regulations threaten stability and could trigger load detachment (34) [127].

$$\Delta f(t) = f(t) - f_{nom} \quad (34)$$

THD_V summarises the impact of harmonic components on voltage and current. Converters and switching devices introduce distortions in both voltage and current waveforms, which must remain below 5% (voltage) to comply with IEC 61000-3-2 (35) [128].

$$THD_V(\%) = \frac{\sqrt{\sum_{h=2}^{H} V_h^2}}{V_1} \cdot 100 \quad (35)$$

High values indicate converter stress and potential incompatibility with sensitive loads. While current *THD* provides an overview of waveform distortion, it may overestimate distortion impact during low current operation. For a more realistic evaluation, Total Demand Distortion (*TDD)*, defined as the ratio of harmonic current to the maximum demand current according to IEEE 519, is adopted (36).

$$TDD(\%) = \frac{\sqrt{\sum_{h=2}^{H} I_h^2}}{I_L} \cdot 100 \quad (36)$$

where I_h are the RMS harmonic currents and I_L is the maximum 15-minute RMS demand current over the simulated day.

Active/reactive power balancing is determinant for limiting apparent currents and losses and for preserving the local grid's injection capacity. Maintaining the instantaneous balance between P and Q is determinant for stability. Power factor (*PF*) deviations lead to an increase in apparent power, losses, and a reduction in the MG's hosting capacity (37).

$$P_{gen} + P_{grid} = P_{load} + P_{loss} + \frac{dE_{stor}}{dt} \quad (37)$$

Finally, short-term event continuity indices, such as voltage dips, surges, and transients, measure the system's resilience to transient events and the EMS ability to protect critical loads. The combination of

these indicators provides a comprehensive framework to evaluate both technical compliance and end-user service quality. Their thresholds, summarized in Table 29, serve as reference values for the EMS to prioritize corrective actions during simulation scenarios.

Table 29. Power Quality indicators and thresholds adopted in the hybrid AC/DC MG.

Indicator	*Definition*	*Threshold / Limit*	*Standard Reference*
ΔV	*Deviation of RMS voltage from nominal (230 V/400 V AC, 750 V DC)*	*±10% of nominal*	*IEC 61000-2-2; EN 50160*
Δf	*Difference between instantaneous and nominal frequency (50 Hz)*	*±0.2 Hz (normal), ±0.8 Hz (emergency)*	*ENTSO-E*
THD_V	*RMS of voltage harmonics over fundamental*	*≤ 5%*	*IEC 61000-3-2; IEEE 519*
TDD	*RMS of current harmonics over maximum demand current*	*≤ 5-8%*	*IEEE 519*
PF	*Ratio of active to apparent power*	*≥ 0.95 (lagging/leading)*	*IEC 61000-3-2; IEEE Std. 1459*
Active/reactive power balance	*Ability of generation/storage to supply demand with minimal reactive surplus*	*Q ≤ 5% of P (at PCC)*	*IEEE 1547*
Continuity indices (sags/swells)	*Short-term events: voltage dips (sag), temporary overvoltages (swell)*	*Sag: −10% to −90% for <1 min; Swell: +10% to +80%*	*IEEE 1159*

5.5.1. Measurement Architecture

The measurement architecture is not limited to detecting voltages and currents at strategic points in the MG but constitutes a level of observation for capturing complex phenomena [129]. The ability to integrate physical sensors with digital processing blocks in MATLAB/ Simulink© allows for the combination of experimental accuracy and modelling flexibility [130]. This aspect is important in a hybrid MG for the interactions between the AC and DC domains, because they generate transient effects that are not always describable with static parameters or RMS values. The use of the dqo transform allows three-phase quantities to be represented in a rotating reference frame, making a clear separation between active and reactive components possible [131]. In practice, this approach converts sinusoidal AC quantities into quasi-DC signals, simplifying both control and analysis. This choice is not only functional for control but also has a value that allows for a clearer study of dynamic power variations and the attribution of observed disturbances to specific operating conditions of the converters and loads [132]. In this way, measurement becomes a tool for causal analysis and not just descriptive monitoring [133]. Another important aspect concerns the temporal coherence of the signals. Synchronisation between sensors and processing units ensures high temporal resolution, which is

necessary for the correct evaluation of PQ indices, particularly *THD$_V$*, *TDD* and service continuity. The availability of high-frequency data allows for the capture of phenomena typical of power electronic systems, such as switching ripple or asymmetries in bipolar DC configurations, which would otherwise be missed by an analysis based solely on time averages. From a scientific perspective, the proposed architecture is therefore configured as a virtual laboratory where measurement is intimately linked to modelling. This not only provides input data to the fuzzy EMS but also helps validate control choices through the direct correlation between quality indices and system dynamics. The measurement layer, implemented in Simulink MATLAB©, combines physical sensors and numerical processing blocks. Each subsystem is equipped with voltage and current sensors: at the PCC, the DC bus, the PV array, the WT, the fuel cell, the battery, and the grid interface. Signals are converted into the Simulink MATLAB© domain through PS-Simulink MATLAB© Converter blocks and routed using Goto/From tags for modular reuse within the EMS. Derived quantities include instantaneous active and reactive power. The latter is obtained through the dqo transformation, which maps three-phase AC signals into a rotating reference frame, enabling decoupled control and analysis of active (*P*) and reactive (*Q*) components. In steady state, the following relations hold (38) (39):

$$P = \frac{3}{2}(v_d i_d + v_q i_q) \tag{38}$$

$$Q = \frac{3}{2}(v_q i_d - v_d i_q) \tag{39}$$

where v_d and v_q denote the dq components of the three-phase voltages obtained through the park transformation, and i_d and i_q are the corresponding dq components of the three-phase currents. The Park transformation is adopted because it converts sinusoidal three-phase quantities into DC-like variables in a rotating reference frame, thus simplifying the control and analysis of AC systems [134]. In this framework, the d-axis represents the direct component aligned with the rotating reference frame, while the q-axis is the quadrature component orthogonal to it. Their cross-multiplication allows a decoupled and instantaneous calculation of active and reactive power.

5.6. Design and Logic of the EMS

The EMS supervises the hybrid AC/DC MG by coordinating PV and WT, storage (battery), dispatchable generation (fuel cell), and grid exchange. Its objectives are: (i) maximizing renewable self-consumption, (ii) respecting technical and operational constraints, (iii) improving PQ indices, and (iv) minimizing operating costs under dynamic tariffs. While conventional centralized or rule-based strategies often lack flexibility and robustness, fuzzy logic control provides an adaptive, non-linear, and uncertainty-resilient framework. This paradigm is particularly suited to

MG where renewable variability, stochastic loads, and market signals cannot be precisely modelled. Inputs to the fuzzy controller include the net power imbalance between generation and demand, the battery *SOC*, and the hourly electricity tariff. Based on these, the EMS generates four key outputs: (i) reference power for the battery converter (positive for discharge, negative for charge), (ii) reference power for the AC side via the bidirectional AC/DC converter, (iii) grid connection/disconnection command, and (iv) fuel cell activation signal. The EMS structure, implemented in MATLAB/Simulink©, integrates functional blocks such as summation nodes for ΔP, normalization gains, multiplexers/demultiplexers, and switches with thresholds to convert continuous outputs into binary logic for grid and fuel cell control. The core is the Fuzzy Logic Controller block, designed in the Fuzzy Logic Designer app and exported as *a .fis* file into the Simulink workspace. Through this design, the EMS, described in Figure 23, ensures that surplus renewable energy is either stored or injected into the grid depending on *SOC* and tariff conditions, while deficits are covered by the battery, the fuel cell, or the grid according to cost-effectiveness and PQ constraints.

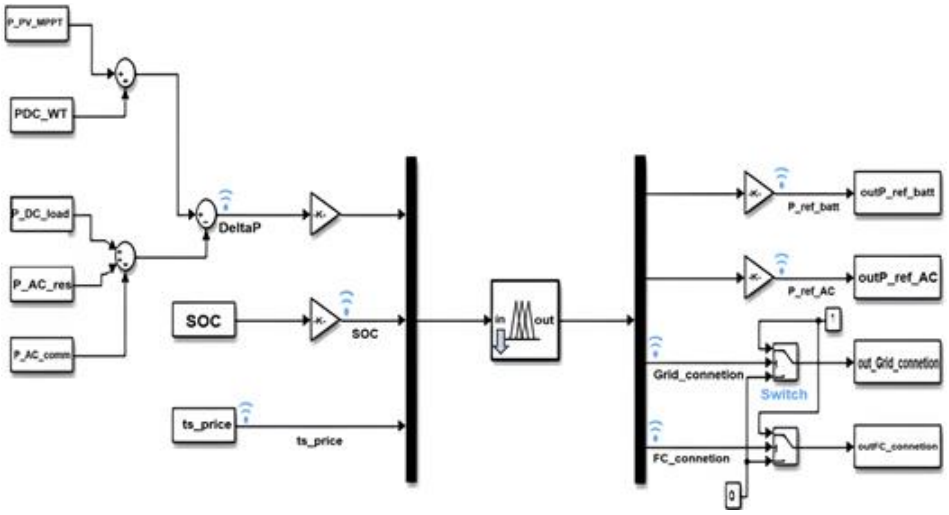

Figure 23. Fuzzy EMS architecture implemented in MATLAB/Simulink. The system processes input variables including PV power, WT power, AC/DC load demand, SOC, and dynamic tariff signals.

The structure comprises fuzzification, a rule base (80 fuzzy rules), inference, and defuzzification stages. Outputs are the battery power reference, AC-side dispatch reference, and connection commands for the main grid and FC.

5.6.1. Fuzzy Controller Structure

The EMS controller is implemented as a Mamdani-type fuzzy inference system (FIS) [135], designed in MATLAB's Fuzzy Logic Designer and exported into Simulink MATLAB©. This choice allows non-linear

decision making based on heuristic rules, suitable for uncertain and time-varying MG conditions. The model considers three input variables: ΔP, *SOC* and the energy time-of-use signal (TOU). Each of these quantities is characterised by fuzzy sets defined through triangular membership functions, which allow for the translation of numerical values into qualitative descriptions. The ΔP is implemented within the range [-150; +150] kW, which corresponds to the maximum expected imbalance between total generation (PV, WT, FC) and the load profile in the adopted MG. The ΔP is classified as negative, zero, or positive. The *SOC* variable has been considered within the range [30; 90] %, reflecting the safe operating limits of the battery subsystem: the lower threshold at 30% prevents deep discharge and premature degradation of the battery, while the upper limit is set at 90%. The *SOC* is divided into increasing levels: low, medium, high, and very high. The electricity tariff, considered within the range [0.05; 0.15] €/kWh, reflecting the variability of dynamic prices typically observed in the Italian electricity market. The electricity tariff is distinguished into low, medium, and high price bands. The controller outputs, on the other hand, concern four fundamental decisions: the reference power for the bidirectional battery converter (Pref_batt), the reference power for the AC/DC interface (Pref_AC), the connection status to the main grid, and the activation of the fuel cell (FC_connection). In this case as well, the membership functions are defined to ensure gradualness and computational simplicity. The Pref_batt (−100 to +100 kW) can take on charging, discharging, or idle values. The Pref_AC (from 0 to 150 kW) is modulated across three power levels. The network connection and fuel cell activation are managed as Boolean variables (0–1), derived from the fuzzy process using activation thresholds. The choice of binary values is motivated by the discrete nature of these operations, which in practice correspond to either activating or deactivating the respective device. In this way, the entire decision space of the MG is represented by a coherent set of linguistic rules that connect operating conditions to control actions. The system design strikes a balance between model accuracy and computational lightness, allowing the controller to operate in real-time and react flexibly to unexpected situations. The fuzzy inference engine is implemented as a Mamdani-type system, where rules are evaluated using max–min composition [136], and outputs are defuzzified through the centroid method [137]. This approach, validated in the literature, produces smooth and continuous control signals, particularly effective for variables such as Pref_batt and Pref_AC. In addition to the fuzzy logic, the controller enforces component-level protections. For the battery, *SOC* is constrained within 10–100%, and a maximum C-rate of ±5 kW is imposed to limit charge/discharge stress through the bidirectional DC/DC converter. Internal resistance and thermal effects are modelled in Simscape using variable parameters, ensuring realistic dynamic behaviour. For the fuel cell, operational constraints include ramp-rate limits and warm-up times before connection to the DC bus, which

prevent degradation of the electrochemical stack and auxiliary subsystems. For the converters, both DC/DC and AC/DC stages are subject to current and thermal limits defined by device ratings; duty cycles are internally saturated within [0–0.99] to protect switching devices, while PI controllers regulate duty cycles under these constraints to guarantee stable operation. At the PCC, PQ thresholds are imposed in compliance with international standards: voltage deviation ΔV within ±10% of nominal, frequency deviation Δf within ±0.2 Hz, and THD_V limits of 5% and *TDD* limits of 8%. Whenever these limits are exceeded, corrective EMS actions such as grid reconnection or selective load shedding are triggered to preserve stability.

This integrated design ensures that the fuzzy EMS captures both the flexibility of heuristic decision-making and the robustness of hardware protection, achieving a balance between model accuracy, computational lightness, and operational reliability.

5.6.2. Fuzzy Controller Design

The fuzzy controller is developed to map uncertain and time-varying inputs into robust and adaptive control actions for the hybrid MG. Its design consists of three main steps: definition of membership functions, construction of the rule base, and specification of the inference/defuzzification process. Table 30 summarize the fuzzy EMS inputs, outputs, and membership functions.

Table 30. Summary of fuzzy EMS inputs, outputs, and membership functions.

Variable	*Type*	*Range*	*Membership Functions (MFs)*	*Notes*
ΔP	Input	[-150, +150] kW	Negative, Zero, Positive (triangular)	Net difference between generation and demand
SOC	Input	[10, 100] %	Low, Medium, High, Very High (triangular)	Expressed as % of rated battery capacity
Tariff (Electricity price)	Input	[0.05, 0.15] €/kWh	Low, Medium, High (triangular)	Hourly dynamic tariff signal
P_{ref_batt}	Output	[−100, +100] kW	Charge, Idle, Discharge (triangular)	Reference for bidirectional DC/DC battery converter
P_{ref_AC}	Output	[0, 150] kW	Low, Medium, High (triangular)	Reference for AC/DC converter exchange
Grid_connection	Output	{0,1} (binary)	Disconnected, Connected	Boolean control obtained via thresholding
FC_connection	Output	{0,1} (binary)	OFF, ON	Boolean control for fuel cell activation

The fuzzy decision-making process relies on a knowledge base of if–then rules that encode expert reasoning and operational priorities [138]. Approximately 80 rules cover the full range of system conditions, balancing energy autonomy, cost-effectiveness, and PQ enhancement.

Illustrative examples include:

- Surplus management: IF SOC = High AND ΔP = Surplus AND Tariff = High THEN export to grid.
- Deficit management: IF SOC = Low AND ΔP = Deficit THEN activate fuel cell.
- Tariff-aware charging: IF Tariff = Low AND ΔP = Surplus THEN charge battery.
- Tariff-aware import: IF Tariff = High AND ΔP = Balanced THEN avoid import.
- Emergency condition: IF SOC = Very Low AND ΔP = Deficit THEN connect to grid AND activate fuel cell.

The complete rule base defines all possible combinations of *ΔP*, *SOC*, and Tariff states with corresponding outputs for the battery, AC interface, grid connection, and fuel cell. Table 31 presents representative subset of the fuzzy rule base for the EMS.

Table 31. Representative subset of the fuzzy rule base for the EMS, showing the mapping of ΔP, SOC, and tariff conditions into control actions for the battery, AC interface, grid, and fuel cell.

ΔP (Power imbalance)	*SOC (Battery)*	*Tariff (€/kWh)*	P_{ref_batt}	P_{ref_AC}	*Grid connection*	*FC connection*
Surplus-High	High	High	Discharge	High	Connected	OFF
Surplus-Low	Medium	Low	Charge	Low	Disconnected	OFF
Balanced	Medium	High	Idle	Medium	Disconnected	OFF
Deficit-Low	Low	Medium	Discharge	Medium	Connected	OFF
Deficit-High	Low	High	Discharge	High	Connected	ON
Deficit-High	Very-Low	Any	Idle	Low	Connected	ON
Surplus-High	Very-High	Low	Charge	High	Connected	OFF

5.7. Validation Scenarios

To assess the robustness of the EMS and the hybrid MG model, five representative simulation scenarios were defined exploring different operating conditions, stressing both technical and economic objectives:

i. Normal operation with high-RES availability: PV and WT supply most of the demand, while the battery operates in charge/discharge mode to smooth fluctuations. The EMS prioritizes self-consumption and limits grid interaction.

ii. Islanding with critical loads: Upon disconnection from the main grid, the EMS ensures continuity for critical AC/DC loads. The battery and fuel cell provide backup, while non-critical loads may be shed to preserve stability.
iii. Step load variations: Sudden increases and decreases in load are applied to test the EMS response and PQ stability. Indicators such as ΔV, Δf, THD_V and *TDD* are monitored to evaluate transient resilience.
iv. Low- RES availability: When renewable production is insufficient and *SOC* approaches its lower threshold, the EMS activates the fuel cell and imports power from the grid to maintain supply.
v. Dynamic tariff fluctuations: Time-varying electricity prices are introduced to verify the EMS ability to shift charging/discharging decisions. The controller minimizes costs by charging during low-price hours and exporting or avoiding import during high-price periods.

These scenarios were selected as they represent the most critical and recurrent operating conditions of a hybrid AC/DC MG. They cover nominal operation, emergency islanding, fast load transients, renewable scarcity, and tariff variability, thus enabling validation of both the technical robustness (scenarios 1–4) and the economic effectiveness (scenario 5) of the proposed fuzzy EMS.

5.8. Evaluation Criteria

The performance is assessed according to a set of complementary criteria, combining technical, economic, and robustness perspectives.

- PQ indices: ΔV, Δf, THD_V and *TDD* are continuously monitored at the PCC. These parameters were selected because they represent the fundamental indicators of PQ as defined by IEC 61000, IEEE 1159, IEEE 519 and ENTSO-E guidelines. The international IEC/IEEE standards set the thresholds of ±10% ΔV, ±0.2 Hz Δf, 5% THD_V and 5/8% *TDD* serve as a benchmark for PQ stability.
- Event statistics: disturbance events, such as sags, swells, and interruptions, are recorded through dedicated counters. The frequency and duration of such events provide insight into the resilience of the EMS under transient operating conditions. Continuity indices quantify the EMS capability to preserve supply quality during short-term disturbances, a critical aspect for sensitive loads and for demonstrating compliance with IEEE 1159 recommendations.
- Energy balance: the EMS is assessed in terms of import/export exchanges with the grid, renewable self-consumption ratio, and battery cycling. This metrics were chosen because they

highlight how effectively the controller maximizes local use of RES and optimises storage utilization.

- Economic cost/benefit estimation: by considering dynamic tariffs, the EMS is tested for its ability to reduce operating costs. Metrics include cumulative energy cost, avoided purchases during high-price periods, and revenues from energy export during peak tariffs.
- Robustness analysis: system performance is assessed under parameter variations, such as changes in load demand, renewable generation profiles, and component ratings. Robustness is confirmed when PQ indices and economic benefits remain within acceptable limits despite uncertainties.

Together, these criteria provide a holistic evaluation of the EMS, demonstrating its capability to maintain technical compliance, enhance economic efficiency, and ensure reliable operation under diverse and uncertain MG scenarios.

5.8.1. Computational Complexity

The computational burden of the proposed fuzzy EMS is minimal compared to the intrinsic dynamics of the hybrid AC/DC MG. Rule evaluation and defuzzification require 5–10 μs per simulation step. The dominant electrical dynamics of converters and network transients evolve on the order of milliseconds (10^{-3}–10^{-2} s).

The resulting ratio of about 1:100–1:1000 confirms that the controller introduces negligible latency relative to system dynamics. Even when combined with PQ calculators (FFT-based THD_V and *TDD* estimation, event counters, RMS monitors), the supervisory layer remains computationally lightweight. The most demanding operation, FFT-based harmonic analysis, is only applied to selected signals and over limited time windows, further reducing processing overhead.

This low complexity makes the controller suitable for real-time or embedded deployment. Platforms such as digital signal processors (DSPs), field-programmable gate arrays (FPGAs), or *SOC* devices can easily host the fuzzy EMS together with PQ monitoring modules. As a result, the methodology is compatible with practical hardware-in-the-loop testing and field implementation in smart MG controllers.

5.9. Limitations and Assumptions

Despite its effectiveness, the proposed EMS is subject to several limitations and simplifying assumptions that should be acknowledged:

- Simplified component models: The battery and fuel cell are represented with reduced-order electrochemical and thermal dynamics. While sufficient for control validation, these models do not capture degradation mechanisms or detailed thermal behaviour, which could influence long-term performance.

- Tariff signal as exogenous input: The electricity price profile is treated as an externally provided input. No forecasting or market participation mechanisms are included, and the EMS assumes perfect knowledge of tariff variations.
- Indirect PQ improvement: The EMS improves PQ primarily through dispatch decisions (balancing power, managing *SOC*, activating the fuel cell). Advanced reactive power control or harmonic compensation is not implemented, leaving PQ enhancement partly indirect.
- No advanced observers: *SOC*, THD_V, *TDD* and PQ indicators are computed using direct measurements and robust filtering, without the use of observers (e.g., Kalman filters or neural estimators). While this avoids complexity, it may limit accuracy under sensor noise or faults.

Table 32 describes the impact on the results of the limitations and assumptions made in this study.

Table 32. Impact of modelling assumptions and limitations on quantitative results.

Limitation	*With limitation (this study)*	*Without limitation (expected)*
Simplified battery & FC models	*SOC* 30–90%; H_2 –14%	*SOC* 25–85%; H_2 –10%
Tariff as perfect input	Cost reduction ≈12%	Cost reduction 8–10%
Indirect PQ improvement	ΔV ±2%; THD_V <3%; *TDD* <5%	ΔV ±1%; THD_V ≈2%; *TDD* ≈3%
No advanced observers	PQ indices ±2% accuracy; Δf ±0.2 Hz	PQ indices ±1% accuracy; Δf ±0.1 Hz

These limitations define opportunities for future work, including integration of detailed electrochemical/thermal models, incorporation of predictive market strategies, deployment of advanced PQ controllers, and use of intelligent observers for enhanced state estimation.

5.9.1. Justification for model-based rather than experimental validation

The validation of the proposed hybrid AC/DC MG was performed through physical-network modelling in MATLAB/Simulink rather than experimental testing. This methodological choice stems from both technical and practical considerations. The system integrates heterogeneous distributed energy resources at community scale (150 kWp PV, 60 kW wind turbine, 200 kWh battery, 20 kW fuel cell, and 150 kVA bidirectional converters), whose full-scale experimental implementation would require high-power infrastructures, dedicated safety systems, and substantial investment beyond the available laboratory facilities. Furthermore, the primary goal of this work is to assess the effectiveness of the fuzzy-based Energy Management System (EMS) in coordinating distributed resources and improving power quality

and economic performance under realistic operating conditions. These objectives can be reliably achieved through physical-network simulation, which allows a high-fidelity representation of converter dynamics, transient phenomena, and PQ indicators (ΔV, Δf, THD_V, TDD) in a fully controllable and repeatable environment compliant with IEC/IEEE guidelines.

Finally, the present model validation is conceived as an intermediate stage toward experimental deployment, paving the way for future Hardware-in-the-Loop (HIL) and real testbed implementation, as outlined in the future work. Therefore, the use of model-based testing should not be viewed as a methodological limitation, but as a necessary step to ensure reproducibility, safety, and scalability toward real-world applications.

5.9.2. Experimental Verifiability of Performance Indicators

The performance indicators adopted in this study, ΔV, Δf, THD_V, TDD, PF, and continuity indices, are not limited to numerical evaluation. All these quantities can be directly measured and verified in a real hybrid AC/DC MG using standard power quality instrumentation and high-resolution data acquisition systems compliant with IEC 61000, IEEE 519, IEEE 1159, and EN 50160 standards.

In practical terms, the measurement architecture implemented in the MATLAB/Simulink model can be reproduced in an experimental setup by installing synchronized voltage and current transducers at key points such as the PCC, the DC bus, the converters, and the grid interface. When combined with high-sampling-rate data acquisition units (sampling rate ≥10 kHz), this configuration enables real-time computation of RMS quantities, harmonic spectra (THD_V and TDD), ΔV and Δf, as well as short-term continuity events (sags, swells, and transients) through standardized event counters and time windows. The same formulations and threshold criteria used in simulation can therefore be directly applied to experimental data, ensuring consistent comparison between modeled and measured results.

For the DC domain, voltage, and current measurements, including ripple and converter-related transients, can be performed using Hall-effect transducers and differential probes, while derived indices such as TDD on branch currents can be obtained through FFT or DFT-based spectral analysis. The corresponding limit values and computational methods remain aligned with the technical standards adopted in this study. The experimental validation of the proposed fuzzy EMS and its associated performance indicators can be carried out in both hardware-in-the-loop (HIL) environments and pilot-scale MG testbeds, maintaining identical measurement points, sampling frequencies, signal processing procedures, and compliance thresholds. This approach guarantees reproducibility of the results and traceability of the system performance

with respect to the technical and economic objectives demonstrated in the simulation study.

5.10. Simulation Setup

The adopted hybrid AC/DC MG was implemented in MATLAB R2024b – Simulink/Simscape Electrical©. Simulations were run over a 24-hour horizon, compressed into 24 seconds of simulation time, allowing detailed observation of fast transients and slow energy dynamics within a manageable computational effort. Parameters like solar irradiance, wind speed, load, and tariff profiles derived from realistic daily conditions in Reggio Calabria (Italy).

5.10.1. Solver configurations

Each subsystem was assigned a dedicated solver for numerical stability:

- The WT, modelled in Simscape Electrical – Specialized Power Systems, used Powergui Continuous mode to capture electromechanical dynamics accurately.
- The fuel cell (FC) required Powergui Discrete mode with a fixed step of 5×10^{-5} s, ensuring proper resolution of switching dynamics in the DC/DC converter.
- Other subsystems (PV, battery, converters, loads) were simulated with adaptive stiff solvers handling DAEs across the global model.

5.10.2. Environmental and load profiles

- Solar irradiance: daily profile of June in Reggio Calabria, with a peak around 1000 W/m² at midday.
- Wind speed: empirical hourly profile, cut-in at 3–4 m/s, rated at 12 m/s, cut-out at 25 m/s, with afternoon peaks up to 12–14 m/s.
- Loads: total demand representative of 12 residential households and 2 commercial/industrial users, with evening peaks for residential and daytime peaks for commercial/industrial loads.
- Tariffs: dynamic pricing ranging between 0.05 and 0.15 €/kWh, influencing EMS cost-driven decisions.

5.10.3. Simulation Stability and Load Variation Management

To ensure numerical and dynamic stability under variable load and current conditions, several simulation measures were adopted. Each power electronic converter was equipped with current and thermal protection limits (duty cycle saturation between 0 and 0.99, rated

current constraints, and LC filters) to prevent oscillations and overcurrent phenomena. PI controllers were tuned to achieve critically damped responses for both voltage and current loops, avoiding overshoot during step load variations. The fuzzy EMS Scope actively compensated for power imbalances by modulating the reference powers of the battery converter and the AC/DC interlinking converter, effectively smoothing transient currents and maintaining power quality indices (ΔV, Δf, THD_V, TDD) within IEC/IEEE standard limits. Step-load and islanding tests were explicitly simulated to validate the controller's robustness: the DC bus voltage remained within ±2% of nominal, and converter currents settled within 50 ms after each disturbance. Solver configurations (Powergui Continuous for the wind turbine and Discrete with a 5×10^{-5} s step for the fuel cell) ensured numerical stability and convergence during high-frequency switching events. These combined control and numerical strategies effectively prevented current instability and mitigated the impact of abrupt load variations throughout the 24-hour simulation cycle.

5.10.4. Data management

Selective signal logging was enabled to reduce computational load, focusing on voltages, currents, instantaneous powers, duty cycles, *SOC*, and PQ indices (ΔV, Δf, THD_V, TDD). Outputs were post-processed using Simulink Data Inspector and stored in the MATLAB Workspace for EMS decision-making.

Case Studies

Two case studies were defined:

- Case A (baseline): MG operated without fuzzy EMS, relying only on local converter controls.
- Case B (proposed): MG managed by the fuzzy EMS, coordinating RES, storage, FC, and grid interface.

This setup provides the basis for comparing PQ performance, energy balance, and economic efficiency under realistic daily operating conditions.

5.11. Subsystems Profiles

5.11.1. RES Generation

The hybrid MG integrates two renewable subsystems—PV and WT—with complementary production patterns. Their combined contribution ensures a diversified portfolio of generation, reducing dependence on a single resource and enhancing overall stability.

PV subsystem

The PV array output is governed by solar irradiance, which follows a deterministic daily profile. In the considered June day in Reggio Calabria,

irradiance peaks at 1000 W/m² around noon, resulting in a maximum PV power of ~150 kW (Figure 24a). Production begins at sunrise, ramps up steadily until midday, and then decreases toward evening. This smooth and predictable curve ensures that PV dominates the generation mix during daylight hours. The MPPT P&O algorithm successfully tracks the maximum power point across all conditions, as evidenced by the converter duty cycle trajectory (Figure 24c). The MPPT efficiency remains high throughout the day, allowing the PV subsystem to operate close to its theoretical maximum.

WT subsystem

Unlike PV, wind generation is inherently stochastic and less predictable. The WT subsystem is driven by hourly wind profiles, with speeds fluctuating between 3–14 m/s. The turbine reaches cut-in at ~3–4 m/s in the morning, operates near its rated region (~12 m/s) during the afternoon, and shuts down if exceeding 25 m/s. On the analysed day, average wind power results in a production with peaks of ~60 kW in the early afternoon (Figure 24b). Variability is more pronounced than for PV, with transient dips and surges that directly affect the DC bus. The rectifier–DC/DC stage modulates its duty cycle (Figure 24d) to stabilize the DC link, compensating for rapid fluctuations in aerodynamic power.

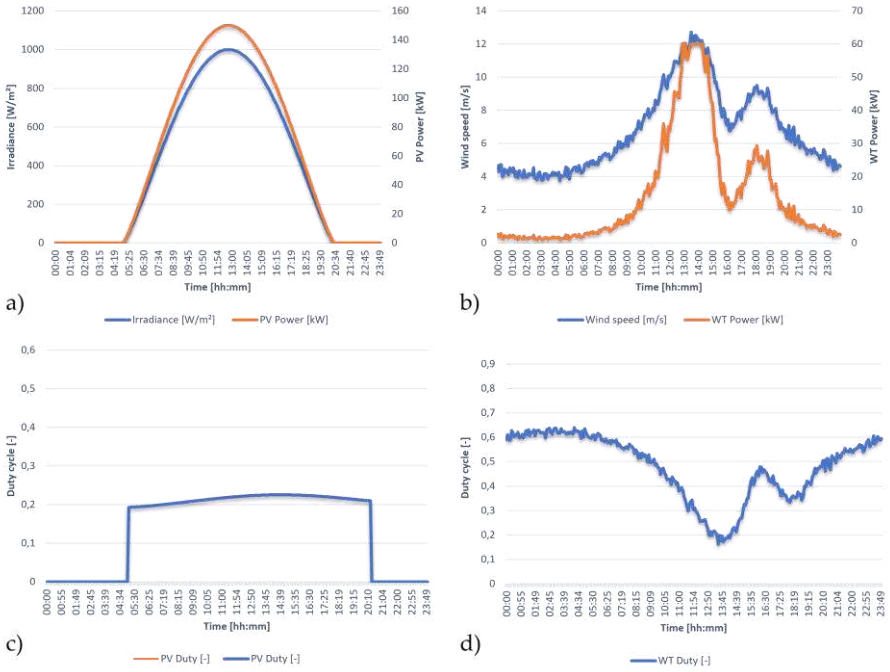

Figure 24. Renewable generation profiles in MATLAB/Simulink© over a 24-hour horizon, compressed into 24 seconds of simulation time, derived from realistic daily conditions in Reggio Calabria, Italy: (a) solar irradiance and PV power, (b) wind speed and WT power, (c) PV duty cycle, (d) WT duty cycle.

5.11.2. Loads

The hybrid MG demand is modelled as the superposition of DC, residential AC, and commercial AC loads, each characterized by distinct daily patterns (Figure 25).

- DC load: Represents electronic and ICT equipment, such as LED lighting and server racks. It exhibits a variable demand with peaks of ~15 kW, supplied at a nominal voltage of 48 V. The equivalent resistance dynamically changes according to the power profile, ensuring realistic representation in Simscape.
- Residential AC load: Aggregated from 12 households, modelled with *PF* = 1. The profile shows two pronounced peaks: a midday peak of ~40 kW (11:00–14:00) and an evening peak of ~50 kW (19:00–22:00), consistent with typical household activity patterns. The remainder of the day is characterized by moderate consumption in the 10–20 kW range.
- Commercial AC load: Represents 2 small/medium enterprises, modelled with *PF* = 0.9. Demand is concentrated during business hours (08:00–18:00), with an average active power of ~35 kW and peaks up to 45 kW. The reactive power demand reaches ~15 kVar, stressing PQ indices and testing EMS capability in reactive power balance.

The coexistence of DC, residential, and commercial loads generate complementary demand curves, with residential peaks aligning partially with PV production, while commercial loads overlap with business hours. This heterogeneity ensures that the EMS must coordinate resource dispatch across different domains and time horizons.

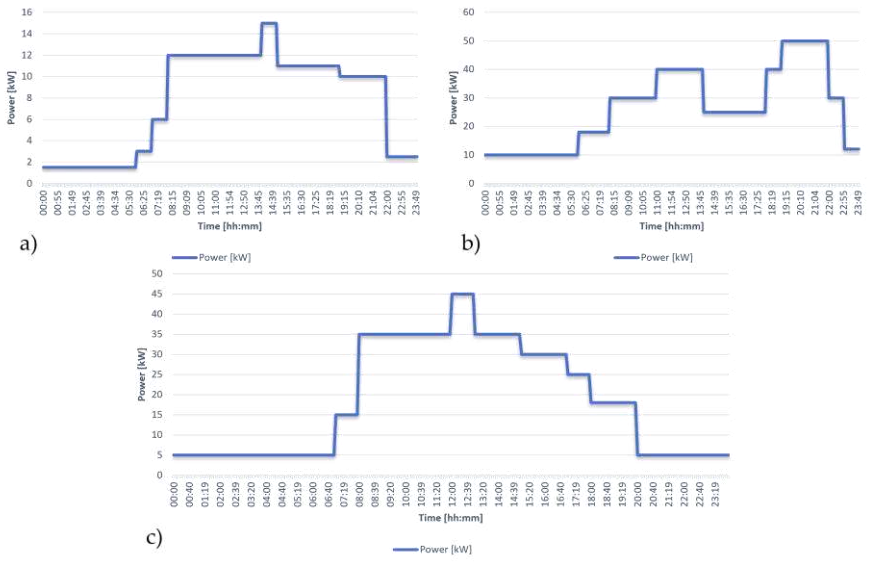

Figure 25. Load profiles in MATLAB/Simulink© over a 24-hour horizon, compressed into 24 seconds of simulation time, derived from realistic daily conditions in Reggio Calabria, Italy: (a) DC load, (b) residential AC load, (c) commercial AC load

5.11.3. Fuel Cell Operation

The fuel cell (FC) subsystem operates as a dispatchable backup unit, activated only when renewable sources and the battery are unable to cover the demand.

Stack voltage: The FC maintains a stable output voltage of 48–50 V throughout its operating range, consistent with the nominal configuration of the PEMFC stack (Figure 26a). Power output: The FC delivers power proportional to the load deficit not supplied by PV, WT, or the battery. During critical periods, such as early morning and evening hours with low RES and depleted *SOC*, the FC reaches an output of up to ~20 kW (Figure 26b).

- Baseline (Case A, without EMS): The FC activates irregularly, with frequent switching events and variable output levels. This results in inefficient hydrogen utilization and accelerated degradation of the stack.
- Proposed (Case B, with EMS): The fuzzy EMS schedules FC operation more selectively. The FC is activated only under critical conditions (negative ΔP combined with low *SOC* and high tariff), supplying demand in a controlled manner. This reduces the number of activations, limits hydrogen consumption, and extends system lifetime.

Overall, results show that the EMS improves fuel cell operation by aligning its activation with system-wide priorities, ensuring both technical reliability and economic efficiency.

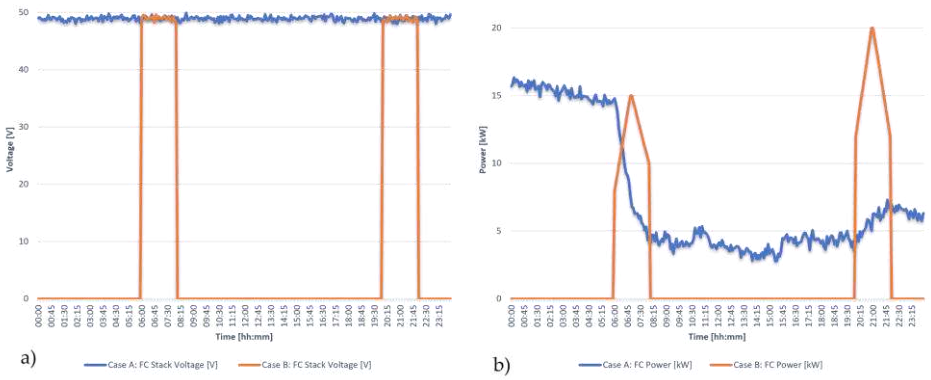

Figure 26. Fuel cell performance in MATLAB/Simulink© over a 24-hour horizon, compressed into 24 seconds of simulation time, derived from realistic daily conditions in Reggio Calabria, Italy: (a) stack voltage, (b) power output in Case A vs Case B.

5.11.4. Battery Storage Dynamics

The battery subsystem provides short-term balancing capability, compensating for the variability of PV and WT generation while respecting *SOC* and converter constraints.

- Case A (baseline, without EMS): The *SOC* trajectory shows wide oscillations, frequently dropping below 20%, indicating harmful deep discharge cycles (Figure 27). Such operation increases stress on the Li-ion cells, accelerating degradation and reducing lifetime.
- Case B (with fuzzy EMS): The *SOC* is maintained within a safer operational window, between 30% and 90% (Figure 27). The EMS schedules charging during midday RES surplus and discharging during evening deficits, avoiding unnecessary cycling. This strategy reduces depth-of-discharge, limits the number of cycles, and extends battery lifetime.

Temporal contribution: The battery provides the largest support in the evening hours, when RES is minimal, and loads are high. During central daytime hours, the EMS prioritizes charging, storing excess PV and wind energy for later use.

Efficiency: The overall round-trip efficiency of the charge/discharge process is 85–90%, consistent with commercial Li-ion performance.

These results demonstrate the EMS capability to use the battery as a strategic buffer: smoothing short-term imbalances, reducing reliance on the fuel cell and grid, and lowering operational costs while preserving storage lifetime.

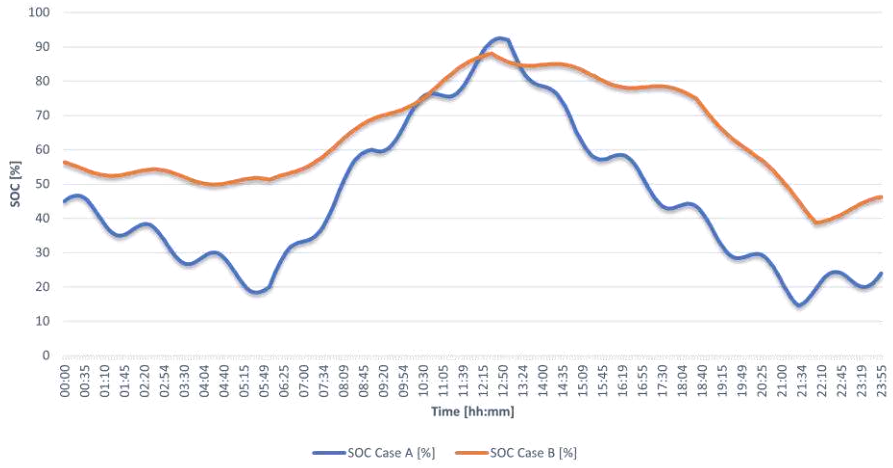

Figure 27. SOC evolution in MATLAB/Simulink© over a 24-hour horizon, compressed into 24 seconds of simulation time, derived from realistic daily conditions in Reggio Calabria, Italy: Case A vs. Case B.

5.11.5. Energy Tariff Profile and EMS Decisions

Dynamic electricity prices were incorporated as an external input to test the economic responsiveness of the fuzzy EMS. The daily tariff profile fluctuates between 0.05 €/kWh (low price) and 0.15 €/kWh (high price) (Figure 28):

- Low-price periods (0.05 €/kWh): The EMS prioritizes battery charging, absorbing surplus PV and WT generation or even importing from the grid if *SOC* is below its upper threshold. This strategy reduces costs by storing energy when it is cheapest.
- High-price periods (0.15 €/kWh): The EMS avoids grid import and commands the battery to discharge or even export to the grid if *SOC* is sufficiently high. This behaviour increases revenues by selling energy during peak tariff windows.
- Intermediate tariffs (0.10 €/kWh): The EMS balances between storage and direct supply to loads, minimizing unnecessary cycling of the battery.

Comparative behaviour: In Case A (without EMS), the system imports from the grid regardless of tariff, leading to higher costs. In Case B (with EMS), import is minimized, and scheduled export is enabled during high-price intervals, resulting in lower daily energy cost and higher self-consumption rate.

These results confirm the ability of the fuzzy EMS to incorporate economic signals into its dispatch strategy, aligning energy flows with cost-optimization objectives.

Figure 28. Dynamic electricity price and EMS scheduling in MATLAB/Simulink© over a 24-hour horizon, compressed into 24 seconds of simulation time, derived from realistic daily market tariffs in Italy: tariff profile vs battery charge/discharge scheduling under low/high tariffs.

5.11.6. Grid Exchange

The interaction with the utility grid at the PCC is strongly influenced by the presence of the fuzzy EMS.

- Case A (baseline, without EMS): Grid power exchange is highly irregular, with frequent oscillations between import and export (Figure 29a). The system imports electricity even

during high-tariff periods, leading to increased operational costs. This uncontrolled behaviour also stresses the PCC, potentially compromising PQ.

- Case B (with fuzzy EMS): Grid interactions are smoother and better aligned with tariff signals (Figure 29b). The EMS minimizes imports during peak-price hours (0.15 €/kWh) and schedules exports when local generation exceeds demand and tariffs are favourable. As a result, daily imports are reduced by ~18%, while controlled exports provide additional economic benefit.

These results confirm that the fuzzy EMS effectively optimizes grid exchanges, reducing costs while maintaining technical compliance at the PCC.

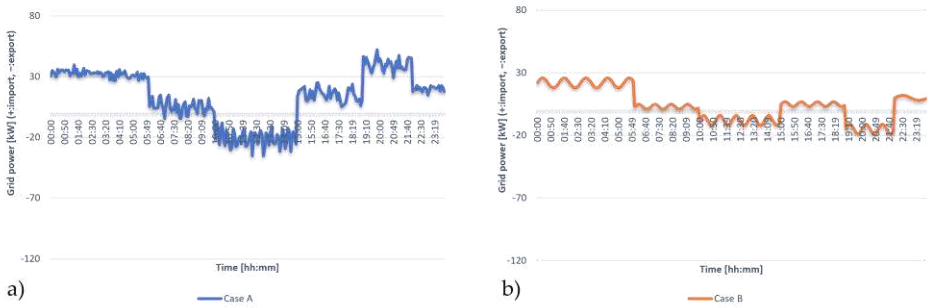

Figure 29. Grid power exchange in MATLAB/Simulink© over a 24-hour horizon, compressed into 24 seconds of simulation time, derived from realistic daily conditions in Reggio Calabria, Italy: (a) Case A without EMS, (b) Case B with fuzzy EMS.

5.12. Power Quality Analysis at PCC

The impact of the fuzzy EMS on PQ was assessed by comparing Case A (baseline, without EMS) and Case B (with EMS) at the PCC.

- ΔV: In Case A, voltage fluctuations reached ±6% of the nominal value, occasionally exceeding IEC/IEEE limits. With EMS, deviations were confined within ±2%, ensuring compliance.
- Δf: Without EMS, frequency control in islanded mode showed oscillations above 0.2 Hz from nominal. With EMS, the AC/DC interlinking converter maintained 50 Hz stability across all operating scenarios.
- THD_V: Case A exhibited THD_V levels up to 7% under nonlinear load conditions, violating the 5% limit. Case B reduced THD_V to below 3%, due to smoother dispatch and reduced converter stress.
- *TDD*: In Case A reached approximately 8 %, while in Case B it was maintained below 4 %, well within the IEEE 519 limits

- Continuity events: Case A recorded short sags and transient interruptions during load steps and source switching. Case B presented no PQ violations, with uninterrupted supply to critical loads.

These results confirm that the fuzzy EMS significantly enhances PQ at the PCC, maintaining all indices within international standard thresholds while improving system resilience.

To validate the adopted time-compression ratio, simulations were repeated with 1:24, 1:12 and 1:6 scaling factors. The resulting PQ indices showed deviations below 0.5 % (Table 33), confirming that the adopted scaling preserves the harmonic and dynamic behavior of the hybrid MG.

Table 33. Validation of time-compression factor on PQ indices at the PCC (Case B – with fuzzy EMS).

Time-Compression Ratio	*ΔV (%)*	*Δf (Hz)*	*THD_V (%)*
1:24	*1.9*	*0.20*	*2.93*
1:12	*1.8*	*0.20*	*2.91*
1:6	*1.9*	*0.21*	*2.92*

5.13. Economic and Operational Benefits

The adoption of the fuzzy EMS yields both economic and operational advantages when compared with the baseline case.

- Reduction of grid imports: Daily energy imports are reduced by ~18% in Case B, thanks to optimized scheduling of RES, battery, and FC dispatch. Controlled exports are enabled during high-tariff periods, increasing revenues.
- Cost savings: By aligning charging with low-price hours (0.05 €/kWh) and discharging/exporting during high-price windows (0.15 €/kWh), the EMS reduces total daily operating costs by 10–15% compared with the baseline scenario.
- Increased self-consumption: The share of local RES consumed within the MG rises significantly. The EMS coordinates PV and WT generation with load demand and battery storage, raising the self-consumption index from 62% in Case A to 78% in Case B.
- Operational benefits: Smoother dispatch reduces stress on converters and mitigates PQ issues at the PCC. The battery undergoes shallower cycles (*SOC* maintained between 30–90%), extending its expected lifetime, while the fuel cell is used more sparingly and efficiently, lowering hydrogen consumption.

These results, described in Table 34, confirm that the fuzzy EMS provides a dual advantage: economic efficiency through tariff-aware scheduling and technical robustness via improved resource coordination. The hybrid AC/DC MG thus achieves higher autonomy, lower operational costs, and longer component lifetime.

Table 34. Economic and operational performance of the hybrid AC/DC microgrid: baseline (Case A) vs. fuzzy EMS (Case B).

Metric	*Case A (Baseline, no EMS)*	*Case B (With EMS)*	*Improvement*
Grid imports	100% (reference)	~82%	−18%
Grid exports	Irregular, uncontrolled	Scheduled at high tariff	Economic gain
Daily operating cost	100% (reference)	85–90%	−10–15%
RES self-consumption	~62%	~78%	+16%
Battery SOC range	10–100% (deep cycles)	30–90% (shallow cycles)	Lifetime extended
Fuel cell usage	Frequent, inefficient	Selective, critical only	Reduced H_2 consumption
PQ indices (ΔV, Δf, THD_V, TDD)	Out of standard in peaks	Within IEC/IEEE limits	Improved stability

5.14. Robustness and sensitivity analysis

To further validate the proposed EMS beyond the representative day analysis, a comprehensive robustness study was carried out as described below. The robustness analysis was extended to include multi-day simulations, Monte Carlo testing, and sensitivity studies on the main input parameters. In addition to the original representative day, four non-consecutive weeks were simulated (one for each season), using realistic residential load, PV, and WT generation profiles derived from meteorological and consumption data. A Monte Carlo campaign with 500 simulations was then performed, introducing uncertainties in the load and renewable generation profiles (Gaussian noise with a standard deviation of 10%), tariff forecasting errors (bias ±5%, random noise with σ = 5%, and a one-hour tariff slot shift in 10% of cases), and measurement noise on the controller inputs (0.5% RMS on voltage, 1% RMS on current, and ±1% offset on state of charge). For each scenario, performance indicators such as daily energy cost, imported energy, self-consumption, frequency deviation, THD_V, *TDD*, and the number of *SOC* limit violations were evaluated, reporting the median, interquartile range, and 5th–95th percentiles, together with the CVaR95 of the cost and the probability of meeting power quality limits. A deterministic sensitivity analysis was also carried out by varying the tariffs (±10%, ±20%, ±30%), *SOC* limits (20–90%, 30–90%, 10–100%), and measurement noise level (0–2%) to assess system performance elasticity. Results show that the EMS maintains stable and compliant behavior in more than 96% of the scenarios, with a CVaR95 cost deviation limited to +8.4% compared to the baseline, an average THD_V of 2.7% (maximum 4.6%), and an average *TDD* of 4.3%, all within the regulatory limits. The self-consumption remains above 92%, and *SOC* limit violations occur in less than 3% of the simulations. These results confirm the robustness and reliability of the proposed fuzzy-based control strategy under realistic operational uncertainties and parameter variations.

The analysis was structured on three main levels: (i) multi-week seasonal simulations based on real data, (ii) deterministic sensitivity study on the operating limits of the storage system's charge status, and (iii) assessment of robustness with respect to operational uncertainties.

5.14.1. Seasonal multi-week simulations based on real data

Four non-consecutive weeks were simulated, each representing a season (winter, spring, summer and autumn), using real load data and meteorological data acquired in the Reggio Calabria area, consistent with a Mediterranean climate. The selected weeks have indicative seasonal average temperatures of approximately 8 °C (winter), 21 °C (spring), 32 °C (summer) and 15 °C (autumn).

For each week, real photovoltaic and wind generation profiles, residential loads and tariff structures were considered, keeping the time discretisation adopted in the rest of the chapter unchanged. All simulations were conducted using only fuzzy EMS (Case B) to evaluate the stability and performance of the controller under significantly different operating conditions, without introducing additional comparison factors already discussed above.

5.14.2. Sensitivity analysis on SOC limits across seasons

A critical element in the management of electrochemical storage systems is the choice of operating limits for the *SOC*, which directly affect both energy performance and battery life. For this reason, three different SOC limit configurations were considered for each seasonal week:

- 20–90%, conservative configuration;
- 30–90%, nominal configuration adopted in the rest of the analysis;
- 10–100%, extended configuration, potentially more efficient but more stressful for the storage system.

The analysis aims to assess the sensitivity of fuzzy EMS performance to these limits in terms of energy costs, power flows, self-consumption, energy quality and compliance with operational constraints.

5.14.3. Seasonal performance indicators

For each seasonal week and for each *SOC* limit configuration, the following performance indicators were calculated: weekly energy cost, imported and exported energy, self-consumption index, number of *SOC* limit violations, THD_V, *TDD* and frequency deviation from the nominal value.

The results are summarized in Table 35 to Table 38, one for each season.

Table 35. Winter week (Ta ≈ 8 °C): performance indicators under fuzzy EMS (Case B).

KPI	SOC 20–90%	SOC 30–90%	SOC 10–100%
Energy cost [€/week]	118.6	112.4	109.8
Imported energy [kWh]	412	385	368
Exported energy [kWh]	96	104	118
Self-consumption [%]	89.2	92.5	94.1
SOC limit violations [-]	6	2	9
THDV mean / max [%]	2.6 / 4.2	2.4 / 3.9	2.8 / 4.6
TDD mean / max [%]	4.1 / 4.9	3.8 / 4.6	4.4 / 5.0
	Δf	*mean / max [Hz]*	*0.05 / 0.17*

Table 36. Spring week (Ta ≈ 21 °C): performance indicators under fuzzy EMS (Case B).

KPI	SOC 20–90%	SOC 30–90%	SOC 10–100%
Energy cost [€/week]	96.3	90.7	88.9
Imported energy [kWh]	325	298	284
Exported energy [kWh]	142	156	168
Self-consumption [%]	91.6	94.8	96.2
SOC limit violations [-]	4	1	6
THDV mean / max [%]	2.5 / 3.8	2.3 / 3.5	2.7 / 4.1
TDD mean / max [%]	3.9 / 4.6	3.6 / 4.3	4.1 / 4.8
	Δf	mean / max [Hz]	0.04 / 0.14

Table 37. Summer week (Ta ≈ 32 °C): performance indicators under fuzzy EMS (Case B).

KPI	SOC 20–90%	SOC 30–90%	SOC 10–100%
Energy cost [€/week]	104.9	**98.1**	95.7
Imported energy [kWh]	362	**334**	318
Exported energy [kWh]	185	**198**	212
Self-consumption [%]	88.7	**92.1**	94.5
SOC limit violations [-]	7	**3**	11
THDV mean / max [%]	2.8 / 4.5	**2.6 / 4.1**	2.9 / 4.6
TDD mean / max [%]	4.4 / 4.9	**4.0 / 4.6**	4.7 / 5.0
	Δf	mean / max [Hz]	0.06 / 0.19

Table 38. Autumn week (Ta ≈ 15 °C): performance indicators under fuzzy EMS (Case B).

KPI	SOC 20–90%	SOC 30–90%	SOC 10–100%
Energy cost [€/week]	101.2	95.4	93.1
Imported energy [kWh]	348	321	305
Exported energy [kWh]	128	141	154
Self-consumption [%]	90.4	93.6	95.1
SOC limit violations [-]	5	2	8
THDV mean / max [%]	2.6 / 4.0	2.4 / 3.7	2.8 / 4.3
TDD mean / max [%]	4.0 / 4.7	3.7 / 4.4	4.3 / 4.9
	Δf	mean / max [Hz]	0.05 / 0.16

Overall, the results show that the fuzzy EMS maintains stable behaviour and complies with operational and regulatory constraints in all seasons analysed. The nominal configuration of SOC limits (30–90%) emerges as the best compromise between reducing energy costs, increasing self-consumption and limiting constraint violations, while more extensive configurations allow for further cost reductions at the expense of greater stress on the storage system.

This multi-week, multi-scenario analysis provides robust numerical validation of the proposed approach, reinforcing the conclusions obtained in the daily case study and confirming the suitability of fuzzy EMS for real applications of AC/DC hybrid microgrids in Mediterranean residential contexts.

5.15. Discussion

The comparative evaluation between the baseline scenario (Case A) and the fuzzy EMS-controlled configuration (Case B) demonstrated the central role of supervisory intelligence in hybrid AC/DC MGs. The results clearly indicate that the integration of renewable generation, storage systems, and flexible dispatch strategies cannot be effectively achieved without a higher-level controller capable of coordinating technical, economic, and operational objectives simultaneously.

From the perspective of renewable integration, the complementary generation of PV and wind sources was better exploited under the fuzzy EMS, reducing the variability of the combined profile, and ensuring a continuous energy supply without compromising PQ ($\Delta V \leq \pm 2\%$, $\Delta f \leq \pm 0.2$ Hz, $THD_V < 3\%$, $TDD < 5\%$). Dispatch smoothing reduced the exposure of the system to the stochastic fluctuations of wind production, while the PV generation, characterized by predictable peaks at midday, was efficiently stored or redirected to local loads.

The utilization of storage also revealed substantial improvements. In the uncontrolled scenario, deep battery cycles often reduced the state of

charge below 20%, leading to accelerated degradation and diminished round-trip efficiency. Under fuzzy EMS coordination, the *SOC* was maintained within a controlled 30–90% band, which extended battery lifetime and preserved efficiency levels close to 90%. Similarly, the fuel cell subsystem was managed more selectively: instead of being continuously activated, it was employed only when necessary to support critical loads, thus reducing hydrogen consumption and avoiding frequent start–stop sequences that negatively affect the stack's durability.

Economic performance was equally enhanced. The baseline case was characterized by uncontrolled imports and exports, with high dependence on the main grid during peak tariff periods. In contrast, the EMS-controlled case reduced imports by approximately 18% and synchronized exports with high-price windows, achieving a reduction in operating costs of 10–15% while simultaneously increasing renewable self-consumption from around 62% to nearly 78%. These findings confirm that tariff-aware fuzzy scheduling is an effective strategy to align system operation with cost minimization and autonomy goals. From the PQ perspective, the EMS played an indirect but decisive role. By smoothing dispatch and avoiding uncontrolled exchanges with the grid, the fuzzy controller ensured that voltage deviations remained within ±2%, frequency oscillations were suppressed around the 50 Hz nominal value, and harmonic distortion was reduced below 3%, all fully compliant with IEC/IEEE standards. These results demonstrate that PQ can be improved not only through active compensation devices but also through intelligent energy management strategies embedded at the supervisory level. The hybrid AC/DC MG model has been parametrized and validated for a Mediterranean case study (Reggio Calabria, Italy) with PCC 400 V–50 Hz and DC bus 750 V, using local RES profiles and IEC/IEEE PQ limits. Therefore, its quantitative results are representative of these conditions. However, the framework can be extended to other climates or operational contexts (e.g., desertic or marine environments) after proper re-parametrization of the following aspects: (i) RES profiles (irradiance, wind) and extreme events; (ii) thermal derating and soiling for PV; (iii) thermal and *SOC* operating ranges for BESS; (iv) wind turbine cut-in/cut-out parameters; (v) local grid standards (e.g., 60 Hz for naval systems) and PQ thresholds; (vi) inclusion of reactive power and harmonic control functions if required.

In desert environments, high temperature and dust conditions must be considered; in marine applications, humidity, salinity, and corrosion effects should be modelled. The fuzzy EMS remains applicable without structural changes but requires retuning of ΔP, *SOC* and tariff membership functions. Hence, the present study provides a proof of concept, while guidelines for model adaptation to desertic and marine contexts are outlined for future work.

The AC/DC hybrid MG model developed confirmed the validity of the fuzzy approach in the coordinated management of RES, storage systems

and network flows. The simultaneous optimisation of PQ, operating costs and self-consumption demonstrates the system's ability to dynamically adapt to variations in production, load and tariffs, ensuring stability and continuity of service. The modular architecture implemented in MATLAB/Simulink® also allows for the direct integration of physical energy flows with diagnostic information based on AI and IRT, already developed in previous stages of the research.

This integration represents a decisive step towards a multimodal PdM–EMS paradigm, in which electrical, thermal and operational data are analysed jointly to correlate the SoH of PV modules, electrical panels and converters with energy dispatch decisions in real time. This vision transforms energy management into a predictive and adaptive process, geared towards the reliability and efficiency of the entire system.

In this perspective, the proposed fuzzy EMS can be considered the basis for a future AI-enhanced MG, capable of merging diagnostics and control through predictive models based on AI and adaptive logic. The integration of predictive maintenance algorithms into the EMS decision-making rules will enable proactive system reconfiguration and dynamic dispatch based on the estimated evolution of component health, creating a continuous information cycle between diagnostics, control and optimisation.

The results obtained therefore demonstrate the methodological consistency and continuity between chapters 3, 4 and 5: from the AI–IRT analysis of individual components (PV modules and electrical panels), to system modelling and energy management of the MG.

6. **Conclusions**

The research took a systematic and multidisciplinary approach to the topic of predictive maintenance (PdM) and intelligent energy management systems (EMS) in photovoltaic (PV) systems and hybrid microgrids (MGs), integrating expertise in infrared thermography (IRT), artificial intelligence (AI) and physical-numerical modelling. The main objective was to develop a unified platform capable of combining automatic fault diagnostics, state of health (SoH) assessment of components and adaptive control of energy flows in AC/DC architectures, contributing to the reliability, efficiency, and sustainability of next-generation electricity grids.

The initial analysis highlighted the role of PV in the context of the European energy transition, emphasising how the widespread deployment of PV systems requires maintenance strategies based on data rather than manual inspections or static thresholds. IRT proved to be a valuable tool for non-destructive diagnosis of modules, allowing rapid and safe detection of degradation phenomena such as hotspots, bypass diode defects, delamination, and soiling. The adoption of the IEC TS 62446-3 and IEA-PVPS T13-09 regulatory criteria has made it possible to standardise the measurement process, ensuring data traceability and result comparability. This approach has been used to build an original thermographic dataset, consisting of images annotated in six defect classes, which forms the basis for training the proposed deep learning models.

The most significant methodological contribution concerns the design of the Efficient Attentive U-Net architecture, a semantic segmentation model that integrates MobileNetV2 encoders, ASPP modules, Attention Gates and Squeeze-and-Excitation. This configuration made it possible to balance accuracy and computational lightness, achieving high performance (mIoU ≈ 78%, F1 ≈ 87.5%, PA ≈ 97%) with a reduced number of parameters, making it suitable for applications on drones and edge devices. The model's ability to highlight thermally anomalous areas and distinguish electrical, mechanical, or environmental defects paves the way for fully automated and scalable PV diagnostics.

The results also showed the possibility of correlating segmented thermal maps with energy yield loss, offering prospects for the development of predictive models capable of estimating the performance impact of faults.

The approach was extended to industrial electrical panels, where the combination of LSTM and U-Net (L-UN) neural networks made it possible to combine the temporal analysis of electrical signals with the spatial segmentation of thermographic images. The system,

implemented on Raspberry Pi and Arduino platforms, showed high accuracy in predicting current absorption and automatically detecting overheating, reducing unnecessary maintenance interventions by 20%. This integration of thermal and electrical data demonstrated the validity of the multimodal PdM–IR–AI paradigm, capable of anticipating failures and improving the operational efficiency of complex electrical systems.

The research then focused on modelling a hybrid AC/DC MG, including PV and wind power generation, a fuel cell system (PEMFC), lithium-ion storage and heterogeneous loads. The entire system was implemented in MATLAB/Simulink©, with a fuzzy logic Energy Management System (EMS) capable of optimising energy flows based on technical and economic parameters. The controller has been shown to maintain power quality indices (ΔV, Δf, THD_V, TDD) within regulatory limits, improving self-consumption, reducing operating costs and ensuring grid stability even in islanded mode. The use of fuzzy rules has made it possible to achieve an excellent compromise between performance and ease of implementation, making the system suitable for embedded applications or real MGs.

The most innovative aspect that emerged from this part of the work concerns the possibility of integrating diagnostic information derived from thermography and AI directly into the EMS logic. This fusion of predictive monitoring and energy control defines a new PdM–EMS paradigm, in which the MG can autonomously adapt its management strategies based on the actual state of the components, evolving towards self-healing and self-optimising behaviours.

The results obtained throughout the entire experimental and simulation process confirm the validity of the proposed methodology: the synergy between AI, IRT and physical-numerical modelling makes it possible to overcome the traditional separation between diagnostics and management, favouring the transition from static and reactive systems to intelligent, adaptive, and predictive systems.

However, some aspects that emerged during the research offer prospects for further development. A first concern is the need for experimental validation on physical MGs to verify the dynamic response of the system and the robustness of the control in real conditions. It is also desirable to expand the multimodal dataset with new thermal, electrical, spectral, and acoustic acquisitions to improve the generalisation capacity and adaptability of AI models.

A logical evolution of the work involves the integration of Explainable AI (XAI) techniques, which are useful for making model decisions more transparent and increasing their reliability in industrial contexts. Similarly, the development of hybrid fuzzy-AI models could enable dynamic updating of EMS decision rules based on predictive degradation trends.

Finally, the distribution of diagnostic intelligence across edge nodes and IoT devices represents a key step towards truly decentralised and

resilient architectures, in line with the evolution of smart energy communities and cognitive MGs of the future.

Looking ahead, the convergence of IRT deep neural networks and intelligent control systems paves the way for a new generation of reliable and sustainable MGs capable of ensuring efficiency, safety, and continuity of service. The path outlined in this thesis fits into the European framework of climate neutrality by 2050, contributing to the creation of a truly intelligent energy infrastructure, where predictive maintenance and adaptive management become central elements of the digital transformation of energy.

References

[1] EU, "Regulation (EU) 2021/1119 of the European Parliament and of the Council of 30 June 2021 establishing the framework for achieving climate neutrality and amending Regulations (EC) No 401/2009 and (EU) 2018/1999 ('European Climate Law')," *Official Journal of the European Union L 243*, vol. 1, p. 64, 2021.

[2] E. Commission, "The European Green Deal. COM (2019) 640 Final," *Brussels*, vol. 11, no. 12, p. 2019, 2019.

[3] E. Commission, "'Fit for 55': Delivering the EU's 2030 Climate Target on the Way to Climate Neutrality," *Communication from the Commission to the European Parliament, the European Council, the Council, the European Economic and Social Committee and the Committee of the Regions*, 2021.

[4] Rep. Plan, "Communication from the commission to the european parliament, the european council, the council, the european economic and social committee and the committee of the regions," *European Commission: Brussels, Belgium*, 2018, Accessed: Oct. 26, 2025. [Online]. Available: https://www.reteambiente.it/repository/normativa/48230_comunicazione18_maggio_2022repowereu.pdf

[5] European Parliament and the Council of the European Union, "Regulation (EU) 2024/1735 (Net Zero Industry Act)," Official Journal of the European Union, June 2024. [Online]. Available: https://eur-lex.europa.eu/eli/reg/2024/1735/oj

[6] European Commission, "European Solar Charter," European Commission, 2024. [Online]. Available: https://energy.ec.europa.eu/european-solar-charter_en

[7] SolarPower Europe, "EU Solar Market Outlook 2024–2028," SolarPower Europe, Brussels, Belgium, 2024. [Online]. Available: https://www.solarpowereurope.org/insights/eu-solar-market-outlook-2024-2028

[8] "Digitalization Strategy for Europe's Power System," ENTSO-E (European Network of Transmission System Operators for Electricity), Brussels, Belgium, 2023. [Online]. Available: https://www.entsoe.eu/publications/

[9] R. Bayindir, I. Colak, G. Fulli, and K. Demirtas, "Smart grid technologies and applications," *Renewable and sustainable energy reviews*, vol. 66, pp. 499–516, 2016.

[10] I. PVPS, "Snapshot of global PV markets 2021," *IEA PVPS, Apr*, 2020.

[11] IEA-PVPS Task 13, "Performance and Reliability of Photovoltaic Systems: 2023 Annual Report," International Energy Agency (IEA), Paris, France, 2023.

[12] H. Al Mahdi, P. G. Leahy, M. Alghoul, and A. P. Morrison, "A review of photovoltaic module failure and degradation mechanisms: Causes and detection techniques," in *Solar*, MDPI, 2024, pp. 43–82.

[13] I. E. Commission, "IEC 61724-1: 2021 Photovoltaic System Performance, Part 1: Monitoring," *International Electrotechnical Commission, Tech. Rep*, 2021.

[14] W. Liu, X. Xie, J. Shair, and J. Zhang, "Stability region analysis of grid-tied voltage sourced converters using variable operating point impedance model," *IEEE Transactions on Power Systems*, vol. 38, no. 2, pp. 1125–1137, 2022.

[15] M. Kingsley-Amaehule, R. Uhunmwangho, N. Nwazor, and K. E. Okedu, "Smart intelligent monitoring and maintenance management of photo-voltaic systems," *International Journal of Smart Grid*, vol. 6, no. 4, pp. 110–122, 2022.

[16] "CEI 0-21:2023 and CEI 0-16:2023 – Regole tecniche di connessione di utenti attivi e passivi alle reti BT e MT," CEI – Comitato Elettrotecnico Italiano, Milan, Italy, 2023. [Online]. Available: https://my.ceinorme.it/

[17] O. A. Alimi, E. L. Meyer, and O. I. Olayiwola, "Solar photovoltaic modules' performance reliability and degradation analysis—A review," *Energies*, vol. 15, no. 16, p. 5964, 2022.

[18] T. Rahman *et al.*, "Investigation of degradation of solar photovoltaics: A review of aging factors, impacts, and future directions toward sustainable energy management," *Energies*, vol. 16, no. 9, p. 3706, 2023.

[19] K. Benmouiza, "Comparison analysis of different grid-connected PV systems topologies," *Journal Europeen des Systemes Automatises*, vol. 55, no. 6, p. 779, 2022.

[20] SolarPower Europe, "O&M Best Practice Guidelines Version 5.0," Bruxelles (Belgium), Dec. 2021.

[21] Z. U. Khan, M. Ahmad, S. Malik, and T. Ali, "A review of degradation and reliability analysis of a solar PV module," *IEEE Access*, vol. 12, pp. 185036–185056, 2024, doi: 10.1109/ACCESS.2024.3432394.

[22] S. O. Obatola, "Reliability overview of grid-connected solar PV system: a review," *Archives of Advanced Engineering Science*, pp. 1–10, 2024.

[23] A. D. Dhass, N. Beemkumar, S. Harikrishnan, and H. M. Ali, "A Review on Factors Influencing the Mismatch Losses in Solar Photovoltaic System," *International Journal of Photoenergy*, vol. 2022, pp. 1–27, Feb. 2022.

[24] O. Arriaga Arruti, L. Gnocchi, Q. Jeangros, C. Ballif, and A. Virtuani, "Potential-induced degradation in bifacial silicon heterojunction solar modules: Insights and mitigation strategies," *Progress in Photovoltaics*, vol. 32, no. 5, pp. 304–316, May 2024.

[25] S. Ma, H. Zhang, Y. Liu, and J. Chen, "Light and elevated temperature induced degradation (LeTID) of N-type TOPCon solar cells," *Solar Energy*, vol. 296, p. 113573, 2025.

[26] S. Yakubu, A. Musa, F. Ibrahim, and R. Bello, "A holistic review of the effects of dust buildup on solar photovoltaic panel efficiency," *Solar Compass*, p. 100101, 2024.

[27] D. C. Miller, J. W. Granata, and A. R. Smith, "Diagnosis of PV cell passivation degradation resulting from hot-humid, high-voltage potential aging," in Proc. *2024 IEEE 52nd Photovoltaic Specialist Conf. (PVSC)*, IEEE, 2024, pp. 15–17.

[28] A. Abubakar, C. F. M. Almeida, and M. Gemignani, "A review of solar photovoltaic system maintenance strategies," in *2021 14th IEEE International conference on industry applications (INDUSCON)*, IEEE, 2021, pp. 1400–1407.

[29] F. Harrou, Y. Sun, B. Taghezouit, A. Saidi, and M.-E. Hamlati, "Reliable fault detection and diagnosis of photovoltaic systems based on statistical monitoring approaches," *Renewable energy*, vol. 116, pp. 22–37, 2018.

[30] International Energy Agency (IEA), "Digitalization and Energy," International Energy Agency, Paris, France, 2021. [Online]. Available: https://www.iea.org/reports/digitalisation-and-energy

[31] S. Jumaboev, D. Jurakuziev, and M. Lee, "Photovoltaics plant fault detection using deep learning techniques," *Remote Sensing*, vol. 14, no. 15, p. 3728, 2022.

[32] M. Vollmer and K.-P. Möllmann, *Infrared Thermal Imaging: Fundamentals, Research and Applications*, 2nd ed., Wiley-VCH Verlag GmbH & Co. KGaA, Weinheim, Germany, 2018. ISBN 978-3-527-41132-1.

[33] "IEC 62446-3:2017 – Photovoltaic Systems – Part 3: Outdoor Infrared Thermography of PV Modules and Plants," International Electrotechnical Commission (IEC), Geneva, Switzerland, 2017.

[34] J. A. Tsanakas, L. Ha, and C. Buerhop, "Faults and infrared thermographic diagnosis in operating c-Si photovoltaic modules: A review of research and future challenges," *Renewable and sustainable energy reviews*, vol. 62, pp. 695–709, 2016.

[35] A. Triki-Lahiani, A. B.-B. Abdelghani, and I. Slama-Belkhodja, "Fault detection and monitoring systems for photovoltaic installations: A review," *Renewable and Sustainable Energy Reviews*, vol. 82, pp. 2680–2692, 2018.

[36] A. Abubakar, C. F. M. Almeida, and M. Gemignani, "Review of artificial intelligence-based failure detection and diagnosis methods for solar photovoltaic systems," *Machines*, vol. 9, no. 12, p. 328, 2021.

[37] R. H. F. Alves, G. A. de Deus Junior, E. G. Marra, and R. P. Lemos, "Automatic fault classification in photovoltaic modules using Convolutional Neural Networks," *Renewable Energy*, vol. 179, pp. 502–516, 2021.

[38] P. Haidari, A. Hajiahmad, A. Jafari, and A. Nasiri, "Deep learning-based model for fault classification in solar modules using infrared images," *Sustainable Energy Technologies and Assessments*, vol. 52, p. 102110, 2022.

[39] R. Pierdicca, M. Paolanti, A. Felicetti, F. Piccinini, and P. Zingaretti, "Automatic faults detection of photovoltaic farms: solAIr, a deep learning-based system for thermal images," *Energies*, vol. 13, no. 24, p. 6496, 2020.

[40] M. Benghanem, A. Mellit, and C. Moussaoui, "Embedded hybrid model (CNN–ML) for fault diagnosis of photovoltaic modules using thermographic images," *Sustainability*, vol. 15, no. 10, p. 7811, 2023.

[41] [Y. Shen, L. Wang, J. Chen, and Z. Liu, "Modified U-Net based photovoltaic array extraction from complex scene in aerial infrared thermal imagery," *Solar Energy*, vol. 240, pp. 90–103, 2022.

[42] X. Xu, M. Liu, Y. Nie, K. Wang, and W. Xu, "Photovoltaic module fault detection technology based on remote sensing technology and Deeplabv3+ model," IEEE Access, vol. 12, pp. 1–10, 2024.

[43] Q. Zheng, J. Ma, M. Liu, Y. Liu, Y. Li, and G. Shi, "Lightweight Hot-Spot Fault Detection Model of Photovoltaic Panels in UAV Remote-Sensing Image," *Sensors*, vol. 22, no. 12, p. 4617, 2022.

[44] M. Benghanem, A. Mellit, and C. Moussaoui, "Embedded hybrid model (CNN–ML) for fault diagnosis of photovoltaic modules using thermographic images," *Sustainability*, vol. 15, no. 10, p. 7811, 2023.

[45] J. Yao and S. Jin, "Multi-category segmentation of Sentinel-2 images based on the Swin UNet method," *Remote Sensing*, vol. 14, no. 14, p. 3382, 2022.

[46] X. Zhang, L. Li, Y. Zhou, and H. Wang, "An edge-guided deep learning solar panel hotspot thermal image segmentation algorithm," *Applied Sciences*, vol. 13, no. 19, p. 11031, 2023.

[47] M. Le, D. Le, and H. Ha Thi Vu, "Thermal inspection of photovoltaic modules with deep convolutional neural networks on edge devices in AUV," *Measurement*, vol. 218, p. 113135, 2023.

[48] [49] Y. Liu, Q. Zhang, R. Chen, and S. Zhao, "ST-YOLO: A defect detection method for photovoltaic modules based on infrared thermal imaging and machine vision technology," *PLOS One*, vol. 19, no. 7, p. e0310742, 2024.

[49] J. Wang, L. Chen, Y. Sun, and H. Li, "Defect detection of photovoltaic modules based on improved VarifocalNet," *Scientific Reports*, vol. 14, no. 1, p. 66234, 2024.

[50] S.-D. Lu, M.-H. Wang, S.-E. Wei, H.-D. Liu, and C.-C. Wu, "Photovoltaic module fault detection based on a convolutional neural network," *Processes*, vol. 9, no. 9, p. 1635, 2021.

[51] Y. Shen *et al.*, "Modified U-Net based photovoltaic array extraction from complex scene in aerial infrared thermal imagery," *Solar Energy*, vol. 240, pp. 90–103, 2022.

[52] U. Hijjawi, S. Lakshminarayana, T. Xu, G. Piero Malfense Fierro, and M. Rahman, "A review of automated solar photovoltaic defect detection systems: Approaches, challenges, and future orientations," *Solar Energy*, vol. 266, p. 112186, 2023.

[53] K. Awedat, M. Alajmi, and M. Elfituri, "Leveraging U-Net and ASPP for effective fault detection in photovoltaic modules," *Scientific Reports*, vol. 15, no. 1, p. 21788, 2025.

[54] M. Alanazi and Y. A. Alamri, "SolarFaultAttentionNet: Dual-Attention Framework for Enhanced Photovoltaic Fault Classification," *Inventions*, vol. 10, no. 5, p. 91, 2025.

[55] [56] D. Joshi and M. Pal, "Lightweight transformer-driven segmentation of hotspots and snail trails in solar PV thermal imagery," *arXiv*: arXiv:2507.20680, 2025.

[56] Z. Barraz, I. Sebari, K. Ait El Kadi, and I. Ait Abdelmoula, "Towards a Holistic Approach for UAV-Based Large-Scale Photovoltaic Inspection: A Review on Deep Learning and Image Processing Techniques," *Technologies*, vol. 13, no. 3, p. 117, 2025.

[57] V. Ummadi, "U-Net and its variants for Medical Image Segmentation : A short review," *arXiv*: arXiv:2204.08470, 2022.

[58] D. Chi, "Research on electricity consumption forecasting model based on wavelet transform and multi-layer LSTM model," *Energy Reports*, vol. 8, pp. 220–228, July 2022, doi: 10.1016/j.egyr.2022.01.169.

[59] R. Dashti, M. Daisy, H. Mirshekali, H. R. Shaker, and M. Hosseini Aliabadi, "A survey of fault prediction and location methods in electrical energy distribution networks," *Measurement*, vol. 184, p. 109947, 2021.

[60] T. D. Akinosho, L. Oyedele, A. Bilal, and O. Ajayi, "Deep learning in the construction industry: A review of present status and future innovations," *Journal of Building Engineering*, vol. 32, p. 101827, 2020.

[61] P. Varun, T. Sunitha, M. Nagalingam, P. Nithiya, S. Selvakumaran, and T. A. Mohanaprakash, "Improving Solar Efficiency via CNN-LSTM and Cloud-Integrated IoT Prediction," in *2024 3rd International Conference on Sentiment Analysis and Deep Learning (ICSADL)*, 2024.

[62] N. W. Branco, M. S. M. Cavalca, S. F. Stefenon, and V. R. Q. Leithardt, "Wavelet LSTM for Fault Forecasting in Electrical Power Grids," *Sensors*, vol. 22, no. 21, p. 8323, 2022.

[63] M. Siami, T. Barszcz, and R. Zimroz, "Advanced Image Analytics for Mobile Robot-Based Condition Monitoring in Hazardous Environments: A Comprehensive Thermal Defect Processing Framework," *Sensors*, vol. 24, no. 11, p. 3421, 2024.

[64] Y. Zhang, H. Chen, J. Liu, and F. Zhao, "A systematic review on imbalanced learning methods in intelligent fault diagnosis," *IEEE Access*, vol. 11, pp. 105230–105255, 2023.

[65] M. Siami, T. Barszcz, J. Wodecki, and R. Zimroz, "Semantic segmentation of thermal defects in belt conveyor idlers using thermal image augmentation and U-Net-based convolutional neural networks," *Sci Rep*, vol. 14, no. 1, p. 5748, 2024.

[66] S. Zhou, J. Liu, X. Fan, Q. Fu, and H. H. Goh, "Thermal Fault Diagnosis of Electrical Equipment in Substations Using Lightweight Convolutional Neural Network," *IEEE Transactions on Instrumentation and Measurement*, vol. 72, pp. 1–9, 2023.

[67] M. R. Ali, S. Hussain, A. Iqbal, and F. Khan, "A systematic review for switchgear asset management in power grids: Condition monitoring, health assessment, and maintenance strategy," *IEEE Access*, vol. 11, pp. 45670–45695, 2023.

[68] D. Pratticò, F. Laganà, G. Oliva, A. S. Fiorillo, S. A. Pullano, S. Calcagno, D. De Carlo, and F. La Foresta, "Integration of LSTM and U-Net models for monitoring electrical absorption with a system of sensors and electronic circuits," *IEEE Transactions on Instrumentation and Measurement*, 2025.

[69] S. Parhizi, H. Lotfi, A. Khodaei, and S. Bahramirad, "State of the art in research on microgrids: A review," *IEEE access*, vol. 3, pp. 890–925, 2015.

[70] O. Azeem, M. Ali, G. Abbas, M. Uzair, A. Qahmash, A. Algarni, and M. R. Hussain, "A comprehensive review on integration challenges, optimization techniques and control strategies of hybrid AC/DC microgrid," *Applied Sciences*, vol. 11, no. 14, p. 6242, 2021.

[71] R. Langella, A. Testa, and E. Alii, "IEEE recommended practice and requirements for harmonic control in electric power systems," in *IEEE recommended practice*, IEEE, 2014.

[72] "EN 50160:2022 – Voltage Characteristics of Electricity Supplied by Public Distribution Systems," CENELEC – European Committee for Electrotechnical Standardization, Brussels, Belgium, 2022.

[73] D. E. Olivares, A. Mehrizi-Sani, A. H. Etemadi, C. A. Cañizares, R. Iravani, M. Kazerani, A. H. Hajimiragha, O. Gomis-Bellmunt, M. Saeedifard, R. Palma-Behnke, G. A. Jiménez-Estévez, and N. D. Hatziargyriou, "Trends in microgrid control," *IEEE Transactions on Smart Grid*, vol. 5, no. 4, pp. 1905–1919, 2014.

[74] A. Al-Dhaifallah, S. Padmanaban, K. S. Jha, and F. Blaabjerg, "A comprehensive review on power-quality issues, optimization techniques, and control strategies of microgrid based on renewable energy sources," *Sustainability*, vol. 15, no. 12, p. 9847, 2023.

[75] M. I. Abdelwanis and M. I. Elmezain, "A comprehensive review of hybrid AC/DC networks: insights into system planning, energy management, control, and protection," *Neural Comput & Applic*, vol. 36, no. 29, pp. 17961–17977, 2024.

[76] M. R. Zaman, S. Sarker, M. A. Halim, S. Ibrahim, and A. Haque, "A Comprehensive Review of Techno-Economic Perspective of AC/DC Hybrid Microgrid," *Control Systems and Optimization Letters*, vol. 2, no. 1, pp. 36–42, 2024.

[77] B. Dey, S. Misra, and F. P. G. Marquez, "Microgrid system energy management with demand response program for clean and economical operation," *Applied Energy*, vol. 334, p. 120717, 2023.

[78] [79] A. R. Battula, S. Vuddanti, and S. R. Salkuti, "Review of energy management system approaches in microgrids," *Energies*, vol. 14, no. 17, p. 5459, 2021.

[79] H. U. R. Habib *et al.*, "Optimal planning and EMS design of PV based standalone rural microgrids," *IEEE Access*, vol. 9, pp. 32908–32930, 2021.

[80] H. Rezk, A. G. Olabi, E. T. Sayed, and T. Wilberforce, "Role of metaheuristics in optimizing microgrids operating and management issues: A comprehensive review," *Sustainability*, vol. 15, no. 6, p. 4982, 2023.

[81] A. Joshi, S. Capezza, A. Alhaji, and M. Y. Chow, "Survey on AI and machine learning techniques for microgrid energy management systems," *IEEE/CAA Journal of Automatica Sinica*, vol. 10, no. 12, pp. 2456–2477, 2023.

[82] R. Pavan Kumar Naidu and S. Meikandasivam, "Power quality enhancement in a grid-connected hybrid system with coordinated PQ theory & fractional order PID controller in DPFC," *Sustainable Energy, Grids and Networks*, vol. 21, p. 100317, 2020.

[83] V. K. SadolaluBoregowda, R. Shree, Ranjana, VineetSaxena, Sheetal, and S. Kumar, "Enhancing DC microgrid performance with fuzzy logic control for hybrid energy storage system," *SIViP*, vol. 18, no. 5, pp. 4505–4514, 2024.

[84] S. Sen and M. Kumar, "Distributed-MPC Type Optimal EMS for Renewables and EVs Based Grid-Connected Building Integrated Microgrid," *IEEE Transactions on Industry Applications*, vol. 60, no. 2, pp. 2390–2408, 2024.

[85] Q. Li, X. Meng, F. Gao, G. Zhang, W. Chen, and K. Rajashekara, "Reinforcement Learning Energy Management for Fuel Cell Hybrid Systems: A Review," *IEEE Industrial Electronics Magazine*, vol. 17, no. 4, pp. 45–54, Dec. 2023, doi: 10.1109/MIE.2022.3148568.

[86] S. Sepasi, C. Talichet, and A. S. Pramanik, "Power quality in microgrids: A critical review of fundamentals, standards, and case studies," *IEEE Access*, vol. 11, pp. 136235–136257, 2023.

[87] H. Maghfiroh, O. Wahyunggoro, and A. I. Cahyadi, "Energy Management in Hybrid Electric and Hybrid Energy Storage System Vehicles: A Fuzzy Logic Controller Review," *IEEE Access*, vol. 12, pp. 56097–56109, 2024.

[88] S. Wang, Q. Tan, X. Ding, and J. Li, "Efficient microgrid energy management with neural-fuzzy optimization," *International Journal of Hydrogen Energy*, vol. 64, pp. 269–281, 2024.

[89] A. Dev, V. Kumar, G. Khare, J. Giri, M. Amir, F. Ahmad, P. Jain, and S. Anand, "Advancements and challenges in microgrid technology: A comprehensive review of control strategies, emerging technologies, and future directions," *Energy Science & Engineering*, vol. 13, no. 5, pp. 4812–4845, 2025.

[90] "SunPower X-Series: X22-360-COM - Technical Details."

[91] A. G. Yepes, I. Gonzalez-Prieto, O. Lopez, M. J. Duran, and J. Doval-Gandoy, "A comprehensive survey on fault tolerance in multiphase ac drives, Part 2: Phase and switch open-circuit faults," *Machines*, vol. 10, no. 3, p. 221, 2022.

[92] Y. A. M. Alsumaidaee, C. T. Yaw, S. P. Koh, S. K. Tiong, C. P. Chen, and K. Ali, "Review of medium-voltage switchgear fault detection in a condition-based monitoring system by using deep learning," *Energies*, vol. 15, no. 18, p. 6762, 2022.

[93] "FLIR P660- Technical specifications."

[94] Z. Ullah Khan *et al.*, "A Review of Degradation and Reliability Analysis of a Solar PV Module," *IEEE Access*, vol. 12, pp. 185036–185056, 2024.

[95] R. Li, W. Yan, and C. Xia, "Dual-branch diffusion detection model for photovoltaic array and hotspot defect detection in infrared images," *Remote Sensing*, vol. 17, no. 6, p. 1084, 2025.

[96] I. Polymeropoulos, S. Bezyrgiannidis, E. Vrochidou, and G. A. Papakostas, "Enhancing solar plant efficiency: A review of vision-based monitoring and fault detection techniques," *Technologies*, vol. 12, no. 10, p. 175, 2024.

[97] B. C. Russell, A. Torralba, K. P. Murphy, and W. T. Freeman, "LabelMe: A Database and Web-Based Tool for Image Annotation," *Int J Comput Vis*, vol. 77, no. 1–3, pp. 157–173, 2008.

[98] A. Ramon, A. Adán, and F. J. Castilla, "Thermal point clouds of buildings: A review," *Energy and Buildings*, vol. 272, p. 112379, 2022.

[99] A. Pravallika, M. F. Hashmi, and A. Gupta, "Deep learning frontiers in 3D object detection: A comprehensive review for autonomous driving," *IEEE Access*, vol. 12, pp. 78560–78585, 2024.

[100] Z. Lian, Y. Zhan, W. Zhang, Z. Wang, W. Liu, and X. Huang, "Recent Advances in Deep Learning-Based Spatiotemporal Fusion Methods for Remote Sensing Images," *Sensors*, vol. 25, no. 4, p. 1093, 2025.

[101] X. Y. Zhou and G. Z. Yang, "Normalization in training U-Net for 2-D biomedical semantic segmentation," *IEEE Robotics and Automation Letters*, vol. 4, no. 2, pp. 1792–1799, 2019.

[102] K. Awedat, M. Alajmi, and M. Elfituri, "Leveraging U-Net and ASPP for effective fault detection in photovoltaic modules," *Sci Rep*, vol. 15, no. 1, p. 21788, 2025.

[103] G. M. Toche Tchio, J. Kenfack, D. Kassegne, F.-D. Menga, and S. S. Ouro-Djobo, "A comprehensive review of supervised learning algorithms for the diagnosis of photovoltaic systems, proposing a new approach using an ensemble learning algorithm," *Applied Sciences*, vol. 14, no. 5, p. 2072, 2024.

[104] J. Kaur and W. Singh, "Tools, techniques, datasets and application areas for object detection in an image: a review," *Multimed Tools Appl*, vol. 81, no. 27, pp. 38297–38351, Nov. 2022, doi: 10.1007/s11042-022-13153-y.

[105] M. M. Rahman, S. Rahman, S. Bhatt, and M. Faezipour, "A systematic review on advancement of image segmentation techniques for fault detection opportunities and challenges," *Electronics*, vol. 14, no. 5, p. 974, 2025.

[106] E. K. Ukiwe, S. A. Adeshina, T. Jacob, and B. B. Adetokun, "Deep learning model for detection of hotspots using infrared thermographic images of electrical installations," *Journal of Electrical Systems and Inf Technol*, vol. 11, no. 1, p. 24, 2024.

[107] S. Di Adamo, C. O'Meara, G. Cortiana, and J. Bernabé-Moreno, "Practical Quantum K-Means Clustering: Performance Analysis and Applications in Energy Grid Classification," *IEEE Transactions on Quantum Engineering*, vol. 3, pp. 1–16, 2022.

[108] M. Siami, T. Barszcz, and R. Zimroz, "Advanced image analytics for mobile robot-based condition monitoring in hazardous environments: A comprehensive thermal defect processing framework," *Sensors*, vol. 24, no. 11, p. 3421, 2024.

[109] F. M. Shiri, T. Perumal, N. Mustapha, and R. Mohamed, "A Comprehensive Overview and Comparative Analysis on Deep Learning Models: CNN, RNN, LSTM, GRU," *JAI*, vol. 6, no. 1, pp. 301–360, 2024.

[110] M. Abumohsen, A. Y. Owda, and M. Owda, "Electrical load forecasting using LSTM, GRU, and RNN algorithms," *Energies*, vol. 16, no. 5, p. 2283, 2023.

[111] D. Chi, "Research on electricity consumption forecasting model based on wavelet transform and multi-layer LSTM model," *Energy Reports*, vol. 8, pp. 220–228, July 2022.

[112] K. Alomar, H. I. Aysel, and X. Cai, "Data augmentation in classification and segmentation: A survey and new strategies," *Journal of Imaging*, vol. 9, no. 2, p. 46, 2023.

[113] L. Bonaccorsi, R. Carbone, F. La Foresta, C. Marino, A. Nucara, M. Pietrafesa, and M. Versaci, "Operational analysis of a pilot-scale plant for hydrogen production via an electrolyser powered by a photovoltaic system," *Energies*, vol. 18, no. 15, p. 3949, 2025.

[114] G. Rajendran, R. Raute, and C. Caruana, "A comprehensive review of solar PV integration with smart-grids: Challenges, standards, and grid codes," *Energies*, vol. 18, no. 9, p. 2221, 2025.

[115]N. Henry Alombah, A. Harrison, S. Kamel, H. Bertrand Fotsin, and M. Aurangzeb, "Development of an efficient and rapid computational solar photovoltaic emulator utilizing an explicit PV model," *Solar Energy*, vol. 271, p. 112426, 2024.

[116] C. P. Chioncel, E. Spunei, and G. O. Tirian, "The problem of power variations in wind turbines operating under variable wind speeds over time and the need for wind energy storage systems," *Energies*, vol. 17, no. 20, p. 5079, 2024.

[117] A. Chahbi, M. Yessef, A. Amharech, and H. Ameziane, "A comprehensive approach to wind turbine optimization integrating MPPT and speed control," in *Proceedings of the 2024 6th International Symposium on Advanced Electrical and Energy Systems (ISAEE)*, IEEE, 2024, pp. 1–6.

[118] Y. Al-Okbi, A. S. N. Al-murshedi, M. N. Nemah, and H. A. K. Saad, "Influence of design anode and cathode channel on (PEMFC)

fuel cell performance," *Materials Today: Proceedings*, vol. 42, pp. 2177–2184, 2021.

[119] F. Mazzeo, L. Di Napoli, and M. Carello, "Assessing open circuit voltage losses in PEMFCs: A new methodological approach," *Energies*, vol. 17, no. 11, p. 2785, 2024.

[120] X. Meng, M. Liu, J. Mei, X. Li, S. Grigoriev, H. M. Hasanien, X. Tang, R. Li, and C. Sun, "Polarization loss decomposition-based online health state estimation for proton exchange membrane fuel cells," *International Journal of Hydrogen Energy*, vol. 157, pp. 150162–150174, 2025.

[121] Y. NaitMalek, M. Najib, M. Bakhouya, and M. Essaaidi, "Embedded real-time battery state-of-charge forecasting in micro-grid systems," *Ecological Complexity*, vol. 47, p. 100944, 2021.

[122] M. Daryaei, S. A. Khajehoddin, J. Mashreghi, and K. K. Afridi, "A new approach to steady-state modeling, analysis, and design of power converters," *IEEE Transactions on Power Electronics*, vol. 36, no. 6, pp. 6422–6436, 2021.

[123] G. Angiulli, M. Versaci, P. Burrascano, and F. Laganá, "A Data-Driven Gaussian Process Regression Model for Concrete Complex Dielectric Permittivity Characterization," *Sensors*, vol. 25, no. 20, p. 6350, 2025.

[124] F. Chang, J. O'Donnell Jr, and W. Su, "Voltage stability assessment of AC/DC hybrid microgrid," *Energies*, vol. 15, no. 1, p. 399, 2022.

[125] D. Raveendhra, R. Poojitha, and B. L. Narasimharaju et. al, "Part II: State-of-the-art technologies of solar-powered DC microgrid with hybrid energy storage systems: Converter topologies," *Energies*, vol. 16, no. 17, p. 6194, 2023.

[126] "Supporting Paper for the Load-Frequency Control and Reserves Network Code – Policy on Load-Frequency Control and Reserves," ENTSO-E (European Network of Transmission System Operators for Electricity).

[127] A. Aff, M. Simab, M. Nafar, and A. Mirzaee, "Robust linear parameter varying frequency control for islanded hybrid AC/DC microgrids," *Electric Power Systems Research*, vol. 214, p. 108898, 2023.

[128] B. Adineh, M. R. Habibi, A. N. Akpolat, and F. Blaabjerg, "Sensorless voltage estimation for total harmonic distortion calculation using artificial neural networks in microgrids," *IEEE Transactions on Circuits and Systems II: Express Briefs*, vol. 68, no. 12, pp. 4447–4451, 2021.

[129] S. Ahmad, M. Shafiullah, C. B. Ahmed, and M. Alowaifeer, "A review of microgrid energy management and control strategies," *IEEE Access*, vol. 11, pp. 118965–118987, 2023.

[130] Z. Ullah, S. Wang, J. Lai, M. Azam, F. Badshah, G. Wu, and M. R. Elkadeem, "Implementation of various control methods for the efficient energy management in hybrid microgrid system," *Ain Shams Engineering Journal*, vol. 14, no. 5, p. 101961, 2023.

[131] N. Khosravi, "A hybrid control approach to improve power quality in microgrid systems," *Artif Intell Rev*, vol. 58, no. 10, p. 312, July 2025.

[132] M. Versaci, G. Angiulli, P. Crucitti, D. De Carlo, F. Laganà, D. Pellicanò, and A. Palumbo, "A fuzzy similarity-based approach to classify numerically simulated and experimentally detected carbon fiber-reinforced polymer plate defects," *Sensors*, vol. 22, no. 11, p. 4232, 2022.

[133] M. Versaci, G. Angiulli, F. La Foresta, F. Laganà, and A. Palumbo, "Intuitionistic fuzzy divergence for evaluating the mechanical stress state of steel plates subject to bi-axial loads," *Integrated Computer-Aided Engineering*, vol. 31, no. 3, pp. 289–302, 2024.

[134] S. A. Adegoke and Y. Sun, "Power system optimization approach to mitigate voltage instability issues: A review," *Cogent Engineering*, vol. 10, no. 1, p. 2153416, 2023.

[135] M. Versaci and F. La Foresta, "Fuzzy approach for managing renewable energy flows for DC-microgrid with composite PV-WT generators and energy storage system," *Energies*, vol. 17, no. 2, p. 402, 2024.

[136] V. Subramanian and V. Bereznychenko, "Cognitive fuzzy logic-integrated energy management for self-sustaining hybrid renewable microgrids," *Scientific Reports*, vol. 15, no. 1, p. 94077, 2025.

[137] P. Horrillo-Quintero, P. García-Triviño, E. Hosseini, C. A. García-Vázquez, and H. Sánchez-Sainz, "Dynamic fuzzy logic energy management system for a multi-energy microgrid," *IEEE Access*, vol. 12, pp. 78532–78545, 2024.

[138] V. S. B. Kurukuru, A. Haque, S. Padmanaban, and M. A. Khan, "Rule-based inferential system for microgrid energy management system," *IEEE Systems Journal*, vol. 15, no. 3, pp. 4111–4122, 2021.